UC San Diego
UC San Diego Electronic Theses and Dissertations

Title

Stratocumulus-Topped Boundary Layers over Coastal Land

Permalink

https://escholarship.org/uc/item/1c21m29t

Author

Ghonima, Mohamed Sherif

Publication Date

2016

Peer reviewed|Thesis/dissertation

UNIVERSITY OF CALIFORNIA, SAN DIEGO

Stratocumulus-Topped Boundary Layers over Coastal Land

A dissertation submitted in partial satisfaction of the requirements for the degree Doctor
of Philosophy

in

Engineering Sciences (Mechanical Engineering)

by

Mohamed Sherif Ghonima

Committee in charge,

        Jan Kleissel, Chair
        Carlos Coimbra
        Thijs Heus
        Joel Norris
        Lynn Russell
        Sutanu Sarkar

2016

The dissertation of Mohamed Sherif Ghonima is approved, and it is acceptable in quality and form for publication on microfilm and electronically:

_____

_____

_____

_____

_____

_____
                                                                    Chair

University of California, San Diego

2016

DEDICATION

I dedicate this work to my parents, Sherif and Amany Ghonima, for their continuous support and belief in me.

TABLE OF CONTENTS

LIST OF FIGURES

ix

LIST OF TABLES

ACKNOWLEDGEMENTS

stratocumulus-topped marine boundary layers and proposed correction to improve

entrainment parameterization *Atmos. Chem. Phys.,* to be submitted

VITA

Education

2010   *Bachelor of Science* (Magna Cum Laude)*,* Mechanical Engineering, American University of Sharjah, U.A.E.

2011   *Master of Science,* Engineering Sciences (Mechanical Engineering), University of California, San Diego

2016   *Doctor of Philosophy,* Engineering Sciences (Mechanical Engineering), University of California, San Diego

Publications

1. **Ghonima, M. S.**, B. Urquhart, C. W. Chow, J. E. Shields, A. Cazorla, and J. Kleissl, 2012: A method for cloud detection and opacity classification based on ground based sky imagery. *Atmos. Meas. Tech.*, **5**, 2881–2892, doi:10.5194/amt-5-2881-2012.

2. Urquhart, B., M. Ghonima, D. Nguyen, B. Kurtz, C. Chow, and J. Kleissl, 2013: Sky Imaging Systems for Short-term Forecasting. Solar Energy Forecasting and Resource Assessment, J. Kleissl, Ed., Elsevier Academic Print, 195–232.

3. Yang, H., B. Kurtz, D. Nguyen, B. Urquhart, C. W. Chow, **M. Ghonima**, and J. Kleissl, 2014: Solar irradiance forecasting using a ground-based sky imager developed at UC San Diego. *Sol. Energy*, **103**, 502–524, doi:10.1016/j.solener.2014.02.044.

4. **Ghonima, M. S.**, J. R. Norris, T. Heus, and J. Kleissl, 2015: Reconciling and Validating the Cloud Thickness and Liquid Water Path Tendencies Proposed by R. Wood and J. J. van der Dussen et al. *J. Atmos. Sci.*, **72**, 2033–2040, doi:10.1175/JAS-D-14-0287.1.

5. Urquhart, B., B. Kurtz, E. Dahlin, **M. Ghonima**, J. E. Shields, and J. Kleissl, 2015: Development of a sky imaging system for short-term solar power forecasting. *Atmos. Meas. Tech.*, **8**, 875–890, doi:10.5194/amt-8-875-2015.

6. **Ghonima, M. S.,** T. Heus, J. R. Norris, and J. Kleissl, 2016: Factors controlling stratocumulus cloud lifetime over coastal land. *J. Atmos. Sci.*, doi:10.1175/JAS-D-15-0228.1.

7. **Ghonima, M. S.**, C. K. Kim, T. H. Heus, and J. Kleissl: Evaluation of WRF SCM simulations of a stratocumulus-topped marine boundary layers and proposed correction to improve entrainment parameterization *Atmos. Chem. Phys.,* **to be submitted**

8. Hanna, R., **M. Ghonima**, J. Kleissl, G. Tynan, D. Victor Business Models for Distributed Power Generation: The case of microgrids., **to be submitted.**

Field of Study

Major Field: Mechanical Engineering, Atmospheric Science, Fluid Dynamics

ABSTRACT OF THE DISSERTATION

Stratocumulus-Topped Boundary Layers over Coastal Land

by

Mohamed Sherif Ghonima

Doctor of Philosophy OF Engineering Sciences (Mechanical Engineering)

University of California, San Diego, 2016

Professor Jan Kleissl, Chair

Stratocumulus is the most common cloud type and has a strong impact on global climate. Over coastal lands, which are frequently well populated, these clouds have a strong impact on surface temperature and radiation through reflection of incoming solar radiation. The cloud behavior is determined both by small-scale processes such as turbulent mixing between two-phase, two-component, fluids at the cloud top and large-

scale circulation such as anticyclones and their climatological occurrence. Due to the large range of spatial scales associated with stratocumulus clouds, global climate models (GCM) and numerical weather prediction models (NWP) parameterize the physical processes occurring in the stratocumulus-topped boundary layer (STBL). However, these models are unable to simulate the clouds accurately. For instance, in the North American Model stratocumulus clouds over the California coast in the summer dissipate earlier than observed via satellite.

In this thesis, we first employ high-resolution Large Eddy Simulations (LES) and Mixed Layer Models (MLM) to study mechanisms regulating the timing of the break up. We find that over coastal lands, as the cloud thins during day, turbulence generated by surface fluxes becomes larger than turbulence generated by longwave cooling across the cloud layer. To capture this shift in turbulence generation in the MLM, we extend an existing entrainment parameterization to account for both sources. We find that cloud lifetime depends on a combination of surface moisture content, cloud-top entrainment flux, and large-scale horizontal advection by sea breeze.

Next, we evaluate three different planetary boundary layer (PBL) parameterization schemes in the Weather Research and Forecasting (WRF) model in simulating the STBL by benchmarking them against high-resolution LES. We find that the schemes do not take into account the turbulence generated by longwave cooling across the cloud layer and therefore underestimate the mixing of warm-dry tropospheric into the STBL at the cloud top. Thus, we propose a correction to the eddy diffusivity coefficient by adding a term that accounts for turbulence generated throughout the cloud layer as well as at the surface due to buoyancy flux. The modified scheme is then able to

simulate the cloud physics similar to that of the LES. The modeling tools developed in this thesis have improved the understanding of and the ability to forecast stratocumulus-topped boundary layers.

Chapter 1.   Introduction

1.1 Motivation and Research Objectives

Stratocumulus clouds cover approximately one-fifth of the Earth's surface in the annual mean making them the most common cloud type (Warren *et al*., 1986, 1988). The stratocumuli's relatively high albedo (30-40%), compared to the ocean's albedo (~10%), results in the reflection of an increased amount of solar radiation to the top of the atmosphere (Fig. 1.1). In the longwave spectrum, the reduction in upward thermal emissions is not significant, due to the cloud's low altitude and relatively warm temperatures (Randall *et al*., 1984). As a result, stratocumulus clouds have a net cooling effect on the planet and in the global climate system and small changes in stratocumulus cloud cover can produce a radiative effect in the same order of magnitude as that introduced by increasing greenhouse gases (Randall *et al*., 1984; Slingo, 1990; Wood, 2012). These realizations led to intensive studies, over the past half century, on the impacts of stratocumulus clouds on the global climate system. These studies focused on observing, measuring and modeling marine stratocumulus clouds in the subtropics (Wood 2012, and references therein).

Over land, stratocumulus clouds have received less attention. These clouds are typically associated with post-cold-frontal air masses or form due to advection of clouds forming over the ocean onshore (Mechem et al. 2010 and Ghonima et al. 2016). Over the coastal lands, which are frequently well populated, the stratocumulus clouds have a strong impact on the energy and water budgets as well as surface temperatures. During

1

heat waves, the optically thick stratocumulus clouds have a substantial cooling effect and can mitigate the adverse effects of the heat waves on the population (Gershunov et al. 2009). The optically thick stratocumulus clouds greatly reduce visibility and thereby affect air traffic. For instance, the presence of marine stratocumulus over the San Francisco International Airport (SFO) forces airplanes to arrive singularly instead of in tandem on parallel runways in the case clear skies (Hilliker and Fritsch 1999). Such studies highlight the need for a more in-depth study and the development of a coherent theory on the factors controlling the formation and dissipation of stratocumulus.

Rooftop solar photovoltaic (PV) power production along the coasts where stratocumulus clouds are prevalent, such as California, is particularly impacted by stratocumulus formation and dissipation (Mathiesen el al. 2013). The dissipation of these clouds is spatially correlated; thus, large changes in power production by the PV panels are observed as a result. These large changes, commonly referred to as ramps in the electric power modeling community, reduce the reliability of the electric grid and make the integration of PV onto the grid challenging (Jamaly *et al.*, 2013). In order to mitigate the effects of ramps in PV power on the electric grid, numerical weather prediction (NWP) models are employed to forecast the formation and dissipation of stratocumulus. However, several studies have found consistent under-predictions of cloud cover for a variety of NWPs, such as the North American Mesoscale (NAM), the European Centre for Medium-range Weather Forecasts (ECMWF) and the Weather Research and Forecasting models (WRF, Remund *et al.*, 2008, Mathiesen and Kleissl, 2011, Perez *et al.*, 2013).
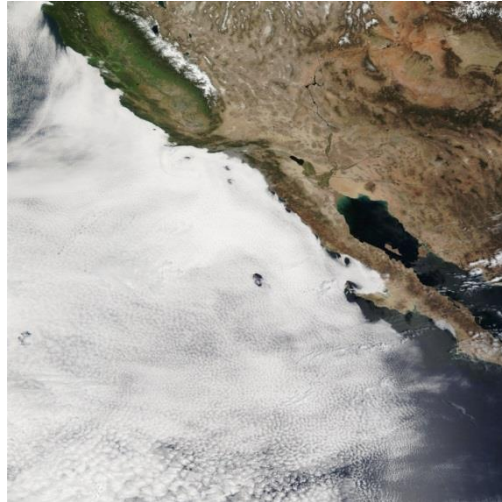
Figure 1.1. Stratocumulus cloud deck off the coast of California, captured by NASA's MODIS Terra satellite on April 14 2013.

1.2 Literature Review

Stratocumulus clouds form under strong temperature inversions (Klein and Hartmann, 1993), where longwave and evaporative cooling at the cloud top are the main drivers of turbulence in the stratocumulus-topped Boundary Layer (STBL) at night. Parcels at the cloud top cool due to longwave radiative emissions thereby becoming denser and sink through the boundary layer driving turbulent mixing. Because of the turbulence, the STBL is relatively well mixed. Especially in shallow STBL, the turbulence acts to couple the cloud layer to the surface, which – over the ocean – is an important source of moisture that offsets the entrainment of warm dry air at the cloud top (Bretherton and Wyant, 1997). During the day, solar loading at the cloud top reduces the longwave cooling thereby reducing the convective circulation during the day for STBL over the ocean. This can lead to decoupling of the cloud layer from the surface (Duynkerke *et al*., 2004). Due to decoupling, a stable stratified layer forms under the cloud layer preventing moisture from the surface from being transported into the cloud

and subsequently the cloud begins to dry out due to entrainment. Over land, as the turbulence generated by longwave cooling is offset by shortwave warming the source of turbulence generation shifts from the cloud-top to the surface flux driven thermals. Surface flux generated turbulence is much stronger than that generated by longwave cooling; thus, as the cloud layer remains coupled to the land surface (Ghonima et al. 2016). In both cases of stratocumulus occurring over the ocean and land, the clouds can exhibit a marked diurnal cycle (Wood *et al*. 2002).

Various remote sensing studies have been conducted to characterize the global climatology of Stratocumulus. Hahn and Warren's (2007) dataset of surface observation of cloud cover over land and ocean depicted in Wood (2012) show that the subtropical eastern oceans are covered by extensive regions in which the stratocumulus cover can exceed 40% with the maxima of stratocumulus cover usually occurring 5° to 10° off the coasts. These clouds exhibit a strong seasonal cycle that follows the seasonal cycle of lower-tropospheric stability, defined as the difference in potential temperature between the free troposphere and the surface (Klein and Hartmann, 1993). Furthermore, through statistical analysis of satellite cloud data Myers and Norris (2013) showed that stronger inversions result in increased stratocumulus cloud fraction while enhanced subsidence has an opposite effect on cloud fraction. Along the North American Pacific coast, from Southern California to Alaska, Schwartz et al. (2014) showed that low clouds, including stratocumulus clouds, constitute >40% of cloud cover occurring during the summer months from 1950 to 2012. These low clouds respond to large-scale forcings, such as Pacific Decadal Oscillation, coherently across the entire west coast of North America and across a wide range of time scales.

In addition to remote sensing, various field campaigns have been conducted in order to obtain in-situ measurement of key process, such as entrainment velocity at the cloud top. For example, the Atlantic stratocumulus Experiment (ASTEX) was conducted over the northeast Atlantic Ocean in June 1992 to study the transition of stratocumulus to cumulus clouds with a variety of measurements obtained from planes, ships, land based instruments and satellites (Albrecht *et al*. 1995). The Dynamics and Chemistry of Marine stratocumulus (DYCOMS-II) study was conducted off the coast of California, to study the entrainment process in nocturnal stratocumulus as well as the importance of drizzle in the boundary layer (Stevens *et al*. 2003b). The VAMOS Ocean-Cloud-Atmosphere-Land Study Regional Experiment (VOCALS-REx) was conducted in the southeast Pacific to study the effects of aerosols and precipitation on stratocumulus radiative properties as well as the physical and chemical couplings between the upper ocean and the lower atmosphere (Wood *et al*., 2011). In the case of continental stratocumulus clouds, the majority of the studies were conducted at the ARM observation facility in the southern great plains (SGP), Oklahoma (Kollias and Albrecht 2000; Zhu et al. 2001; Ghate et al. 2010; Fang et al. 2014a,b). These studies have mainly utilized surface-based measurements to characterize the turbulence characteristics in STBL. Mechem et al. (2010) used LES in addition to surface measurements to analyze post-cold-frontal continental stratocumulus over the SGP.

Large Eddy Simulations (LES) play an important role in filling the gap in observations of quantities, such as third-moment atmospheric profiles, that are both very difficult and expensive or in some cases impossible to measure. LES solve the Navier–Stokes equations and filters out the small-scale eddies which are then parameterized

using a sub-grid scale model. Hence, LES explicitly simulates the energy-containing scales of turbulence in the STBL. Multiple intercomparisons between different LES models and measurement campaigns have been conducted to determine the accuracies of LES in simulating the STBL (Stevens et al. 2005; Ackerman et al. 2009). Of particular importance, was validating the capability of LES models in representing entrainment (mixing) at the cloud-top interface. This was particularly challenging, as the LES were expected to model two-phase fluids at very high Reynolds numbers. Stevens et al. (2005) found that the different LES were able to match measurements of cloud-top entrainment relatively well once the vertical grid was refined thereby limiting the effects of the sub-grid model and reducing the effects of spurious mixing at the cloud top. A more recent LES inter-comparison was conducted to study the sensitivity of stratocumulus to idealized climate changes and the models were found to agree well (Zhang *et al*., 2012; Blossey *et al*., 2013).

In contrast to LES, Mixed Layer Models (MLM) are computationally inexpensive conceptual tools that consists of a thermodynamic model of convective boundary layers which solves the boundary layer mass, heat, and moisture budget equations (Lilly, 1968). Due to turbulence generated by longwave cooling or land surface flux in the STBL, the thermodynamic properties are assumed to follow the adiabatic values and the STBL is taken to be well-mixed. Thus conserved tracers, such as liquid potential temperature and total water mixing ratio, are uniform within the boundary layer (Albrecht et al., 1990; Caldwell et al., 2005). The well-mixed assumption breaks down when the STBL becomes decoupled due to a reduction in turbulence in the boundary layer or to an increase in the inversion height. Researchers typically use the MLM in order to understand the impacts

of different physical processes on boundary layer turbulence. For example, researchers used the MLM to propose various entrainment parameterizations for stratocumulus occurring over the ocean (refer to Stevens 2002 for a comprehensive review of such efforts).

In addition to improving our knowledge of how stratocumulus function, measurements, MLM, and LES provide the basis for boundary layer parameterizations in global climate models (GCM) and numerical weather prediction models (NWP). While both GCM and NWP have different applications, both models share the same underlying principle of resolving the large-scale flow and parameterizing the turbulence within the boundary layer through Planetary Boundary Layer (PBL) schemes. The effects of PBL can be incorporated into the large-scale model in two ways: the first, involves parameterizing the entire PBL as one layer, which is usually the case for GCMs that are run for hundreds of years and therefore have limited computational power to represent the boundary layer at higher resolutions. The second is to resolve the PBL with several computational levels, which is the case for NWPs. These PBL schemes parameterize the turbulent flux of momentum, heat and moisture within the boundary layer and hence employ some types of turbulent closure to relate the turbulent fluxes to the mean quantities (Holt and Raman 1998; Nakanishi and Niino 2004; Hong et al. 2006). It is important to note that the representation of thermodynamic and kinematic structures in the boundary layer is one of the main sources of uncertainty and divergence in simulations of the different NWPs and GCMs (Hu et al. 2010; Nielsen-Gammon et al. 2010, Zhang et al. 2013).

1.3 Characterization of Coastal Stratocumulus

This study will mainly focus on stratocumulus clouds forming over midlatitude coastal land area. The clouds are especially prevalent during the summer months in the northern hemisphere due to strong climatological anticyclones over the adjacent ocean. The clouds form as rising air parcels originating at the ocean surface cool and expand, the parcel's relative humidity (RH) increases. Once RH exceeds 100%, water vapor condenses into liquid water droplets and clouds form. The prevailing onshore winds then advect the clouds inland at night. The extent of the advection inland is dependent on the topography, if the elevation exceeds the inversion height. Using normalized GHI observations (% of instantaneous clear sky irradiance computed based on Ineichen and Perez, 2002) from a Li-200SZ (LiCor, Nebraska, US) pyranometer at the University of California, San Diego (117.23° W, 32.88° N, approximately 1 km from the Pacific Ocean) in 2011. We observe that the averaged irradiance is lowest during mornings in the months of May-September, compared to the rest of the year, corresponding with the occurrence of coastal stratocumulus clouds (Fig 1.2(a)).

Clouds begin to dissipate furthest inland first in the morning and at progressively later times closer to the coast, where the clouds often survive into the afternoon (Fig. 1.2 (b); Skupniewicz et al., 1991). Similar to the stratocumulus clouds occurring over the ocean, stratocumulus clouds over coastal land attain maximum coverage at sunrise. After sunrise, solar radiation warms the atmospheric STBL and land surface. Due to the lower heat capacity of land, a significant portion of the solar radiation absorbed at the surface is converted to convective surface fluxes, which in turn warm and moisten the STBL depending on land surface properties such as soil moisture content. Even though the

Bowen ratio can be greater than one over land, the larger total available energy can result in a higher latent heat flux over land then over ocean. The surface buoyancy fluxes also drive turbulence in the STBL, which in turn increases the cloud top entrainment and inversion height. Greater warming of land during day drives a stronger pressure difference between land and ocean boundary layers, which in turn increases onshore advection. The horizontal advection of marine air has a cooling effect on the land STBL and may decrease the absolute humidity over land even though the relative humidity of the advected marine air is higher than that of the onshore air. As the day progresses, surface flux heating/moistening, advection of cool oceanic air, and entrainment of warm dry air into the STBL all increase. Price (1999) studied the breakup of stratocumulus over the coast in the UK and found that cloud break up was caused by solar heating in one case and by a combination of solar heating and shear-driven entrainment in another case.

a)
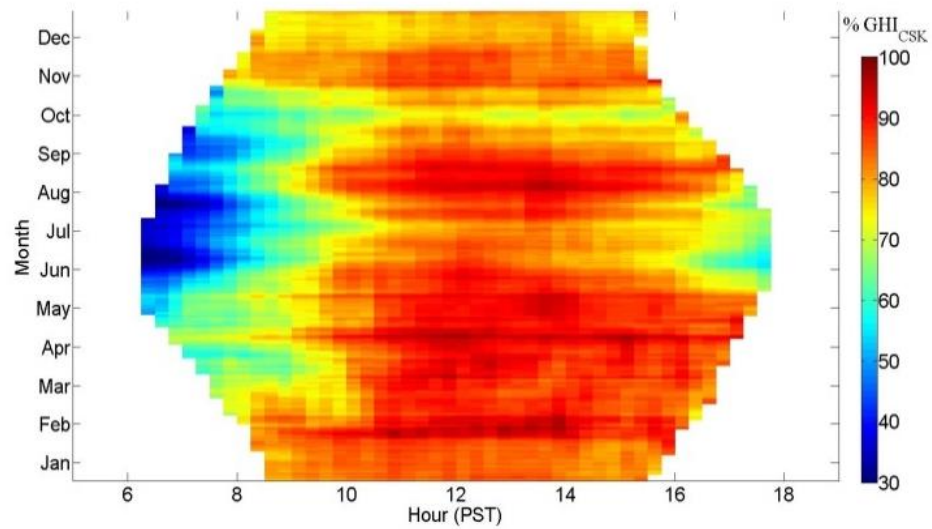
b)
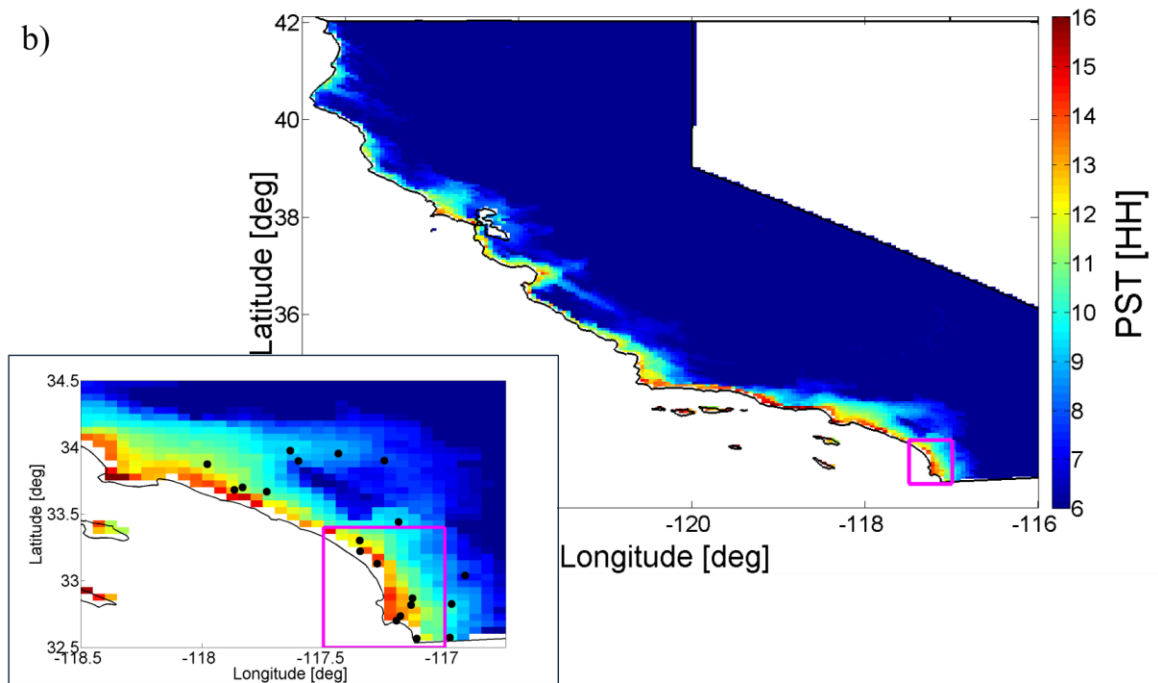
Figure 1.2. (a) Normalized GHI observations **(b)** Averaged cloud dissipation time derived from satellite solar resource data for June 2-9 2014 (SolarAnywhere 2014) for the state of California. Averaged cloud dissipation time for southern California overlaid with METAR stations along the coast. The magenta box represents the domain where METAR wind data is acquired to model advection (117 -118°W, 32.5 - 33.3°N).

While in reality the inland penetration of the stratocumulus clouds is limited by distance from the coast and by topography, for the purpose of this paper we shall neglect topographical effects. We define three domains: an "over the ocean" domain, a "coupled" domain which consists of an STBL over the land with large-scale advection of cool moist air from the ocean, and a "land" domain which we assume to be sufficiently inland that advection does not play a significant role in modulating the cloud lifetime (Fig. 1.3). We simulate the ocean case to serve as a baseline analysis to compare against published results as well as to contrast against the coupled and land cases. The coupled case is chosen to study the effects of large-scale horizontal advection on cloud lifetime. Each of the coupled and land domains are further broken down into two cases, one consisting of a STBL over a wet land surface and another case over a moderately dry land surface. The wet and dry surface cases are chosen to study the effects of idealized surface moisture content and vegetation cover on cloud lifetime.
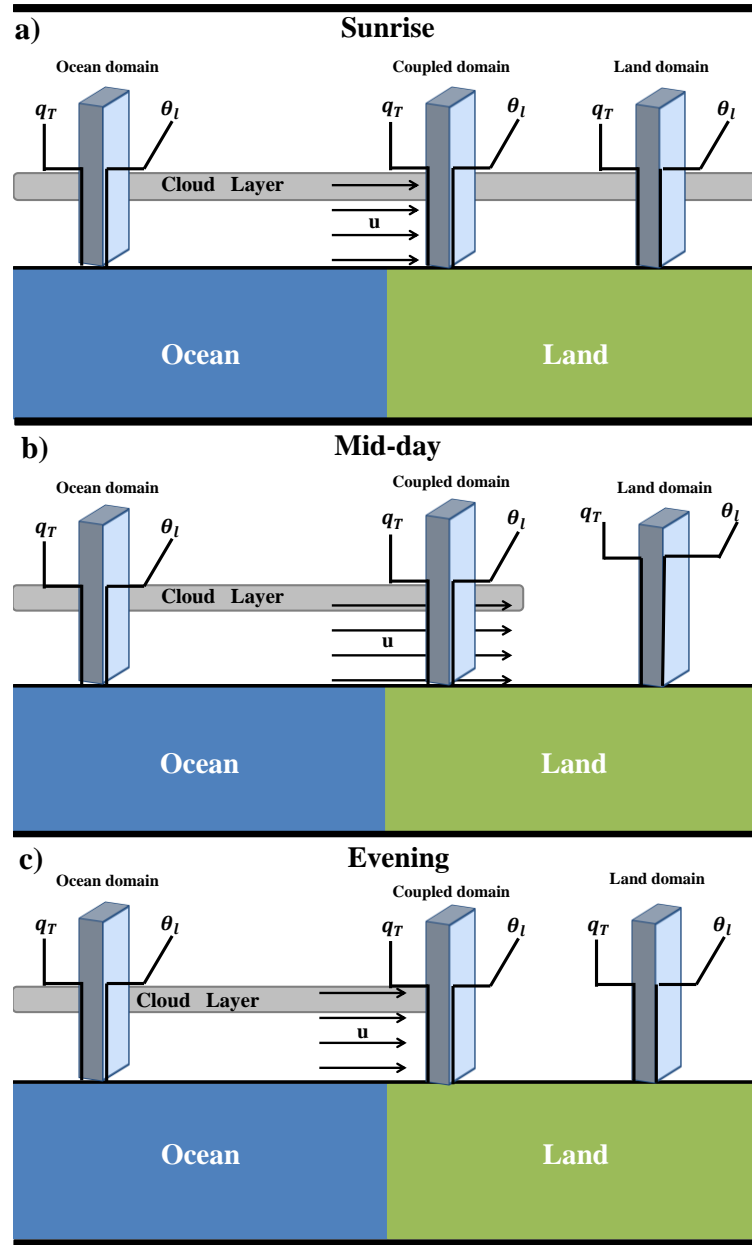
Figure 1.3. Schematic description of stratocumulus cloud dissipation. **(a)** At sunrise, the stratocumulus cloud extends from over the ocean inland, thermodynamic profiles are well-mixed, and there is a strong thin inversion. **(b)** At midday, the stratocumulus cloud begins breaking up inland first and the dissipation propogates towards the coast. The cloud has dissipated inland giving rise to a clear dry convective boundary layer. Near the coast the cloud has thinned significantly and is near dissipation. Over the ocean the cloud has thinned but less so due to lower surface warming occuring in the ocean domain. For all three domains the boundary layer remains well-mixed driven by longwave cooling in the ocean surface case and surface flux in the land cases. **(c)** In the evening, the horizontal extent of of the stratocumulus is at its minimum. The clear dry convective boundary layer inland begins to collapse as the surface flux driving turbulence decreases. Near the coast, the cloud has dissipated but the inversion is supported by the advection of oceanic air mass inland. Over the ocean, the cloud begins to thicken as solar radiation goes to zero. During the night as the cloud thickens over the ocean it is advected inland.

1.4 Thesis Outline

The outline of the thesis is as follows. Chapter 2 consists of an overview of the UCLA- LES model. Chapter 3 analyzes the thermodynamic and turbulent structure of STBL over coastal lands as well as analyzing the effects of aerosols on stratocumulus cloud lifetime. Chapter 4 consists of an overview of the mixed-layer theory and modifications to the MLM to more accurately represent how changes in cloud base and cloud top temperature affect longwave radiation and to more accurately represent the combined effect of surface and cloud-driven buoyancy on turbulence and entrainment. Next, the MLM is applied to understand how STBL turbulence, entrainment, cloud liquid water path (LWP), and cloud thickness respond to the varying initial profiles, wet and dry land surfaces, large-scale advection, and subsidence (Chapter 5). Chapter 6 provides a brief description of PBL schemes employed in NWP and GCMS. Next, SCM representation of the STBL in the Weather Research and Forecasting (WRF) model is evaluated by comparing the SCM results against LES (Chapter 7). In Chapter 8, the most important findings of this thesis are summarized and implications of this thesis to future research on the topic are presented.

Chapter 2. Description of the Large Eddy Simulation Model

This section provides an overview of the UCLA-LES model. The model was developed by Bjorn Stevens at University of California, Los Angeles and grew out of the cloud and meso-scale modelling projects directed by William Cotton and Roger Pielke at Colorado State university. The UCLA-LES has been comprehensively tested and was able to replicate observational data gathered from numerous campaigns (Ackerman et al., 2009; Stevens et al., 2005). The model was also tested against a variety of other LES models (Stevens et al., 2005; Ackerman et al., 2009; Blossey et al., 2013).

2.1 Model Equations

The equations of motion for a moist, compressible, rotating atmosphere under the influence of gravity are

$$\frac{D\rho}{Dt} + \frac{\partial u_i}{\partial x_i} = 0, \tag{1}$$

$$\rho\left(\frac{\partial u_i}{\partial t} + u_j\frac{\partial u_i}{\partial x_j}\right) = -\frac{\partial P}{\partial x_i} - \rho g\delta_{i3} - \rho 2\Omega \times u_i + Q, \tag{2}$$

$$\rho\left(\frac{\partial \phi}{\partial t} + u_j\frac{\partial \phi}{\partial x_j}\right) = \rho\frac{\partial F_\phi}{\partial x_j}\delta_{i3} + Q_\phi, \tag{3}$$

where g, Ω are , respectively, the gravity and angular velocity terms. F_ϕ denotes a flux whose divergence contributes to the evolution of scalar ϕ (for example, in the heat budget equation, ϕ would be replaced by the liquid potential temperature θ_l and Q_ϕ would represent the radiative and precipitation flux). Q represents the viscous stress and

Q_ϕ the molecular diffusion, for a scalar ϕ, term. Both terms are parameterized in LES but do not play a signifacnt role at high Reynolds number, which is typical in the atmospheric BL.

2.1.1   Anelastic and Boussinesq approximation

The equations of motions that describe the evolution of the atmosphere contain solutions resulting from sound waves. In order to filter out the sound waves, which have no meteorological significance, Ogura and Phillips (1962) developed and Durran (1989), Bannon (1996) further improved the anelastic approximations to the equations of motion. The benefit of the anelastic approximation is that hydrostatic balance is not assumed and thus can be applied to cases of deep convection in the atmosphere. It should also be noted that the Boussinesq approximation is a simplified subset of the anelastic approximation. Under the anelastic formulation, the atmospheric variables are split into base state C_0 and perturbations from it C'. The base-state variables are set to satisfy the following set of equations

$$\frac{dP_0}{dz} = -\rho_0 g, \theta_0 = T_0 \left(\frac{P_{00}}{P_0}\right)^{R/c_p}, \tag{4}$$

$$P_0 = \rho_0 R T_0, \tag{5}$$

where ρ_0 is the base state density, T_0 is the reference temperature, P_{00} is a constant reference pressure and θ_0 is the base state potential temperature and. Following Bannon (1996), the anelastic assumptions are: (i) the buoyancy force is the major component of the vertical momentum equation and cannot be neglected (ii) the characteristic vertical displacement (D) of an air parcel is of the same order of magnitude as the density scale

height ($D \sim H_\rho = \left| \frac{-1}{\rho_0} \frac{d\rho_0}{dz} \right|^{-1}$), hence, the Boussinesq approximation is only valid for shallow flows, (iii) the horizontal perturbations of the thermodynamic variables are small compared to the base state values at that height, for example, $C'(x, y, z, t) \ll C_0(z)$ or $\frac{C'(x,y,z,t)}{C_0(z)} = O(\epsilon) \ll 1$. As result of the preceding arguments, the anelastic equations of motion for a compressible atmosphere, expanded into the mean and turbulent parts and Reynolds averaged, are

$$\frac{\partial}{\partial x_i} \cdot (\rho_0 \bar{u}_i) = 0, \tag{6}$$

$$\frac{\partial \bar{u}_i}{\partial t} + \bar{u}_j \frac{\partial \bar{u}_i}{\partial x_j} = -\frac{\partial}{\partial x_i}\left(\frac{P'}{\rho_0}\right) + \frac{\theta'}{\theta_0} g \delta_{i3} + f_k\left(\bar{u}_j - V_{g,j}\right) + \frac{Q}{\rho_0}, \tag{7}$$

$$\frac{\partial \bar{\phi}}{\partial t} + \bar{u}_j \frac{\partial \bar{\phi}}{\partial x_j} = \frac{\partial F_\phi}{\partial x_j} \delta_{i3} + \frac{Q_\phi}{\rho_0}, \tag{8}$$

where $f_k = 2\Omega \sin\theta$ is the Coriolis parameter and $V_{g,j}$ denotes the geostrophic wind. Henceforth, the over-bar denotes a filtered quantity and $'$ denotes a residual quantity. The subgrid-scale stress, Q, and subgrid-scale heat flux, Q_ϕ, terms can be formulated in terms of the divergence of the momentum, $(\tau_{i,j})$, and scalar $(\gamma_{\phi,j})$ sub-grid flux. $\tau_{i,j}$ and $\gamma_{\phi,j}$ are defined as:

$$\tau_{i,j} = \overline{u_i u_j} - \bar{u}_i \bar{u}_j, \tag{9}$$

$$\gamma_{i,j} = \overline{\phi u_j} - \bar{\phi} \bar{u}_j. \tag{10}$$

Substituting the sub-grid flux (Eqs.9, 10) into Eqs. 6-8, we finally obtain the model equations:

$$\frac{\partial}{\partial x_i} \cdot (\rho_0 \bar{u}_i) = 0, \tag{11}$$

$$\frac{\partial \bar{u}_i}{\partial t} + \bar{u}_j \frac{\partial \bar{u}_i}{\partial x_j} = -\frac{\partial}{\partial x_i}\left(\frac{P'}{\rho_0}\right) + \frac{\theta'}{\theta_0} g \delta_{i3} + f_k\left(\bar{u}_j - V_g, j\right) + \frac{1}{\rho_0}\frac{\partial}{\partial x_j}\left[\rho_0 \tau_{i,j}\right], \qquad (12)$$

$$\frac{\partial \bar{\phi}}{\partial t} + \bar{u}_j \frac{\partial \bar{\phi}}{\partial x_j} = \frac{\partial F_\phi}{\partial x_j} \delta_{i3} + \frac{1}{\rho_0}\frac{\partial}{\partial x_j}\left[\rho_0 \gamma_{\phi,j}\right]. \qquad (13)$$

2.2 Sub-grid Parameterization

Large Eddy Simulations are able to simulate the turbulence down to near the grid resolution; hence the sub-grid fluxes $\tau_{i,j}$ and $\gamma_{\phi,j}$ are not explicitly known and must be modeled. The UCLA-LES employs the Smagorinsky model to determine the sub-grid fluxes (refer to Meneveau and Katz (2000) for a review of the Smagorinsky model):

$$\tau_{i,j} = -\rho_0 K_m D_{i,j}, \qquad (14.1)$$

$$\gamma_{\phi,j} = -\frac{K_m}{Pr}\frac{\partial \bar{\phi}}{\partial x_j}, \qquad (14.1)$$

where $D_{i,j} = \frac{\partial \bar{u}_i}{\partial x_j} + \frac{\partial \bar{u}_j}{\partial x_i}$ is the resolved strain rate tensor and Pr is the Prandtl number. K_m is the eddy viscosity and is modeled as:

$$K_m = (C_s l)^2 S\sqrt{1 - Ri/Pr}, \qquad (15)$$

where $= \frac{S^2}{N^2}$, $S^2 = \frac{\partial \bar{u}_i}{\partial x_j} D_{i,j}$ and $N^2 = \frac{g}{\Theta_0}\frac{\partial \bar{\theta}_v}{\partial z}$. θ_v is the virtual potential temperature and Θ_0 is the background temperature. $C_s = 0.2$ is the Smagorinsky constant and $l^{-2} = (\Delta x \Delta y \Delta z)^{-2/3} + (z\kappa/C_s)^{-2}$. $\kappa = 0.35$ is the von Karman constant and $\Delta x \Delta y \Delta z$ represent grid spacing in the x, y, z axis respectively.

2.3 Numerics

The model employs a Runge-Kutta third order method, with a variable time-step that is set to maintain a constant CFL maximum value to maintain numerical stability. The pressure solver uses a two-dimensional Fast Fourier Transform (FFT) to transform the Poisson equation to a second-order ordinary-differential-equation (ODE) that can then be solved efficiently, but globally using a tri-diagonal solver.

The model grid is doubly periodic in the horizontal x, y direction and bounded in the vertical z-direction. The horizontal grid is tiled with uniform spacing while a stretchable grid spans the vertical. The model employs the Arakawa-C grid; whereby, velocity quantities are computed half a grid point up-grid (in the direction of the velocity component) of the thermodynamic and pressure points (note that the zonal velocities are computed at points east and west and meridional at points north and south).

2.4 Radiation

Full radiative schemes are computationally expensive since they compute transmittance in the frequency domain where the absorption cross-sections of gases vary by orders of magnitude over small spectral intervals (Pincus and Stevens, 2009). In order to reduce computational time of radiative schemes, the "correlated k-distribution" method was developed (Lacis and Oinas, 1991; Fu and Liou, 1992). The method consists of a set of B relatively broad spectral bands, in which Rayleigh scattering by molecules and aerosol and cloud water optical properties are considered to be uniform. Within each band similar values of absorption coefficients k are grouped into G "g-points" such that $k \approx k(g)$. The flux for a column at time t can then be computed as

$$F(x, y, t) = \sum_{b}^{B} w_b \sum_{g}^{G(b)} w_{g(b)} F_{b,g}(x, y, t), \qquad (16)$$

where the g-points weights (w_g) are the fraction of each band accounted for by the g-points such that $\sum w_{g(b)} = 1$. w_b denotes the amount of energy within a spectral band; for example, in the solar band, w_b denotes the amount of solar energy emitted within that band. Thus, the correlated k-distribution method computes spectral transmittance with a relatively smaller number of computational points in the g-domain instead of in the highly variable frequency (v) domain that requires a larger number of computational points. However, the correlated k-distribution method is still too computationally expensive to be computed at every time step in the LES (B and G are of order 10; therefore, several hundred pseudo-monochromatic calculations are required for the radiative scheme at each time step in LES).

In order to further reduce the computational time of the correlated k-distribution method, Pincus and Stevens (2009) proposed to randomly select a spectral band and the corresponding g-point as a proxy for the full radiation calculation within a column. Thus, for a randomly chosen value of b' and g', Eq. 16 can then be approximated as:

$$F(x, y, t) \approx F_{MC}(x, y, t) = B w_b' F_{b',g'}(x, y, t), \qquad (17)$$

where the probabilities of choosing a given value of b' and g' are based on the weight of each spectral interval and point. The Monte Carlo Spectrally integrated Radiative flux (MSR,F_{MC}) introduces substantial random error to the LES. However, this error decreases as $1/\sqrt{n}$, where n is the number of samples. As a result equations 16 and 17 converge as the number of samples increase. In the LES, the samples are accumulated

over space and time; hence, the random errors averages out over the domain (Pincus and Stevens, 2009).

2.5 Microphysics

The LES code has several different microphysics models; the simplest of which is a pure condensation scheme, with no rain. The second is a two-moment rain scheme, in which the cloud droplets are assumed to be in equilibrium with a fixed concentration (Seifert and Beheng, 2001; Stevens and Seifert, 2008). In the two-moment rain scheme, the water droplets evolve under the actions of the ambient flow and microphysical processes such as accretion and sedimentation.

The microphysical schemes first compute saturation, and liquid droplets form once the saturation ratio is exceeded so it is an "all-or-nothing" scheme. The cloud droplet number is specified and remains constant throughout the simulation. Thus, the droplet radius varies as total liquid content varies in the BL. In the scheme with precipitation suppressed, unrealistic cloud droplet sizes may be observed at high liquid water contents as the cloud droplet number is constant and the clouds do not rain out.

2.6 Surface Model

The LES is coupled to a surface model to compute surface flux which are introduced through the sub-filter-scale terms at the first atmospheric level. In this thesis, we utilize both ocean and land surface models that are formulated as follows.

2.6.1 Ocean Surface Model

For the ocean cases, the sensible (SHF) and latent heat fluxes (LHF) are computed as

$$SHF = C_T\big(SST - \theta_{l_1}\big), \tag{18.1}$$

$$LHF = C_T\big(0.98q_{sat}(P_s, SST) - q_{T_1}\big), \tag{18.2}$$

where θ_{l_1} and q_{T_1} are liquid potential temperature and total water mixing ratio at the lowest model fluid level, respectively. $q_{sat}(P_s, SST)$ is the saturation specific humidity at the surface pressure (P_s) and sea surface temperature (SST). C_T is the drag coefficient and is set as a constant value in the simulation.

2.6.2 Land Surface Model

For the land cases, the convective fluxes are larger than the ocean case and the partitioning of available energy into sensible (SHF) and latent heat fluxes (LHF) is of primary importance for stratocumulus lifetime and described by the Bowen Ratio ($\beta = \frac{SHF}{LHF}$). A constant Bowen ratio is a simplified assumption that serves to avoid the complexity of a detailed land surface model that lacks generality and introduces many empirical parameters. While the Bowen ratio is motivated by similar exchange coefficients for heat and water and the larger timescales of soil moisture content changes compared to atmospheric turbulence, in practice several limitations exist with the constant Bowen ratio concept. For large available energy at the surface, the ability of the vegetation to conduct sufficient water to the surface to maintain the Bowen ratio may be limited due to stomatal conductance or leaf area index, which results in increased Bowen ratio as the morning progresses e.g. during clear middays. However, stratocumulus

clouds attenuate the shortwave energy available at the surface making this limitation largely irrelevant for the cases studied in this paper. The Bowen ratio will also vary if the air is near saturation inhibiting latent heat flux, which is not the case in our simulations, or if the soil moisture in the root zone or top soil layer reaches the permanent wilting point. Typical Bowen ratio values range from 0.1 over irrigated orchards to 0.2 over forests and grasslands to 2 for urban and semi-arid regions (EPA, 2004). In this thesis, we chose a Bowen ratio of 0.1 to represent the wet surface case and a Bowen ratio of 1.0 to represent the moderately dry surface case. Furthermore, we assume that the land surface is homogeneous.

Hence, the convective surface fluxes are parameterized as a function of the net surface radiation and Bowen ratio as

$$SHF = \phi \left(\frac{\beta}{\beta + 1} \right) F_{rad_0}, \tag{19.1}$$

$$LHF = \phi \left(\frac{1}{\beta + 1} \right) F_{rad_0}, \tag{19.2}$$

where ϕ is the efficiency at which net surface radiation (F_{rad_0}) is converted to convective surface fluxes. LHF is set to zero at night as dew formation is negligible in cloud-topped BLs. The surface energy balance equation is then formulated as

$$F_{rad_0} = \phi \left(\frac{\beta}{\beta + 1} \right) F_{rad_0} + \phi \left(\frac{1}{\beta + 1} \right) F_{rad_0}$$
$$+ (1 - \phi) \left(\varphi c_p \frac{dT_{srf}}{dt} + (1 - \varphi)G \right), \tag{20}$$

where T_{srf} is the surface temperature, G represents the ground heat flux, and φ partitions the heat input into the soil between the top layer $(c_p \frac{dT_{srf}}{dt})$ and the lower layers (G).

2.7 Validation of Land Surface Model

In order to validate the LSM, a clear day (May 02, 2013) was simulated in LES with initial conditions obtained from North American Model (NAM, Janjic et al., 2010, 2011). The LES model was run at 25m horizontal resolution and 5m vertical resolution with grid stretching occurring after 1 Km. The number of points in the horizontal: $N_x = N_y = 52$ and in the vertical $N_z = 193$. LES sampling occured at 20 second intervals and averaged over 600 seconds. The LES model also employed the MSR radiation scheme (section 2.4).

Table 2.1. Land surface model specified properties for coastal sage scrub.

Soil Property	Value	Soil Property	Value	Soil Property	Value
Depth [m]	0.05	Soil temperature [K]	286.55	Soil moisture $[m^3 m^{-3}]$	0.1124
	0.25		293.45		0.1923
	0.70		292.28		0.1933
	1.50		291.57		0.2651
Momentum Roughness Length [m]	0.0371	Heat Roughness Length [m]	0.0371	Heat conductivity skin layer $[Wm^{-1}K^{-1}]$	2.138
Canopy cover [-]	0.372183	Average leaf area index [-]	2.6432	Volumetric moisture at wilting point [-]	0.1
Volumetric moisture at field capacity [-]	0.412	Response factor vegetation to vapor pressure deficit [-]	42	Heat capacity skin layer [kJ]	20
Surface Albedo [-]	0.2661	Minimum vegetation resistance $[sm^{-1}]$	300	Minimum soil evaporation resistance $[sm^{-1}]$	50

In addition to an LES run coupled to the LSM outlined in section 2.6.2, a second LES simulation was coupled to a "full" LSM scheme outlined in Heus et al. (2010) , and Malte et al. (2014). The full LSM scheme parameterizes the turbulent drag and the exchange coefficients between the surface and the first atmospheric level as a function Obukhov length and the surface friction velocity. The surface fluxes are introduced through the sub-filter-scale terms at the first atmospheric level. The full LSM further solves for the surface energy balance equation.

Both models were run till sunset and the surface fluxes and were compared with surface flux, measurements obtained from a FLUXNET site (Gamon et *al,* 2010) located at 33.734 °Lat, -117.696 °Long. The sensible and latent heat flux are in good agreement between the two models and the measurements (Fig. 2.1). During the summer months, there is little precipitation reaching the surface in Southern California. Hence, the soil is dry and the majority of the incoming short wave radiative flux, at the surface, is converted to sensible heat flux (Fig. 2.1). The full LSM was configured to match coastal sage scrub type land, which is a common type of land found in southern California where the FLUXNET sensor was located. Land surface speicifications for the LSM were obtained from the NOAH community model (Hong et al., 2009; Niu, 2011; Table 2.1).
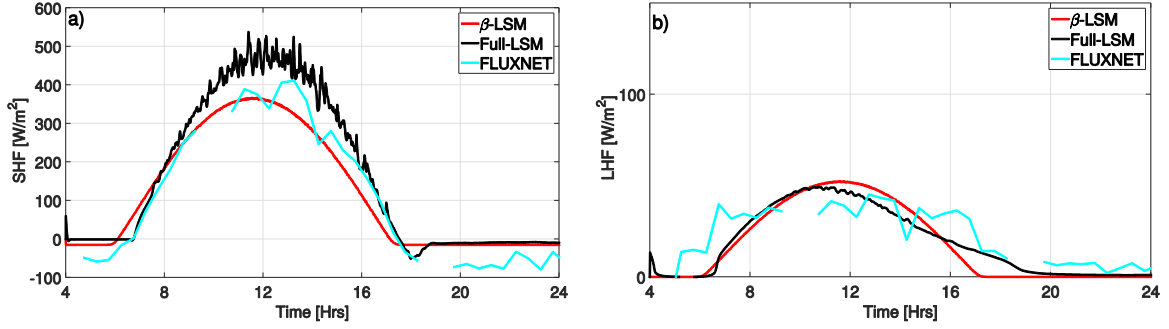
Figure 2.1 (a) Surface sensible heat flux and **b)** latent heat flux time series. LES coupled to the LSM based on Bowen ratio is plotted in red, and the full LSM in black. FLXNET measurements are plotted in cyan. Upward flux is taken to be positive.

2.8 Large-scale Horizontal Advection

Due to the limited horizontal extent of the LES, we are unable to simulate mesoscale atmospheric processes and explicitly compute advective tendencies for the case with ocean-land interaction. Meteorological observations are also not sufficient to compute advection as continuously operating, horizontally displaced profiles would be required. As an alternative, we introduce a simple model to apply large-scale horizontal forcings ($\overline{v} \cdot \nabla_h \overline{\theta_l}, \overline{v} \cdot \nabla_h \overline{q_T}$) to the LES as follows

$$\overline{v} \cdot \nabla_h \overline{\theta_l} = \overline{v} \cdot \left(\overline{\theta_l}_{land}(z,t) - \overline{\theta_l}_{ocean}(z,t) \right)/\Delta x, \tag{21.1}$$

$$\overline{v} \cdot \nabla_h \overline{q_T} = \overline{v} \cdot \left(\overline{q_T}_{land}(z,t) - \overline{q_T}_{ocean}(z,t) \right)/\Delta x, \tag{21.2}$$

where z represents the LES domain height and $\overline{v}$ is the large-scale horizontal surface wind reported hourly from seven METAR stations (117 -118°W, 32.5 - 33.3°N) on the southern California coast for June 2, 2014 (Fig. 2.2 (a)). This day was chosen because Geostationary Operational Environmental Satellite (GOES) imagery showed a typical stratocumulus day with widespread cloud cover at dawn and dissipation progressing from inland towards the ocean through the day (Fig. 1.2 (b)). Primarily westerly winds

throughout the day (Fig. 2.2 (b)), which is representative of summer months along the North American coast due to the North Pacific High and the ocean-land thermal gradient (Taylor et al., 2008).

The LES ocean case provided values of liquid potential temperature and total water mixing ratio profiles $(\overline{\theta_l}_{ocean}(z,t), \overline{q_T}_{ocean}(z,t))$ for use in Eqs. 21.1 and 21.2, while $\overline{\theta_l}_{land}(z,t)$ and $\overline{q_T}_{land}(z,t)$ were dynamically computed within the LES run. Δx is a lengthscale representative of the strength of the large-scale advective tendencies. As Δx increases, the large-scale advective tendencies decrease, corresponding to a domain further inland and not significantly affected by the land-ocean temperature and moisture gradients. For the purpose of this study we chose $\Delta x = 30$ km, which is representative of the scale of inland penetration of stratocumulus. We note that this is an idealized analysis and that we made the following simplifying assumptions: (i) surface wind velocity measurements are representative of the boundary layer wind profiles, (ii) wind direction is perpendicular to the coast, (iii) topographic effects are negligible. Although these assumptions lead to significant deviations from the actual advective tendencies, our goal is to gain a sense of how large-scale advection affects the cloud layer. Hence, we believe that our assumptions are reasonable within our idealized framework.
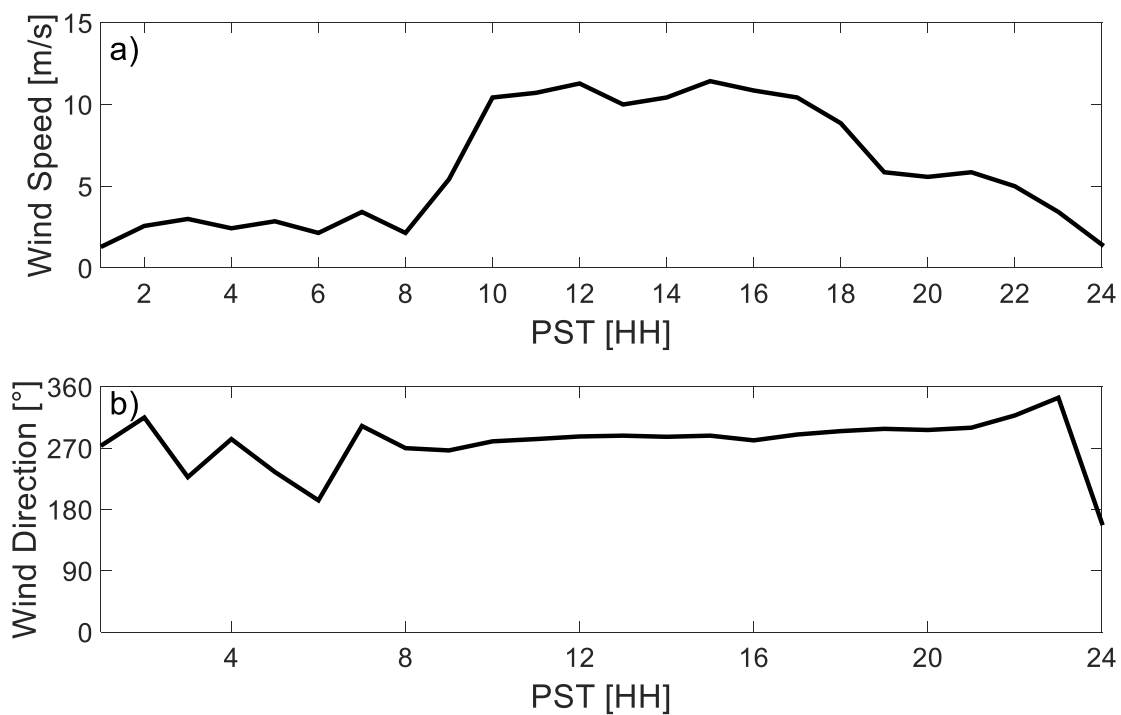
Figure 2.2. Surface wind speed magnitude **(a)** and direction **(b)** collected from METAR stations along the coast of California (117 -118°W, 32.5 - 33.3°N, see Fig. 1.2 (b)).

2.9 Acknowledgement

Chapter 3.   Turbulent and thermodynamic structure of STBL over coastal lands

3.1 Initial Profiles and Domain Setup

We simulate the CGILS S12 profile as it is representative of a well-mixed STBL (Fig. 3.1) and has been extensively reported on in the literature including as initializations for LES intercomparisons (Blossey et al., 2013; Zhang et al., 2012). Bretherton et al. (2013) ran LES and MLM initialized using the CGILS S12 profile to study the ocean STBL response to a variety of factors such as inversion strength, CO_2 concentration, and free tropospheric relative humidity. The CGILS S12 profile was developed for over-the-ocean model intercomparison studies; however, we do not anticipate any major differences in STBL profiles between the land and the ocean cases at night. While a weak temperature inversion may occur near the land surface due longwave cooling, the surface longwave cooling effect is greatly diminished due the presence of the cloud deck. There are two main deviations between real observations and the CGILS S12 profile: 1) variations in $\theta_l(z)$ and $q_T(z)$ within the STBL, and 2) thicker inversions. However, a LES based on sounding data with significant inversion thickness (but same inversion strength) showed a qualitatively similar evolution of the cloud layer as the CGILS S12 results (not shown). We therefore expect that the MLM and LES simulations based on the CGILS case increase our understanding of the processes behind the cloud dissipation in more realistic situations, similar to how the idealized MLM of stratocumulus by Nicholls (1984) generated insight in more realistic marine cloud layers. In any case, the departures

from the idealized cases noted earlier directly violate the assumptions of the MLM and therefore cannot be represented in a MLM framework.
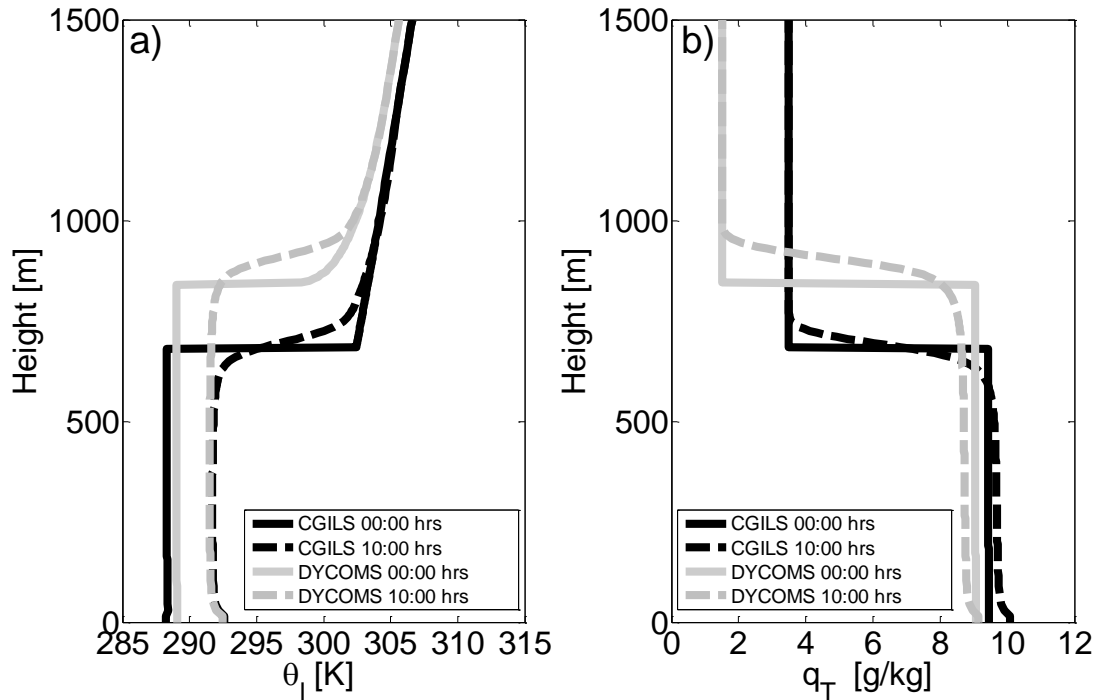
Figure 3.1. (a) Liquid potential temperature and **(b)** total water mixing ratio for CGILS S12 (black lines) and DYCOMS (grey lines) simulations at the start of the simulation (0000 LST, solid line) and at 1000 LST for the 1.0 Bowen ratio land case (dashed line).

We follow the numerical setup of the CGILS LES inter-comparison study: the vertical grid spacing is 10 m near the surface and refined (10% per layer) to obtain a 5 m resolution near the inversion, after which the grid is stretched again. The horizontal resolution is 25 m and the domain size is 2.4 km × 2.4 km in the horizontal and 1.6 km in the vertical (Blossey et al., 2013). In the CGILS S12 LES inter-comparison study, the different LES were run to equilibrium conditions over 10 days with an interactive radiation scheme, diurnally-averaged (constant) solar loading, and varying sea surface temperature (Blossey et al., 2013). Little or no precipitation was reported for the duration of the 10 day runs. Thus, we do not consider precipitation and employ a simplified

microphysics scheme, which consists of a simple pure condensation scheme with no rain. However, for section 3.3 we employ a two-moment rain scheme (a brief overview of the scheme is presented in Section 2.5) to test the effects of aerosol on cloud lifetime. Moreover, unlike the CGILS LES intercomparison, we allow the solar position to undergo a diurnal cycle over the 24 hour simulation starting at 00:00 PST. Large-scale mean subsidence is assumed to be steady as it typically does not vary significantly within 24 hours. The LES exhibit a characteristic "spinup" period during the first two hours (00:00 to 02:00 PST) during which the turbulent eddies develop as a result of the unstable conditions in the STBL due to cloud-top longwave cooling.

3.2 Turbulent and Thermodynamic Structures of STBL

We carry out LES initialized with CGILS profiles for five cases. The first three are for STBLs (i) over the ocean, (ii) over a wet land surface, and (iii) over a moderately dry land surface. The next two are "coupled" cases that include advection from ocean to land for (iv) a wet land surface and (v) a moderately dry land surface. In the non-coupled cases (i, ii, iii), we assume that horizontal heterogeneity is negligible and that the large-scale horizontal advection of heat and moisture does not affect either domain. Conversely, the coupled cases are motivated by actual coastal conditions where temperature and moisture gradients are significant and large-scale advection plays an important role in modulating the cloud lifetime.

3.2.1   Ocean case – baseline analysis

The ocean results confirm well-known stratocumulus behavior (Fig. 3.2 (a-c)). LWP varies diurnally over the ocean with maximum LWP occurring just before sunrise.

LWP decreases after sunrise due to solar radiative heating across the cloud layer that warms the boundary layer, causing cloud evaporation. Minimum LWP occurs at 13:40 LST and at a value of 31 gm^{-2}. The solar radiative heating additionally reduces the buoyancy flux (Fig. 3.3(a)) generated through longwave radiative cooling within the cloud layer and correspondingly reduces the turbulence within the STBL (reduction in vertical velocity variance, Fig. 3.3(b)). Thus, in addition to directly heating the STBL, solar radiative forcing indirectly affects LWP by reducing buoyancy flux generated within the cloud layer and thus entrainment of warm and dry air into the STBL.

3.2.2   Land cases without advection

At night over land, longwave cooling is the main factor driving turbulence and entrainment flux. During day, surface flux is an additional source of turbulence and heating and moistening. For the wet surface case (small Bowen ratio), the stratocumulus layer breaks up at 14:00 LST followed by partly cloudy conditions until sunset, after which the cloud cover returns to overcast (Fig. 3.2 (d-f)). The increase in surface latent heat flux after sunrise moistens the STBL (Fig. 3.2 (e)). The surface buoyancy flux keeps the STBL well-mixed despite the increase in inversion height by more than 100 m between sunrise and midday (Fig. 3.3 (c)).

For the dry surface case (large Bowen ratio), we observe rapid cloud dissipation soon after sunrise as the STBL substantially warms due to increasing surface sensible heat flux (Fig. 3.2 (g-i)). The sensible heat flux drives a strong increase in buoyancy flux (Fig. 6 (e)), resulting in a rapidly increasing entrainment velocity that incorporates more warm dry air aloft into the STBL and increasing the inversion height (Fig. 3.2 (g-i)).

Stronger warm thermals emitted by the dry land surface substantially enhance STBL height compared to the wet surface case. Pal and Haeffelin (2015) similarly found that inversion height evolution, measured using Lidar, had a higher correlation to land surface processes for drier soil conditions.

3.2.3   Land case with advection of oceanic air

At night the physics of the coupled cases are similar to the land cases with no large-scale horizontal advection as the pressure difference between the ocean and land air masses is small resulting in weak onshore winds (Fig. 2.2). During the day the prescribed horizontal winds increase as the pressure difference between the warm land and cool ocean air masses increases. Combined with the temperature and moisture differences between both air masses, the winds give rise to the advective tendencies. For the both coupled cases, the advection of ocean air cools the STBL resulting in thicker clouds compared to the cases with no large-scale horizontal advection. The thicker clouds attenuate net surface radiation reducing the surface buoyancy flux. As a result, of the decreased turbulence the coupled cases entrain less and therefore have lower inversion compared to the no-advection cases.

The cloud layer in the coupled wet land surface case exists in a cooler STBL and persists throughout the day (Fig. 3.2(j-l)), unlike the wet land surface case without advection. For the coupled dry surface case, the STBL does not warm as fast in the coupled case as in the uncoupled land case because cooling from large-scale advection acts to offset the strong warming effect of entrainment flux, surface sensible heat flux, and solar absorption. The reduced warming of the STBL results in slower cloud

dissipation. The cloud layer begins to thin at 09:00 LST resulting in a broken cloud deck (cumulus clouds) that persists until 12:30 LST, followed by clear skies (Fig. 3.2 (j-l)). This case is similar to stratocumulus clouds occurring over the relatively dry southern California coast during the summer months (Fig. 1.2).

Fluctuations in coastal wind speed and direction at sub-hour temporal and 1-10 km spatial scales resulting from variations in ocean-land pressure differences and synoptic conditions could be responsible for the observed day-to-day and spatial differences in stratocumulus cloud cover along the coast. This was observed during the VOCALS-Rex campaign in which horizontal advection had a strong effect on marine boundary layer height and the advection term ($\bar{v}$) could reach $15 \, \text{mms}^{-1}$ (Rahn and Garreaud, 2010).

Figure 3.2. Horizontally averaged temporal evolutions from LES of vertical profiles for the CGILS case of: (**a, d, g, j, m**) liquid potential temperature ($\overline{\theta_l}$), (**b, e, h, k, n**) total water mixing ratio ($\overline{q_T}$), (c, f, i, l, o) liquid water mixing ratio ($\overline{q_l}$). Results are provided for the ocean case (**a-c**), land case with Bowen ratio equal 0.1 (**d-f**), land case with Bowen ratio equal 1.0 (**g-i**), coupled case with horizontal advection representing the diurnally-varying sea breeze circulation and Bowen ratio equals to 0.1 (**j-l**), and coupled case with horizontal advection representing the diurnally-varying sea breeze circulation and Bowen ratio equals to 1.0 (**m-o**). While the LES domain reaches up to 1.6 km, only the lowest km is shown to focus on the boundary layer dynamics.

Figure 3.2. Horizontally averaged temporal evolutions from LES of vertical profiles for the CGILS case of: (**a, d, g, j, m**) liquid potential temperature ($\overline{\theta_l}$), (**b, e, h, k, n**) total water mixing ratio ($\overline{q_T}$), (**c, f, i, l, o**) liquid water mixing ratio ($\overline{q_l}$). Results are provided for the ocean case (**a-c**), land case with Bowen ratio equal 0.1 (**d-f**), land case with Bowen ratio equal 1.0 (**g-i**), coupled case with horizontal advection representing the diurnally-varying sea breeze circulation and Bowen ratio equals to 0.1 (**j-l**), and coupled case with horizontal advection representing the diurnally-varying sea breeze circulation and Bowen ratio equals to 1.0 (**m-o**). While the LES domain reaches up to 1.6 km, only the lowest km is shown to focus on the boundary layer dynamics.. continued.
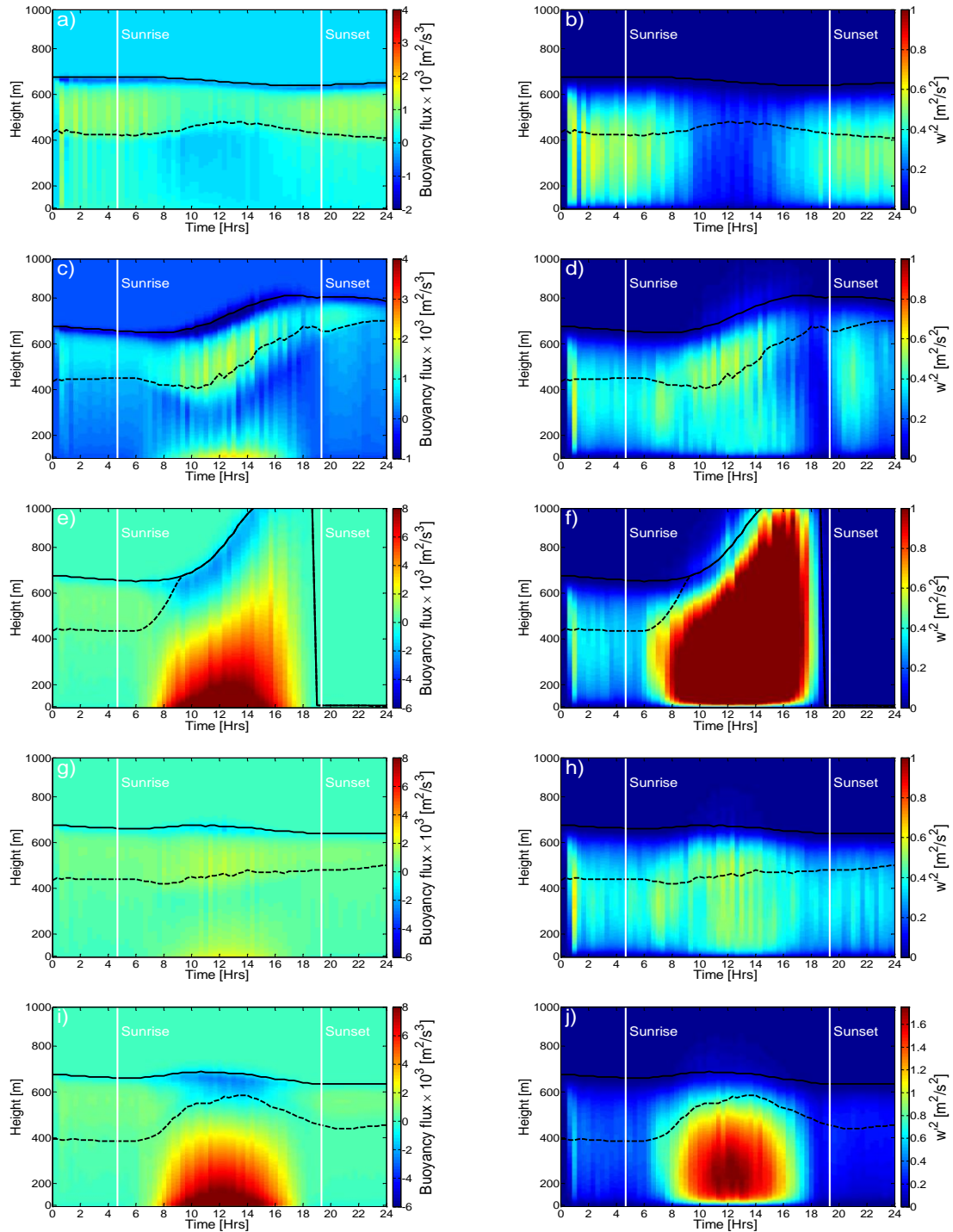
Figure 3.3. Horizontally averaged temporal evolutions from LES for the CGILS case of vertical profiles of (**a, c, e, g, i**) buoyancy flux and (**b, d, f, h, j**) vertical velocity variance ($\overline{w'^2}$). Results are shown for the ocean case (**a-b**), land case with Bowen ratio equal 0.1 (**c-d**), land case with Bowen ratio equal 1.0 (**e-f**), coupled case with horizontal advection representing the diurnally-varying sea breeze circulation and Bowen ratio equals to 0.1 (**g-h**), and coupled case with horizontal advection representing the diurnally-varying sea breeze circulation and Bowen ratio equals to 1.0 (**i-j**). While the LES domain reaches up to 1.6 km, only the lowest km is shown to focus on the boundary layer dynamics.

3.3 Effect of Aerosols on Stratocumulus Dissipation

In order to study the effects of aerosols on the stratocumulus cloud lifetime, two LES cases were run, one with prescribed CCN=100cm^{-3} and the second with CCN=1000cm^{-3} for the CGILS over the ocean case. The two-moment rain scheme scheme (Stevens and Seifert 2008) was employed in both runs and all other model specifications were the same as those outlined in section 3.2. Cloud dissipation times are not affected by CCN (Fig. 3.4 (a), (b)); however, LWP increases in the lower CCN case. This may seem odd at first since at lower CCN, water droplets have larger radii and thus more likely to precipitate (Fig. 3.4 (c), (d)). However, for thin clouds the precipitation flux is low and evaporates below the cloud layer, thereby increasing the instability at the bottom at the cloud. As a result, there are increased updrafts (Fig. 3.4 (e), (f)) which condense increasing the LWP (Lee et *al.*, 2009).
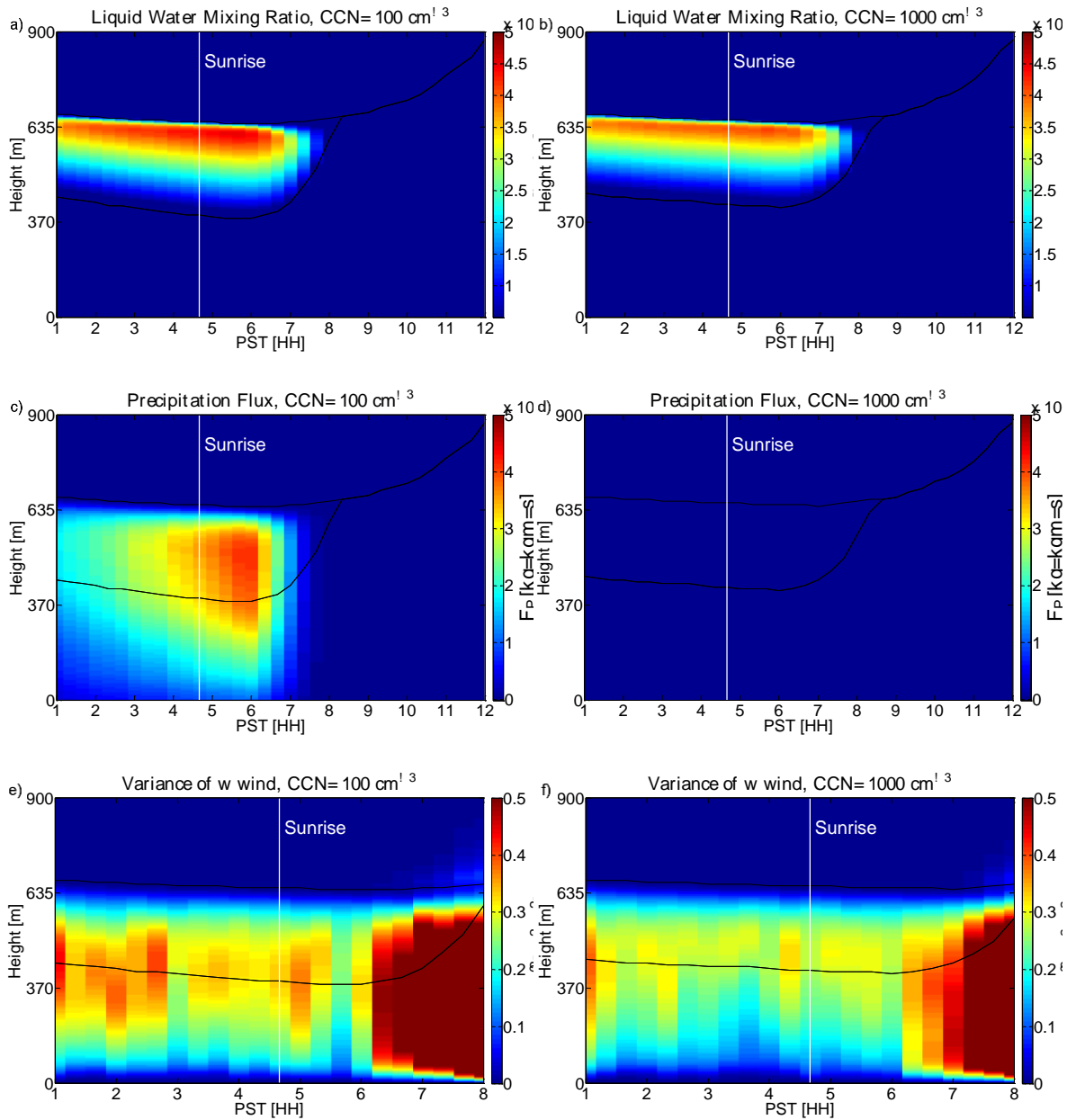
Figure 3.4. Horizontally averaged temporal evolutions of vertical profiles of liquid water mixing ratio (q_l) for **(a)** CCN=100cm^3 **(b)** CCN=1000cm^3. Horizontally averaged temporal evolutions of vertical profiles of precipitation flux (F_P) for **(c)** CCN=100cm^3 **(d)** CCN=1000cm^3. Horizontally averaged temporal evolutions of vertical profiles of vertical velocity variance ($\overline{w'^2}$) for **(e)** CCN=100cm^3 **(f)** CCN=1000cm^3.

3.4 Acknowledgment

Chapter 4.   Description of the Mixed Layer Model

The mixed layer model (MLM) is a thermodynamic model that has been applied to various atmospheric boundary layers, including dry convective and the STBL over the ocean (Bretherton and Wyant, 1997; Uchida et al., 2010; and Dal Gesso et al., 2014). The MLM solves the STBL mass, heat, and moisture budget equations (Lilly, 1968). Turbulence in the STBL is generated by either longwave radiative divergence across the cloud layer or by surface flux, and unstable conditions are assumed to prevail. Thus, the thermodynamic properties are assumed to follow adiabatic values, and the STBL is taken to be well-mixed (Albrecht et al., 1990; Caldwell et al., 2005). The well-mixed assumption breaks down when the STBL becomes decoupled due to a reduction in turbulence or an increase in the inversion height. We did not observe any significant deviations from the well-mixed assumption in this study since the inversions height does not exceed 1 km for the cases we have chosen. Furthermore, surface buoyancy flux in the land cases is a significant source of turbulence that keeps the STBL well-mixed. While the MLM framework and budget equations are taken from the literature, to improve the MLM accuracy for STBL over land several parameterizations are modified or introduced in the following sections.

4.1 Governing Equations

STBL inversion heights are usually much less than 2 km, hence we assume that the density remains constant up to the inversion height. The boundary layer columnar

mass ($m_{clm} = \bar{\rho}_{air} z_i$, where $\bar{\rho}_{air}$ represents the density of air, and z_i is the inversion height) balance equation is formulated as

$$\frac{\partial z_i}{\partial t} + \boldsymbol{v_H} \cdot \boldsymbol{\nabla} z_i = w_e + w_s(z_i) = w_e + D \times z_i. \tag{22}$$

The first and second term on the left hand-side of Eq. 22. represent the STBL columnar mass tendency and large scale horizontal advection, respectively. The first term on the right hand side of Eq. 22 represents the entrainment rate and the second the vertical large-scale wind component (subsidence), which is taken to be a function of inversion height and divergence (D). Note that $\bar{\rho}_{air}$ cancels out on both sides of the equation. The heat budget equation is formulated in terms of the liquid potential temperature ($\theta_l = \theta - \frac{1}{\Pi} \frac{L_v}{c_p} q_l$), where q_l represents the liquid water mixing ratio, θ represents the potential temperature, $\Pi = \left(\frac{P}{P_0}\right)^{R_d/C_p}$ is the Exner function, L_v is the latent heat of evaporation, c_p is the specific heat of air at constant pressure, and R_d is the dry air gas constant.

The MLM heat and moisture budget equations were derived in detail by Lilly (1968) and more recently by Caldwell et al. (2005). The final budget equations are expressed as

$$\frac{\partial \bar{\theta}_{l_{BL}}}{\partial t} + (\bar{v} \cdot \nabla_h \bar{\theta}_l)_{BL} = -\frac{\partial}{\partial z}\left(\overline{w'\theta_l'}(z) + \frac{F_{rad}(z)}{c_p \rho_{air}}\right)$$
$$= \frac{1}{z_i}\left(\overline{w'\theta_l'}_0 + w_e \Delta\theta_{l_i} - \frac{\Delta F_{rad}}{c_p \rho_{air}}\right), \tag{23}$$

$$\frac{\partial \overline{q_T}_{BL}}{\partial t} + (\bar{v} \cdot \nabla_h \overline{q_T})_{BL} = -\frac{\partial \overline{w'q_T'}(z)}{\partial z} = \frac{1}{z_i}\left(\overline{w'q_t'}_0 + w_e \Delta q_{t_i}\right), \tag{24}$$

where ∇_h is the horizontal divergence operator and $(\bar{\boldsymbol{v}} \cdot \nabla_h \bar{\theta}_l)_{BL}$, $(\bar{\boldsymbol{v}} \cdot \nabla_h \overline{q_T})_{BL}$ represent the large scale horizontal advection of heat and moisture into the boundary layer respectively. $\overline{w'\theta_l'}_0$ and $\overline{w'q_t'}_0$ are the surface sensible and latent heat flux, respectively. ΔF_{rad} represents the net radiation divergence across the cloud. Precipitation is neglected in the MLM formulation as the clouds are assumed to be thin enough not to precipitate or drizzle significantly. $\Delta\theta_l = \theta_{l_i} - \bar{\theta}_{l_{BL}}$ and $\Delta q_t = q_{t_i} - \overline{q_T}_{BL}$ represent the inversion jumps for heat and moisture, respectively (see also Section 4.3 later). $\bar{\theta}_{l_{BL}}$ and $\overline{q_T}_{BL}$ represent the boundary layer averaged liquid potential temperature and total water mixing ratio, respectively, while θ_{l_i} and q_{t_i} are evaluated just above the inversion height. Following the CGILS s12 specifications, we specify the linear free tropospheric liquid potential temperature profiles as

$$\theta_{l_i} = \theta_{l_i}(0) + (5.22 \text{ K km}^{-1})z_i, \tag{25}$$

with $\theta_{l_i}(0) = 299\text{K}$. q_{t_i} is constant in height above the inversion and is set as 3.5 g kg^{-1} for the CGILS case. In order to solve Eqs. 22 - 24, we will need to compute (i) surface flux, (ii) large-scale horizontal advection, (iii) radiative flux, and (iv) entrainment.

To compute surface flux we employ an LSM identical to that utilized in the LES (outlined in section 2.6.2). To obtain the large-scale advection terms, similar to the LES, we specify

$$\bar{\boldsymbol{v}} \cdot \nabla_h \bar{z}_l = \bar{\boldsymbol{v}} \cdot \left(\bar{z}_{l_{land}}(t) - \bar{z}_{l_{ocean}}(t)\right)/\Delta x, \tag{26.1}$$

$$\bar{\boldsymbol{v}} \cdot \nabla_h \bar{\theta}_l = \bar{\boldsymbol{v}} \cdot \left(\bar{\theta}_{l_{land_{BL}}}(t) - \bar{\theta}_{l_{ocean_{BL}}}(t)\right)/\Delta x, \tag{26.2}$$

$$\bar{\boldsymbol{v}} \cdot \nabla_h \overline{q_T} = \bar{\boldsymbol{v}} \cdot \left(\overline{q_T}_{land_{BL}}(t) - \overline{q_T}_{ocean_{BL}}(t)\right)/\Delta x, \tag{26.3}$$

where $\bar{\theta}_{l_{ocean_{BL}}}(t), \overline{q_T}_{ocean_{BL}}(t)$ and $\bar{z}_{l_{ocean}}(t)$ represent the ocean boundary layer liquid potential temperature, total water mixing ratio, and inversion height, respectively, obtained from the ocean MLM case. $\bar{\theta}_{l_{land_{BL}}}(t), \overline{q_T}_{land_{BL}}(t)$, and $\bar{z}_{l_{land}}(t)$ are computed dynamically within the MLM. Note that the MLM is a zero-dimensional model and hence the temperature and moisture are values are assumed to be height independent within the boundary layer.

4.2 Radiation Parameterization

An analytical radiation scheme that models longwave radiation (F_{lw}) as a function of the STBL LWP and temperature is coupled to the MLM. It is different from the radiation scheme employed in the LES since the latter is too computationally expensive to be coupled to the MLM. The radiation scheme in the MLM is similar to that used in the Global Energy and Water Cycle Experiment (GEWEX) Cloud System Study (GCSS; Bretherton et al. 1999) which was found to yield accurate fluxes for liquid clouds (Larson and Kotenberg, 2007). However, the GEWEX radiation parameterization does not account for the cloud base and cloud top temperature changes that are crucial for the STBL occurring over land, where there is significant heating from the surface. Thus, we modified the radiation scheme to be a function of these temperatures in the MLM.

To develop the LW radiation parameterization, we first assume an idealized cloud with the following properties: horizontally infinite uniform slab, constant asymmetry factor (g), single scattering albedo (ω), mass extinction cross section (m) and temperature (T). Following Goody (1995) and Larson and Kotenberg (2007) the net radiative flux is expressed as

$$\frac{d^2F}{d\tau^2} = \alpha^2 F \, , \alpha^2 = 3(1-\omega)(1-\omega g),$$

(27)

with the following boundary conditions at the cloud top

$$\frac{dF}{d\tau}\bigg|_{\tau=0} = 4\pi(1-\omega)\left[\frac{F_{\tau=0}}{2\pi} - (B_{cld} - B_t)\right],$$

(28)

and the cloud bottom

$$\frac{dF}{d\tau}\bigg|_{\tau=\tau_b} = 4\pi(1-\omega)\left[(B_b - B_{cld}) - \frac{F_{\tau=\tau_b}}{2\pi}\right].$$

(29)

B_b is the upwelling black body radiance at the cloud base $(B_b = \left(\frac{\sigma}{\pi}\right)T_{srf}{}^4)$, where T_{srf} is

the surface temperature that is determined dynamically from the land surface model .

B_{cld} is the black body emitted radiance from the cloud $(B_{cld} = \left(\frac{\sigma}{\pi}\right)T_{cld}{}^4)$, where T_{cld} is

the effective cloud temperature that is obtained dynamically from the MLM. B_t is the

downwelling black body radiance at the cloud top $(B_t = \left(\frac{\sigma}{\pi}\right)T_t{}^4)$, where T_t is effective

temperature of the air just above the cloud and σ is the Stefan-Boltzmann constant. The

solution to Eq. 27 determined by inspection is

$$F = Le^{\alpha\tau} + Me^{-\alpha\tau}.$$

(30)

By substituting Eq.30 into the boundary conditions (Eqs. 28 29), L and M are

determined as

$$L = \gamma[(B_{cld} - B_t)c_1 e^{-\alpha\tau_b} + (B_0 - B_{cld})c_2],$$

$$M = \gamma[(B_{cld} - B_t)c_2 e^{\alpha\tau_b} + (B_0 - B_{cld})c_1],$$

(31)

where,

$$\gamma = -\frac{4\pi(1-\omega)}{c_1^2 e^{-\alpha\tau_b} - c_2^2 e^{\alpha\tau_b}},$$

(32)

and

$$c_1 = \alpha - 2(1-\omega),$$

$$c_2 = \alpha + 2(1-\omega).$$

(33)

Finally, following Stevens et al. (2005), Eq. 29 is augmented to include cooling of the air above the cloud top as

$$F_{LW} = Le^{\alpha\tau} + Me^{-\alpha\tau} + \rho_{air,i} c_p D \alpha_z \left[\frac{(z-z_i)^{4/3}}{4} + z_i(z-z_i)^{1/3} \right],$$

(34)

where $\rho_{air,i}$ is the density of air at the inversion, and $\alpha_z = 1\mathrm{m}^{-4/3}$. $D = 4.86 \times 10^{-6}$, and 3.75×10^{-6} which represents large-scale divergence for the CGILS and DYCOMS cases, respectively. Thus, the first term in 34 represents the cloud top cooling, the second the cloud-base warming, and the third the cooling in the troposphere and is only applied above the inversion. The parameterized longwave radiation was found to be in agreement with that computed in LES using the Monte-Carlo spectral radiation scheme (Pincus and Steven, 2008, Fig. 4.1).
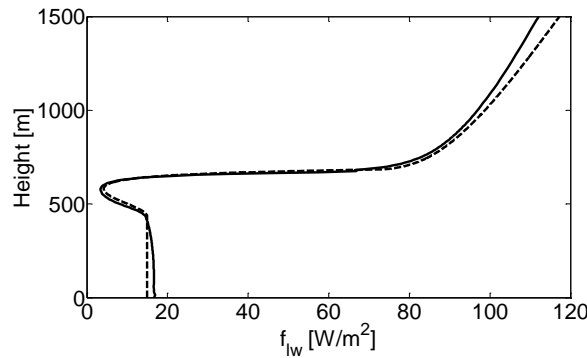
Figure 4.1. Comparison of longwave radiation derived from LES (solid) and MLM (dashed) computed using the CGILS S12 temperature and liquid water vertical profiles.

The net downward solar radiation (F_{sw}) is derived using the analytical solution of the Delta-Eddington approximation (Joseph et al., 1976; Shettle and Weinman 1970; Duynkerke et al., 2004) and is expressed as

$$F_{SW}(z) = \frac{4}{3}F_0\left[p\{A_1 e^{-k\tau(z)} - A_2 e^{k\tau(z)}\} - \beta e^{-\frac{\tau(z)}{\mu_0}}\right] + \mu_0 F_0 e^{-\frac{\tau(z)}{\mu_0}},\qquad (35)$$

where $\mu_0 = cos\theta$, θ is the solar zenith angle. $F_0 = 1100\ \text{Wm}^{-2}$ is the downward solar radiation at the cloud top. Constants A_1 and A_2 are computed based on the boundary conditions, p and β are functions of the asymmetry factor and single scattering albedo. $\tau(z)$ is the optical depth and is defined as

$$\tau(z) = \frac{3}{2}\frac{LWP}{r_e \rho_w},\qquad (36)$$

where r_e is the cloud droplet effective radius, i.e. the ratio of the third moment to the second moment of the droplet size distribution. For marine boundary layer clouds, we chose $r_e = 10\ \mu\text{m}$, which was observed for stratocumulus over the Pacific Ocean off the coast of California (Duda et al., 1991). ρ_w is the liquid water density.

4.3 Entrainment Parametrization

We assume that the STBL is a shear-free, convective boundary layer. Under that assumption, the main driver of turbulence in a STBL over ocean is cloud top longwave radiative cooling (also see section 5). For a STBL over land, the main source of turbulence shifts from cloud top longwave radiative cooling during night to surface generated buoyancy during day (refer to section 5). In order to parametrize entrainment velocity for both cases, we first formulate the total velocity scale as a linear combination

of the buoyancy flux generated in the cloud layer due to the radiative divergence and the buoyancy flux generated at the surface as

$$w_T^{*3} = w_{rad}^{*3} + w_{srf}^{*3} = 2.5 \frac{g}{\theta_{v0}} \int_{z_b}^{z_i} \overline{w'\theta_v'} \, dz + 1.25 \frac{gz_i}{\theta_{v0}} \overline{w'\theta_v'}_s, \quad (37)$$

where $\overline{w'\theta_v'}_s$ is the virtual potential flux evaluated at the surface, and θ_{v0} is the reference virtual potential temperature taken to be 290K. Fang et al. (2014a) also formulated a total velocity scale as linear combination of the buoyancy flux generated at the surface and the radiative convective velocity. Utilizing ground measurements, Fang et al. (2014a) were able to show that the total convective velocity scale w_T^{*3} tracked the turbulence forcing well throughout the day. Furthermore, they found that turbulence at night is mainly driven by the cloud top cooling characterized by w_r^{*3} whereas turbulence during the day is driven by both cloud top cooling and surface flux. Rather than use net radiative flux divergence as did Fang et al. (2014a) ($w_r^{*3} = \frac{gz_i}{\rho c_p \theta_{v0}}(-\Delta F_r)$), we use the in-cloud buoyancy flux as a measure of the turbulence generated by the net longwave radiative flux divergence across the cloud layer as well as the turbulence generated by latent heat release in updrafts within the cloud layer. We hypothesize that the integral of the in-cloud buoyancy flux is a more appropriate velocity scale considering that cloud-top longwave emission becomes insensitive to LWP changes for thick clouds (Kazil et al., 2015). Thus, for sufficiently thick clouds, additional turbulence generation and boundary layer growth is produced by latent heat release in updrafts within the cloud layer rather than increased longwave emission.

Next, we parameterize the cloud top entrainment velocity as

$$w_e = A\left(\frac{w^*_{rad}}{Ri_{rad}} + \frac{w^*_{srf}}{Ri_{srf}}\right),$$

(38)

where $Ri_{rad} = \frac{gz_{cld}\Delta\theta_{vi}}{\theta_{v0}w^{*2}_{rad}}$ and $Ri_{srf} = \frac{gz_i\Delta\theta_{vi}}{\theta_{v0}w^{*3}_{srf}}$ are the bulk Richardson numbers for the

radiative driven turbulence and surface driven turbulence, respectively. z_{cld} represents

the cloud thickness and a floor of $z_{cld} = 0.1 \times z_i$ is set for when the cloud dissipates.

Cloud thickness is defined as the difference between the inversion height and the cloud

base height, defined as the height corresponding to the maximum liquid potential

temperature gradient and the minimum height at which the liquid water mixing ratio is

greater than zero, respectively. $\Delta\theta_{vi}$ is the inversion jump in virtual potential temperature.

A represents the entrainment efficiency and is expressed as

$$A = a_1\left\{1 + a_2\left(1 - \frac{\Delta_m b}{\Delta_i b}\right)\right\},$$

(39)

where the term $a_2\left(1 - \frac{\Delta_m b}{\Delta_i b}\right)$ accounts for the evaporative enhancement of entrainment.

$\Delta_m b$ is the linearized average buoyancy of all possible mixtures between purely clear

tropospheric air and purely cloudy air, relative to the cloudy air (refer to appendix B of

Grenier and Bretherton (2001) for a detailed derivation and description of Eq. 39). $\Delta_i b$ is

the buoyancy jump across the inversion. $a_1 = 0.2$ and $a_2 = 60$ are based on fits to

observations and laboratory experiments (Nicholls and Turton, 1986). As the cloud

begins to dissipate, the evaporative enhancement goes to 0 and A goes to 0.2, which is the

entrainment efficiency for a dry mixed layer. Thus, the entrainment parametrization we

propose is a linear combination of two regimes: the first occurs at night and is driven by

longwave cooling with turbulence mainly concentrated in the cloud layer; the second

occurs at day and is driven by surface heating with turbulence that is almost an order of magnitude stronger and encompasses the entire boundary layer.

Next, in order to solve for the in-cloud virtual potential temperature flux we equate it to the conserved variable fluxes as follows

$$\overline{w'\theta_v'}(z) = C_1\overline{w'\theta_l'}(z) + C_2\overline{w'q_T'}(z) \qquad z_b < z < z_i, \tag{40}$$

where $C_1 = \dfrac{1+\frac{\overline{q_s}}{\epsilon}-\overline{q_T}+\frac{\overline{\theta}}{\epsilon}\left(\frac{dq_s}{dT}\right)}{1+\frac{L_v}{c_p}\left(\frac{dq_s}{dT}\right)} \approx 0.5$ and $C_2 = \dfrac{L_v}{c_p}\left(\dfrac{1+\frac{\overline{q_s}}{\epsilon}-\overline{q_T}+\frac{\overline{\theta}}{\epsilon}\left(\frac{dq_s}{dT}\right)}{1+\frac{L_v}{c_p}\left(\frac{dq_s}{dT}\right)}\right) - \overline{\theta} \approx 970$ K (refer to

Stevens 2002 for a more detailed derivation of the constants). In order for the STBL to remain well mixed, $\dfrac{\partial\overline{\theta_l}_{BL}}{\partial t} + (\overline{\boldsymbol{v}}\cdot\nabla_h\overline{\theta_l})_{BL}$ and $\dfrac{\partial\overline{q_T}_{BL}}{\partial t} + (\overline{\boldsymbol{v}}\cdot\nabla_h\overline{q_T})_{BL}$ must be height independent. In order to satisfy Eqs. 23and 24, $\overline{w'\theta_l}'(z) + \dfrac{F_{rad}(z)}{c_p\rho_{air}}$ and $\overline{w'q_T}'(z)$ must therefore be linear functions of height in the STBL and can be expressed as follows:

$$\overline{w'\theta_l'}(z) + \frac{F_{rad}(z)}{c_p\rho_{air}} = \left(1 - \frac{z}{z_i}\right)\frac{SHF + F_{lw_0}}{\rho c_p} - \frac{z}{z_i}\left(w_e\Delta\theta_{l_i} - \frac{F_{lw_i}}{\rho c_p}\right), \tag{41}$$

$$\overline{w'q_T'} = \left(1 - \frac{z}{z_i}\right)\frac{LHF}{\rho L_v} - \frac{z}{z_i}w_e\Delta q_{T_i}. \tag{42}$$

In order to define the jumps in heat and moisture across the inversion ($\Delta\theta_{l_i}, \Delta\theta_{vi}$ and Δq_{t_i}), we must determine the thickness of the entrainment zone (also referred to as the inversion layer or interfacial layer, Fig. 3.1). The entrainment zone is the region where air from the overlying free atmosphere is entrained across the inversion into the convectively mixed STBL. The entrainment is fed by the penetration of thermals from the STBL into the stably stratified air above the inversion that cause the descent of more buoyant air aloft into the STBL.

The thickness of the entrainment zone is an active research topic. Studies conducted by Sullivan et al. (1998), and Fedorovich et al. (2004) on clear convectively driven boundary layers considered a single layer to exist within the entrainment zone. More recently, Garcia and Mellado (2014) showed that the entrainment zone consists of two overlapping sublayers: an upper sublayer that is dominated by thermals and stratification, and a lower layer dominated by troughs (crests of undulations within the entrainment zone at the cloud top) of mixed fluid. In the case of the STBL over land, defining the entrainment zone is further complicated by an inversion that is rapidly weakening due to surface heating and rising in height due to increased encroachment fed by the enhanced turbulence resulting from the land surface flux (Figs. 3.2 (d-i), and Figs. 3.3 (c-f)). Due to the uncertainties regarding the definition of entrainment zone heights and insufficient resolution in LES to accurately represent the physical processes occurring in the entrainment zone, we utilize the entrainment zone thickness as a tuning parameter to match LES derived entrainment velocity with that of the MLM. Thus, we set two different entrainment zone heights: one for the cloud top radiative cooling contribution and another for the surface flux contribution, equal to 3.4 m and 7.5 m, respectively. The entrainment zone heights remain constant throughout the simulation and do not change between cases.

4.4 Cloud Thickness and Liquid Water Tendencies

Temporal evolution of cloud thickness (z_{cld}) can be formulated as follows:

$$\frac{\partial z_{cld}}{\partial t} = \frac{\partial z_i}{\partial t} - \frac{\partial z_b}{\partial t}$$

(**43**)

where z_b is the cloud base height corresponding to the height at which the saturation mixing ratio (q_s) is equal to the total water mixing ratio:

$$q_s(T_{cb}, P_{cb}) = q_t, \tag{44}$$

where T_{cb}, P_{cb} are the temperature and pressure values evaluated at the cloud base height. The temporal evolution of cloud top height can be obtained from the mass balance (Eq. 22). The tendency of the cloud base height can be formulated in terms of liquid potential temperature and total mixing ratio as (Wood 2007)

$$\frac{\partial z_b}{\partial t} = \frac{\partial z_b}{\partial \theta_l}\frac{\partial \theta_l}{\partial t} + \frac{\partial z_b}{\partial q_t}\frac{\partial q_t}{\partial t}. \tag{45}$$

Liquid water path (LWP) is defined as:

$$LWP = \int_0^{z_i} q_l dz = \int_{z_b}^{z_i} q_l dz. \tag{46}$$

The liquid water content in a layer of cloud is assumed to increase linearly with height z above the cloud base (Albrecht 1990), and can be expressed as

$$q_l(z) = f_{ad}\Gamma_{ad}z, \tag{47}$$

where $\Gamma_{ad}(T, P)$ is the adiabatic rate of increase of liquid water content with respect to height and f_{ad} is the degree of adiabacity ($0 < f_{ad} < 1$). Substituting Eq. 47 into 46 :

$$LWP = \int_{z_b}^{z_i} f_{ad}\Gamma_{ad}z dz = \frac{1}{2}f_{ad}\Gamma_{ad}z_{cld}^2, \tag{48}$$

where $\Gamma_{ad}(T, P)$ is a weak function of temperature and pressure and is taken to be constant with height for a shallow cloud deck (Albrecht 1990). Finally, the LWP tendency can be expressed in terms of the cloud thickness tendency as:

$$\frac{\partial LWP}{\partial t} = f_{ad}\Gamma_{ad}h\frac{\partial z_{cld}}{\partial t}. \tag{49}$$

4.4.1 Response of Cloud Base Height to Changes in Boundary Layer Moisture Content

In the case where there is a change in total water mixing ratio (dq_T) and liquid potential temperature is kept constant $(d\theta_l = 0$, Fig. 4.2), from the definition of cloud base height, dq_T is equal to the change in saturation mixing ratio at the cloud base :

$$dq_t = dq_s(T_{cb}, P_{cb}).$$

(50)

The total differential of the saturation mixing ratio is defined as follows:

$$dq_s = \frac{\partial q_s}{\partial T} dT + \frac{\partial q_s}{\partial P} dP.$$

(51)

Thus, the response cloud base height to a change in the total water mixing ratio is formulated as:

$$\frac{dq_t}{dz_b} = \frac{dq_s(T_{cb}, P_{cb})}{dz_{cb}} = \frac{\partial q_s}{\partial T} \frac{dT_{cb}}{dz_b} + \frac{\partial q_s}{\partial P} \frac{dP_{cb}}{dz_b}.$$

(52)

Taking the derivative the saturation mixing ratio with respect to temperature results in $\frac{\partial q_s(z_b)}{\partial T_b} = \varepsilon \frac{\partial e_s}{\partial T_b} \frac{1}{P} \left(1 + \frac{e_s}{P}\right)$. Utilizing the Clausius Clapeyron equation $\left(\frac{\partial e_S}{\partial T_b} = \frac{L_v e_s}{R_v T_b{}^2}\right)$ and assuming that $\frac{e_s}{P} \ll 1$:

$$\frac{\partial q_s(z_b)}{\partial T} = \frac{L_v q_t}{R_v T_{cb}{}^2}.$$

(53)

Since there is no addition of heat to the boundary layer (Fig. 4.2) , the dry adiabatic lapse rate can be used to formulate $\frac{dT_{cb}}{dz_b}$ as follows:

$$\frac{dT_{cb}}{dz_b} = -\frac{g}{c_p}.$$

(54)

Taking the partial derivative of the saturation mixing ratio ($q_s = \varepsilon \frac{e_S}{P - e_s}, \varepsilon = \frac{M_v}{M_d} = 0.622$)

with respect to temperature and assuming that $p \gg e_S$:

$$\frac{\partial q_s(z_b)}{\partial P} \approx -\frac{q_t}{P_{cb}}.$$

(55)

Applying the hydrostatic balance at the cloud base:

$$\frac{dP_{cb}}{dz_b} \approx -\frac{P_{cb} g}{R_d T_{cb}}.$$

(56)

Finally, substituting Eqs. 53 54, 55 and 56 into Eq. 52 :

$$\frac{dz_b}{dq_t} = \frac{R_d T_{cb}}{g q_t} \left(1 - \frac{L_v R_d}{c_p R_v T_{cb}}\right)^{-1}$$

(57)

a)
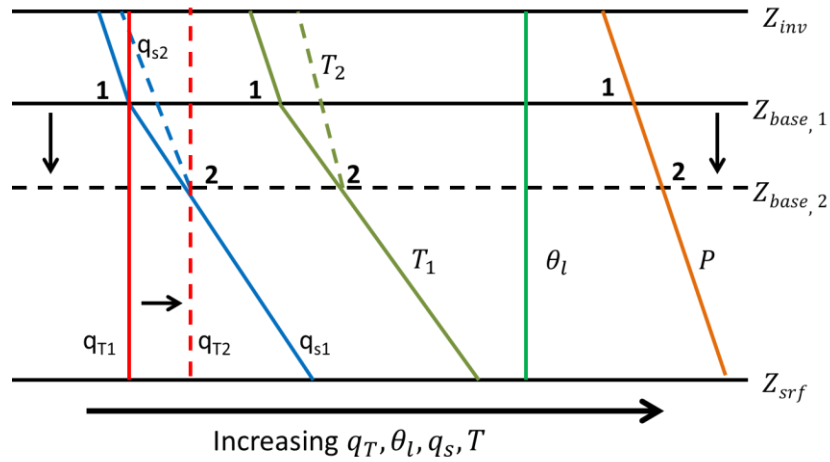
b)
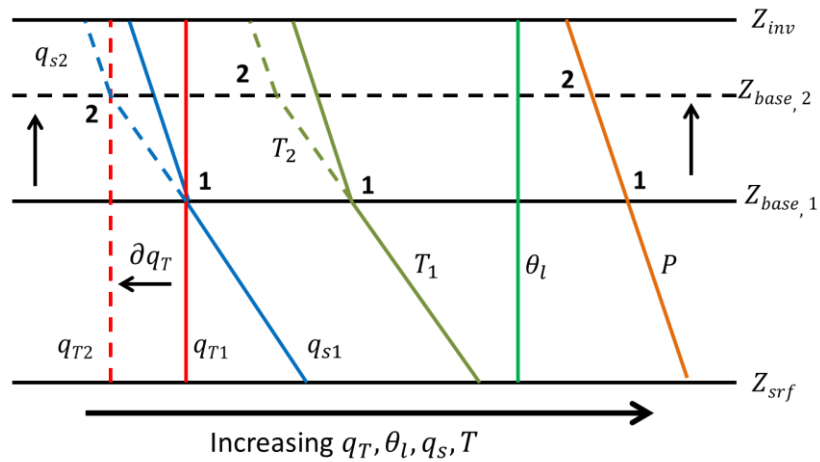
Figure 4.2.(a) response of cloud base height to an *increase* in total water mixing ratio, **(b)** response of cloud base height to a *decrease* in total water mixing ratio. Solid lines ("1") show initial profiles and dashed lines ("2") show the response

4.4.2 Response of Cloud Base Height to Changes in Boundary Layer Heat Content

In this case the liquid potential temperature $(d\theta_l)$ changes and the total water mixing ratio is kept constant $(dq_t = 0$, Fig. 4.2). Since $q_l = 0$ at the cloud base, $d\theta_l$ at the cloud base is

$$d\theta_l = \frac{dT_{cb}}{\Pi_1} - \frac{T_1}{\Pi_1^2} d\Pi_{cb},$$

(58)

where dT_{cb} is the difference in temperature at the different cloud bases. It is important to note that dT_{cb} does not follow either the dry or moist adiabatic lapse rate as the vertical temperature profile is shifted due to the addition of heat in the boundary layer (Fig. 4.2). $d\Pi_{cb}$ is the difference in Exner function values at the different cloud base heights. Utilizing the definition of the Exner function and assuming the atmosphere is in hydrostatic balance (Eq. 56), Eq. 58 is then formulated in terms of dz_{cb} as,

$$d\theta_l = \frac{dT_{cb}}{\Pi_1} - \frac{R_d T_1}{c_p P_1 \Pi_1} dP_{cb} = \frac{1}{\Pi_1}\left(dT_{cb} + \frac{g}{c_p} dz_{cb}\right),$$

$$\frac{d\theta_l}{dz_b} = \frac{1}{\Pi_1}\left(\frac{dT_{cb}}{dz_b} + \frac{g}{c_p}\right).$$

(59)

Since q_T is constant, q_s at the cloud base remains constant as well ($q_{s1} = q_{s2}$). The saturation mixing ratios at the cloud base are then expressed as: $q_{s1} = \frac{e_{s1}}{P_1} = \frac{e_{s2}}{P_2}$; hence, $\frac{de_s}{e_{s1}} = \frac{dP}{P_1}$. Utilizing the definition of the saturation water vapor pressure ($e_s = e_{s,tr}\exp\left[\frac{L_v}{R_v}\left(\frac{1}{T_{tr}} - \frac{1}{T}\right)\right]$ and the hydrostatic balance assumption, an expression for $\frac{dT_{cb}}{dz_b}$ is derived as

$$de_{s_{cb}} = e_{s,tr} \frac{L_v}{R_v T_1^2} \exp\left[\frac{L_v}{R_v}\left(\frac{1}{T_{tr}} - \frac{1}{T}\right)\right] dT_{cb} = \frac{L_v e_{s1}}{R_v T_{cb}^2} dT_{cb},$$

$$\frac{de_{s_{cb}}}{e_{s1}} = \frac{dP_{cb}}{P_1} = -\frac{g}{R_d T_{cb}} dz_b,$$

$$\frac{de_{s_{cb}}}{e_{s1}} = \frac{L_v}{R_v T_1^2} dT_{cb} = -\frac{g}{R_d T_{cb}} dz_b,$$

$$\frac{dT_{cb}}{dz_b} = -\frac{g R_v T_{cb}}{R_d L_v}. \tag{60}$$

Substituting Eq. 60 into 59 :

$$\frac{d\theta_l}{dz_b} = \frac{g}{c_p \Pi_1}\left(1 - \frac{c_p R_v T_{cb}}{R_d L_v}\right). \tag{61}$$

4.5 Factors Contributing to Cloud dissipation

In order to study how different physical processes such as entrainment and radiation divergence affect cloud lifetime, the MLM equations (Eqs. 22-24) are coupled with the cloud thickness (z_{cld}) tendency equation as

$$\frac{\partial z_{cld}}{\partial t} = \frac{\partial z_i}{\partial t} - \frac{c_p \Pi_{b,1}}{g}\left(1 - \frac{c_p R_v T_{b,1}}{R_d L_v}\right)^{-1} \frac{\partial \theta_l}{\partial t} - \frac{R_d T_{b,1}}{g q_t}\left(1 - \frac{L_v R_d}{c_p R_v T_{b,1}}\right)^{-1} \frac{\partial q_t}{\partial t}, \tag{62}$$

where $T_{b,1}$ is the cloud base temperature and $\Pi_{b,1} = \left(\frac{P_{b,1}}{P_0}\right)^{R_d/C_p}$ is the Exner function.

Substituting the inversion height and conserved variable tendencies (Eqs. 22-24) into Eq. 62

$$\frac{\partial z_{cld}}{\partial t} = w_e + w_s(z_i) - \boldsymbol{v_H} \cdot \boldsymbol{\nabla} z_i$$

$$- \frac{c_p \Pi_{b,1}}{z_i g}\left(1 - \frac{c_p R_v T_{b,1}}{R_d L_v}\right)^{-1}\left(-z_i(\bar{\boldsymbol{v}} \cdot \nabla_h \bar{\theta_l})_{BL} + \overline{w'\theta_l'}_0 + w_e \Delta \theta_{l_i}\right.$$

$$\left.- \frac{\Delta F_{rad}}{c_p \rho_{air}}\right) \tag{63}$$

$$- \frac{R_d T_{b,1}}{z_i g q_t}\left(1 - \frac{L_v R_d}{c_p R_v T_{b,1}}\right)^{-1}\left(-z_i(\bar{\boldsymbol{v}} \cdot \nabla_h \overline{q_T})_{BL} + \overline{w'q_t'}_0\right.$$

$$\left.+ w_e \Delta q_{t_i}\right).$$

We then split Eq. 63 into the five different physical factors contributing to the cloud thickness tendency as

$$entrainment\ flux$$

$$= w_e - \frac{c_p \Pi_{b,1}}{z_i g}\left(1 - \frac{c_p R_v T_{b,1}}{R_d L_v}\right)^{-1} w_e \Delta \theta_{li} \tag{64.1}$$

$$- \frac{R_d T_{b,1}}{z_i g q_t}\left(1 - \frac{L_v R_d}{c_p R_v T_{b,1}}\right)^{-1} w_e \Delta q_{ti},$$

$$surface flux = - \frac{c_p \Pi_{b,1}}{z_i g}\left(1 - \frac{c_p R_v T_{b,1}}{R_d L_v}\right)^{-1} \overline{w'\theta_l'}_0$$

$$- \frac{R_d T_{b,1}}{z_i g q_t}\left(1 - \frac{L_v R_d}{c_p R_v T_{b,1}}\right)^{-1} \overline{w'q_t'}_0, \tag{64.2}$$

$$radiation = \frac{c_p \Pi_{b,1}}{z_i g}\left(1 - \frac{c_p R_v T_{b,1}}{R_d L_v}\right)^{-1}\frac{\Delta F_{rad}}{c_p \rho_{air}}, \tag{64.3}$$

$$subsidence = w_s(z_i), \tag{64.4}$$

$$advection = -\boldsymbol{v_H} \cdot \boldsymbol{\nabla} z_i + \frac{c_p \Pi_{b,1}}{g}\left(1 - \frac{c_p R_v T_{b,1}}{R_d L_v}\right)^{-1}(\bar{\boldsymbol{v}} \cdot \nabla_h \bar{\theta_l})_{BL}$$

$$+ \frac{R_d T_{b,1}}{g q_t}\left(1 - \frac{L_v R_d}{c_p R_v T_{b,1}}\right)^{-1}(\bar{\boldsymbol{v}} \cdot \nabla_h \overline{q_T})_{BL}.$$

(64.5)

4.6 Acknowledgment

Chapter 5.   Factors Controlling Stratocumulus Cloud Lifetime

Similar to Section 3, we present a comparison between LES and MLM for five cases: (i) ocean case, (ii) relatively wet land surface case ($\beta = 0.1$), (iii) moderately dry land surface case ($\beta = 1.0$), (iv) relatively wet land surface case ($\beta = 0.1$) "coupled" to the ocean STBL by horizontal advection, and (v) moderately dry surface case ($\beta = 1.0$) "coupled" to the ocean STBL by horizontal advection. The analysis is performed using both the CGILS and DYCOMS initial profiles (refer to Stevens et al., (2003, 2005) for an overview of the DYCOMS field campaign and LES intercomparison). For each of the cases outlined, we compare the MLM output against the LES results up to the time of cloud dissipation since we are interested in studying the factors affecting cloud lifetime.

For the all cases, the MLM and LES results are in good agreement (Fig. 5.1). In all LES cases, there is a drop in LWP during 00:00 to 02:00 LST possibly due to spinup effects; consequently, LWP in LES is slightly lower than that of the MLM. The MLM results better match those of the LES when the MLM was initiated with LES thermodynamic profiles sampled after the spin up period (not shown). For the ocean case, the MLM simulated entrainment velocity matches that of the LES relatively well; furthermore, the entrainment velocity parameterization is able to simulate the decrease in entrainment velocity magnitude due to the reduction in boundary layer turbulence resulting from solar absorption.

In the wet land surface case, the higher LWP in the MLM attenuates the net surface radiation, thereby reducing the surface flux (Fig. 5.1(f)). In particular, the lower

surface latent heat flux in the MLM results in lower STBL moisture content later in the day compared to the LES (Fig. 5.1 (i)). In both land surface cases, we observe entrainment velocities during the day that are about a factor of three larger than the over the ocean case. For the coupled cases, we observe slightly weaker entrainment velocities particularly for the coupled wet land surface case. The thicker clouds in the coupled cases attenuate the net surface radiation thereby decreasing the surface buoyancy flux.
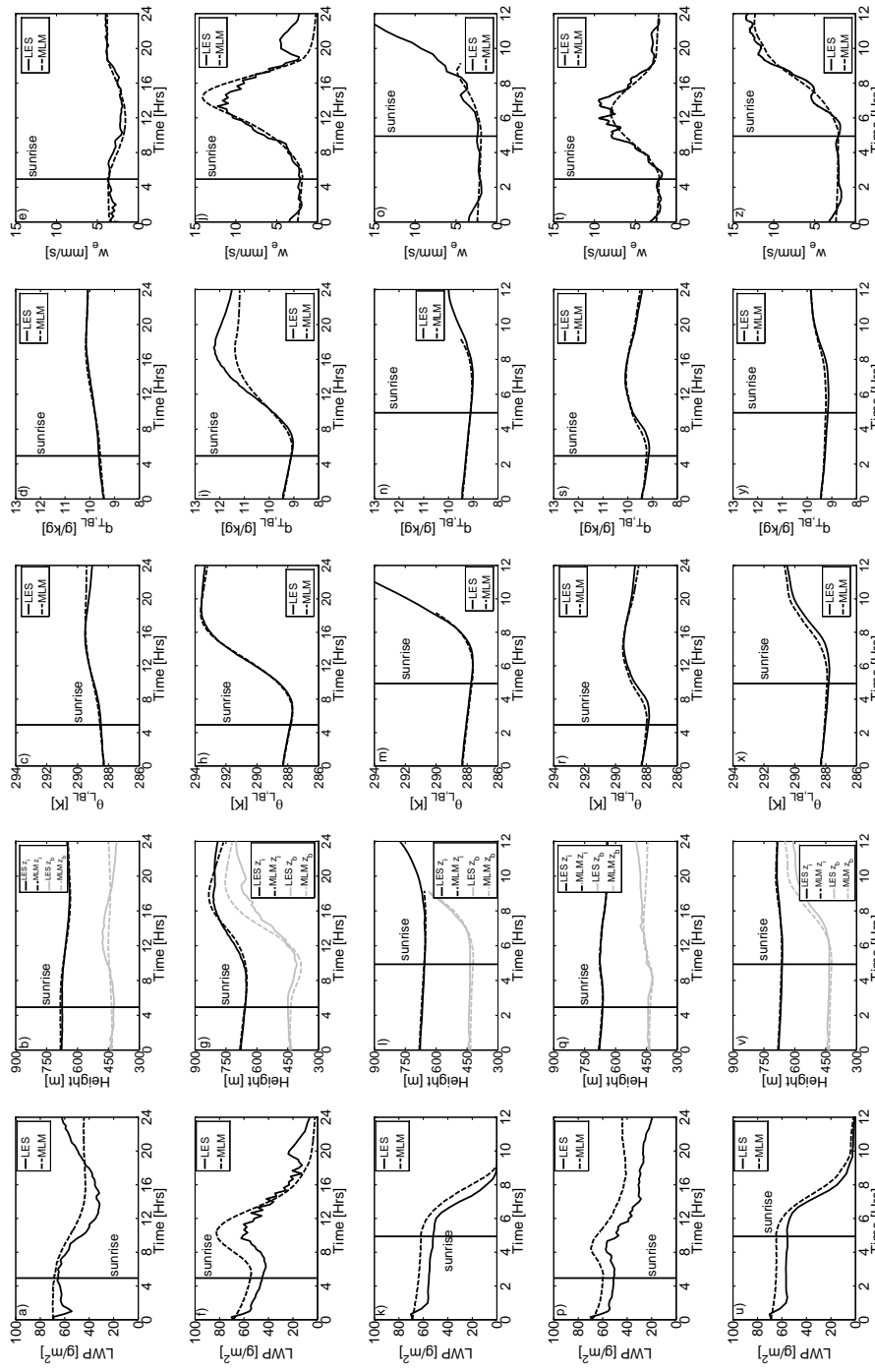
Figure 5.1. Comparison between LES (solid) and MLM (dashed) for the CGILS case of (**a, f, k, p, u**) LWP, (**b, g, l, q, v**) cloud base (grey) and inversion height (black), (**c, h, m, r, x**) liquid potential temperature of the boundary (θ_{IBL}), (**d, i, n, s, y**) total water mixing ratio (q_{TBL}), and (**e, j, o, t, z**) entrainment velocity (w_e) for ocean case (**a-e**), land case with Bowen ratio equal 0.1 (**f-j**), land case with Bowen ratio equal 1.0 (**k-o**), coupled case with horizontal advection representing the diurnally-varying sea breeze circulation and Bowen ratio equals to 0.1, and (**p-t**) coupled case with horizontal advection representing the diurnally-varying sea breeze circulation and Bowen ratio equals to 1.0 (**u-z**). Note that for the land case with Bowen ratio equal 1.0 (**k-o**) and coupled case with Bowen ratio equals to 1.0 (**u-z**), the plots are only from 0:00-12:00 LST as the cloud dissipates soon after sunrise and the MLM simulation ends.

5.1 Effects of surface flux, entrainment, subsidence, and radiation on cloud lifetime

We now apply Eq. 64 to the MLM output in order to understand how each physical process contributes to the cloud thickness tendency. For the all cases, radiation has a net cloud thickening effect during the night that decreases during the day due to solar absorption (Fig. 5.2). Subsidence thins the cloud by pushing the inversion downwards (Myers and Norris 2013). Entrainment flux, on the other hand, modulates cloud thickness and lifetime by raising the cloud top and thinning the cloud layer through the mixing of warm dry air aloft into the clouds. The magnitude of entrainment flux decreases during the day over the ocean due to the decrease in buoyancy flux caused by solar heating that offsets the longwave cooling within the cloud layer (Fig. 5.2 (a)). For the land surface cases, conversely, entrainment flux increases during the day driven by the increased surface flux (Fig. 5.2(b, c)). For the wet land case, despite the substantial moistening effect of surface latent heat flux, the combination of solar absorption and enhanced entrainment flux thin the cloud at a faster rate than the surface latent heat flux thickens the cloud; thus, the cloud layer eventually dissipates in the MLM (Fig. 5.2 (b)). For the dry land surface case, the combined effect of entrainment flux, solar absorption and sensible heat flux all act to rapidly dissipate the cloud during the day (Fig. 5.2(c)).

5.2 Effect of large-scale horizontal advection on cloud lifetime

In terms of temperature, large-scale advection of ocean air produces a strong cooling effect after sunrise that thickens the cloud layer for both dry and wet land surface conditions. In terms of moisture, large-scale advection acts to thin the cloud layer for the

wet surface case (Fig. 5.2 (d)). This is because the land STBL experiences increased latent heat flux from a wet surface at warmer temperature and thus has greater water vapor mixing ratio than air advected from the ocean. The combined effects of large-scale advection of heat and moisture nonetheless provide a net cloud thickening, as expected, that offsets the cloud thinning effects of larger entrainment flux, solar absorption, and the lower mixing ratio of the advected air (Fig. 5.2 (d)).

For the coupled dry surface case, the cloud thickening effect of large-scale advection is further enhanced by the attenuation of net surface radiation by the thicker cloud, thus reducing energy available for the surface flux warming. The advective tendencies more strongly support cloud thickening in the dry case compared to the wet case, because (i) the STBL over dry land is warmer, thus increasing land – ocean temperature gradients and (ii) the STBL over dry land is less moist and therefore advection only causes minimal drying compared to the STBL over wet land (Fig. 5.2 (e)).
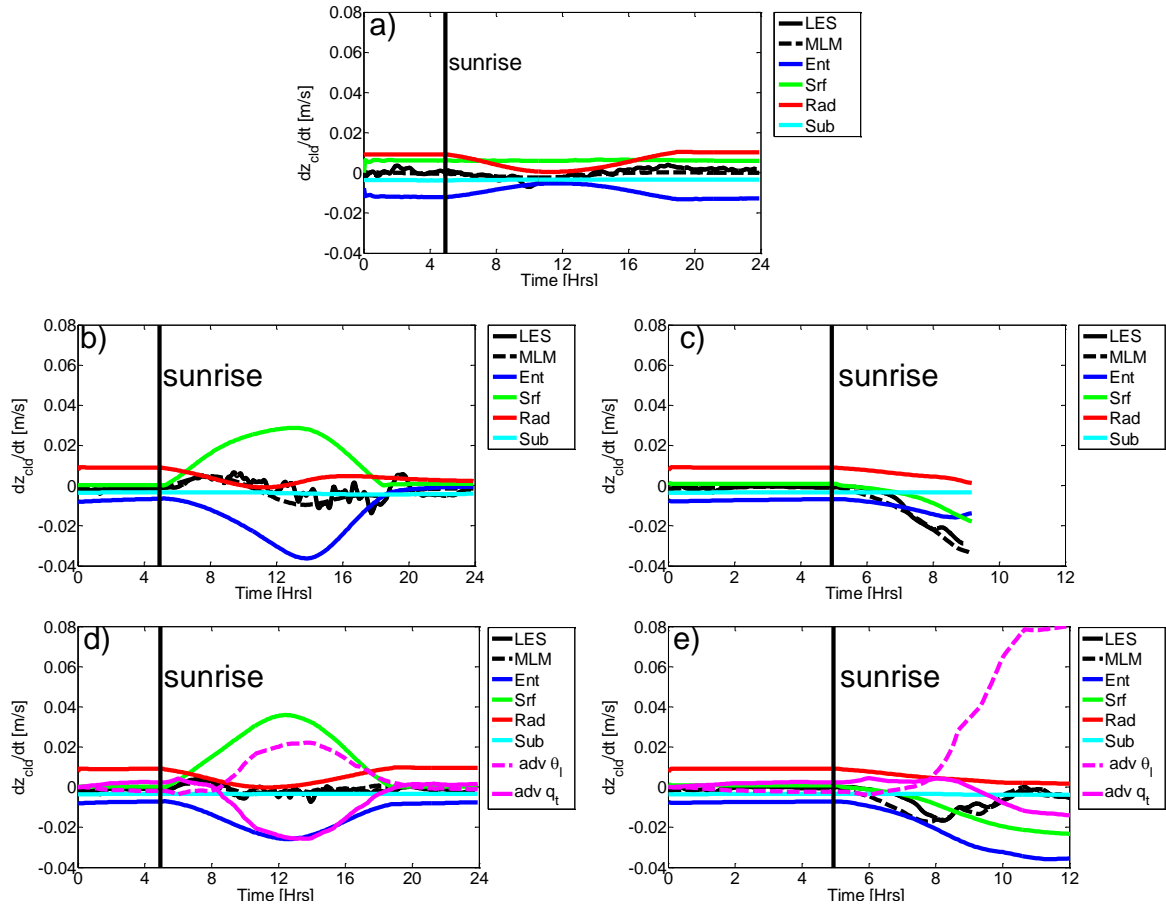
Figure 5.2. Breakdown of the different factors controlling cloud thickness (h) evolution in the MLM for **(a)** the ocean case, the land surface cases with Bowen ratio equal to **(b)** 0.1 and **(c)** 1.0 and the coupled case with Bowen ratio equal to **(d)** 0.1 and **(e)** 1.0. The entrainment flux across the inversion is denoted by the blue line, sensible heat flux (SHF) and latent heat flux (LHF) by the green line, radiation divergence by the red line, subsidence by the cyan line, large-scale horizontal advection of heat by the dashed magenta line, the large-scale horizontal advection of moisture by the solid magenta line, and total cloud thickness tendency by the black line for LES and the dashed black line for MLM.

5.3 Effects of initial conditions on cloud lifetime

In order to test how well the MLM performs under different initial conditions and the different physical factors affecting cloud lifetime, we simulate the five cases using DYCOMS initial profiles that consist of higher inversion height and a stronger temperature inversion than that of CGILS (Fig. 3.1). The LES and MLM results for the DYCOMS case are in good agreement (Fig. 5.3.). In the first two hours of the DYCOMS case, the MLM over-predicts entrainment velocity compared to the LES due to a

relatively weaker inversion and a stronger entrainment efficiency coefficient, and the stronger entrainment flux causes a rapid decrease in LWP in the MLM that is comparable to the decrease in LES due to the spinup effect. The major difference between the CGILS and DYCOMS cases is that the entrainment velocities are higher in the DYCOMS cases (Figs. 5.3. (e, j, o, t, z)) than in the CGILS cases (Fig. 5.1 (e, j, o, t, z)) due to the weaker inversion in DYCOMS initial profile (Fig. 3.1). Hence, the inversion height increases at a faster rate in the DYCOMS cases compared to the CGILS cases. Despite the higher magnitude of entrainment velocity in the DYCOMS cases, the contribution of entrainment flux to cloud thinning is similar to CGILS (Figs. 5.2, 5.4) due to the weaker temperature inversion in the DYCOMS case. Despite the difference in initial conditions, the cloud lifetime in both cases behaves similarly in response to the external forcings such as land surface properties and large-scale horizontal advection.
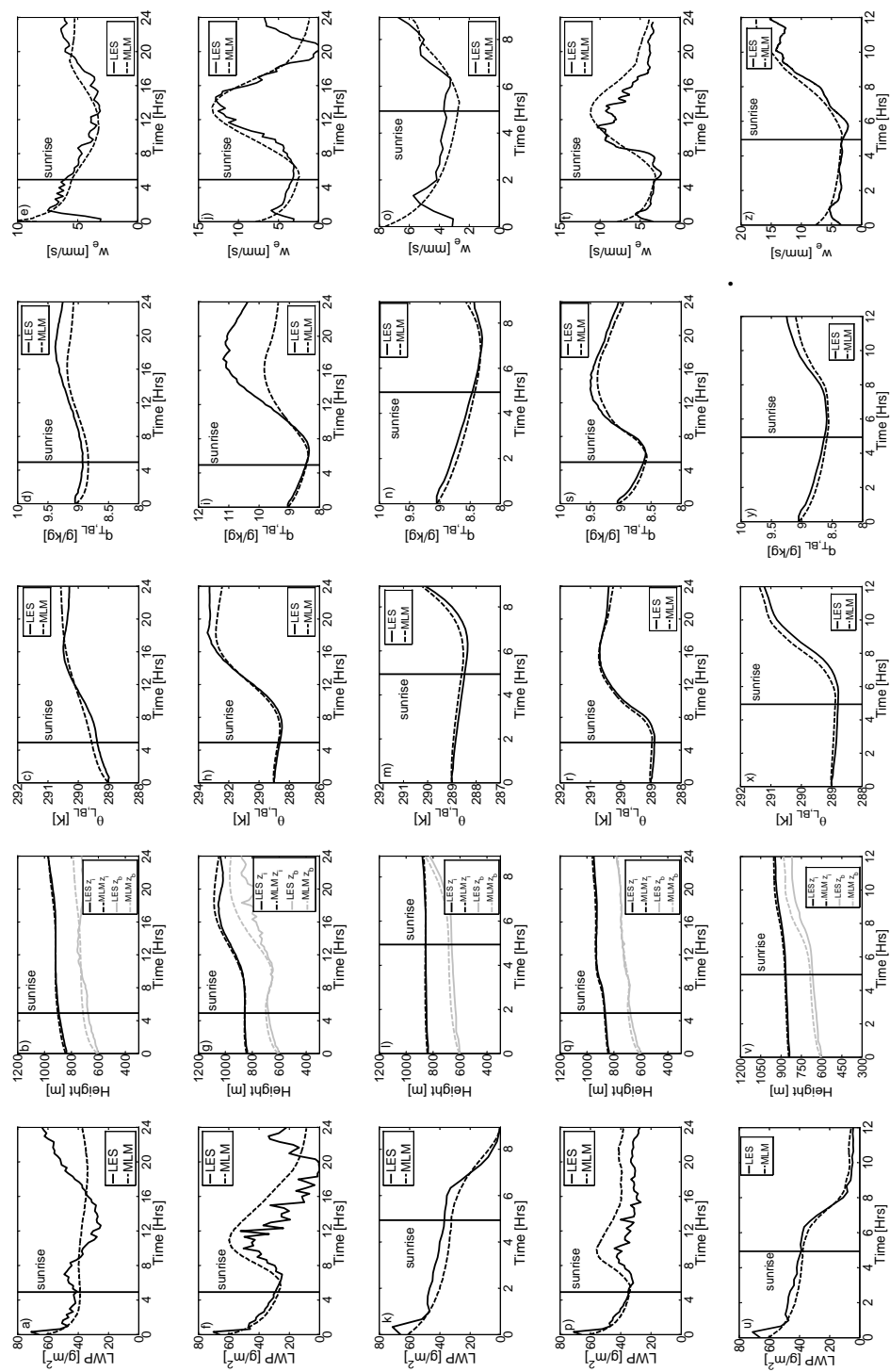
Figure 5.3. As Fig.5.1 , but for the DYCOMS initial conditions.
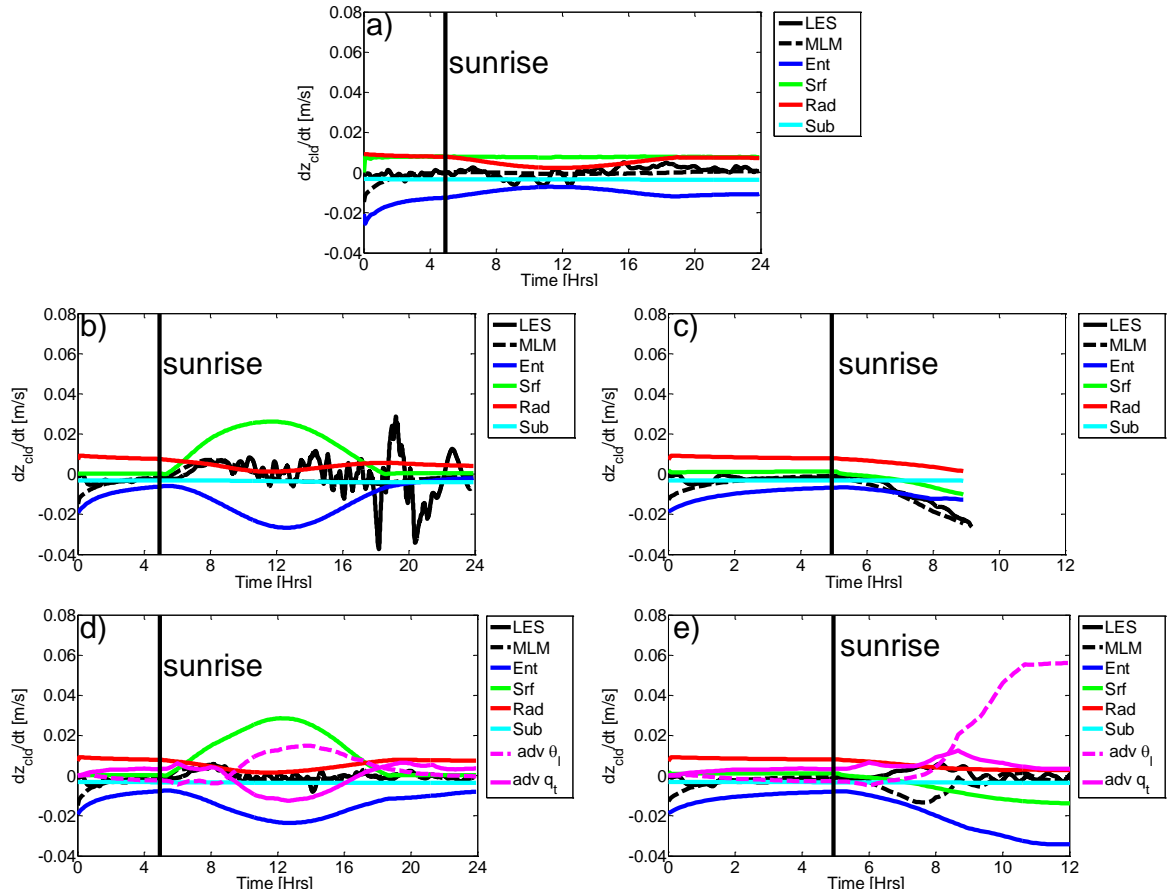
Figure 5.4. As Fig. 5.2, but for the DYCOMS initial conditions.

5.4 STBL feedback loops

The advantage of Eq. 64 applied to a MLM is that we can map the feedbacks between two variables and the interaction between different feedbacks. Although we provide only a qualitative description of the main feedback loops present in the STBL over the coast in this section, the feedback analysis could be expanded to include a quantitative analysis similar to that of Jones et al. (2014), in which the authors used LES and MLM to quantify the adjustment time scale arising from cloud thickness-turbulence-entrainment feedbacks for stratocumulus clouds over the ocean. A positive effect is one in which change (increase or decrease) in a certain variable results in the same type of change (increase or decrease) in a second variable and vice versa for a negative effect.

Effects can then be summed to form feedback loops. A positive feedback (reinforcing) loop occurs when a change in a certain variable ultimately comes back to cause further change in the same direction for that certain variable. A negative (balancing) loop, on the other hand, occurs when a change in a certain variable ultimately comes back to cause change in the opposite direction for that certain variable. An example of a positive loop is when the surface sensible heat flux warms the boundary layer and dissipates the cloud layer, thereby increasing the net surface radiation which feeds the surface flux. An example of a negative feedback loop is when the surface latent heat flux moistens the boundary layer, thereby thickening the cloud layer and reducing the net surface radiation feeding the surface latent heat flux. For the STBL particularly over land, the daytime cloud dissipating feedback loops tend to be more powerful, leading to rapid thinning of the initial cloud layer.

For all five cases, longwave radiative divergence cools the STBL, thereby thickening the cloud layer and increasing the longwave radiative divergence across the cloud layer, thus forming a reinforcing feedback loop (Fig. 5.5 (a)). Longwave radiative divergence additionally drives the turbulence in the STBL which feeds cloud top entrainment which in turn warms and dries the STBL, thereby reducing the cloud thickness and the longwave radiative divergence and thus forming a negative feedback loop (Fig. 5.5 (b)). Nocturnally, we observe that the stabilizing longwave-radiation-entrainment feedback loop dominates and that the LW cooling of the boundary layer saturates for LWPs of around 40 $\mathrm{gm^{-2}}$ (Figs. 5.1 (a), 5.3. (a)).

Over the ocean, solar radiative heating has two opposing effects on cloud thickness: (i) warming of the STBL that thins the cloud and therefore reduces solar

heating within the cloud layer (balancing feedback loop), and (ii) warming of the cloud layer that opposes longwave cooling and reduces buoyancy flux, which reduces cloud thinning due to weaker entrainment flux (positive feedback loop, Fig. 5.5 (a-b)). Over land, the STBL responds much faster to solar heating because the lower heat capacity of the land surface means most of the net surface radiative flux is reemitted by the land surface as turbulent fluxes of sensible and latent heat. Large-scale horizontal advection acts to dampen the effects of solar heating by thickening the cloud layer, thereby reducing the net radiation at the surface.

For the low Bowen ratio case we have two feedback loops: (i) a negative feedback loop that maintains the cloud layer and consists of surface latent heat flux moistening the STBL, thickening the cloud, and thereby attenuating the surface radiation feeding the surface flux and (ii) a positive feedback loop that causes the cloud to dissipate and consists of latent heat flux feeding the cloud-top entrainment flux, dissipating the cloud layer, and thereby increasing surface radiation feeding the surface flux (Fig. 5.5 (c-d)). We observe a positive feedback loop, in the high Bowen ratio case, in which increased sensible heat flux leads to increased entrainment with both factors then warming and drying the STBL. Both factors decrease the LWP, which in turn increases the net solar radiative flux at the surface thus driving an additional increase of surface flux (Fig. 5.5(d)).
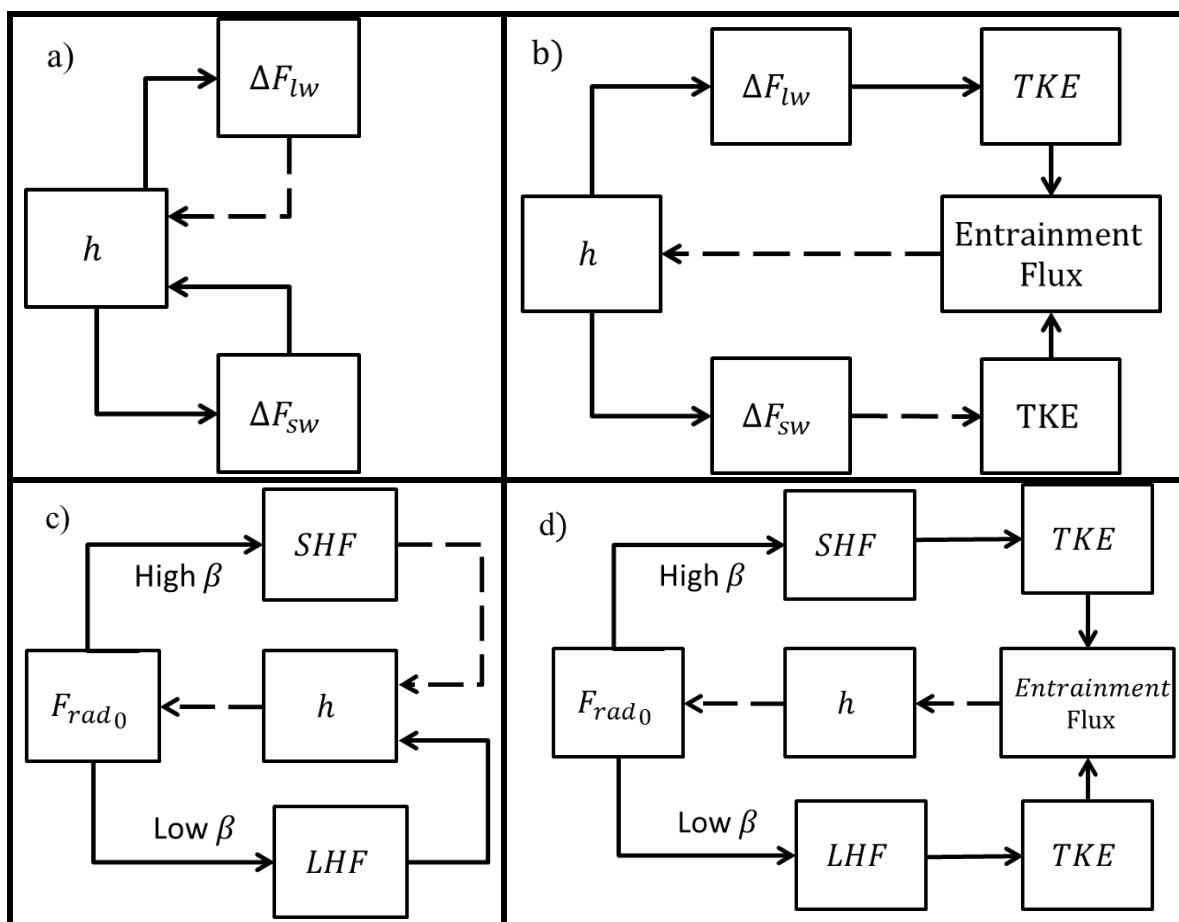
Figure 5.5. Feedback loops acting upon the cloud thickness (h) in the MLM. Solid lines denote positive effects, and dashed lines denote negative effects. Feedback loops are shown separately for (a) radiative divergence, (b) entrainment driven by radiative divergence, (c) surface flux, and (d) surface flux driven by radiative divergence.

5.5 Acknowledgement

Chapter 6.   Description of PBL Schemes

Numerical Weather Prediction models (NWP) and Global Climate models (GCMs) have a domains that range from 100s of kilometers to the entire globe. In order to simulate such large domains within current computational constraints, grid spacing is usually greater than 1 km in the horizontal direction and tens of meters in the vertical. Such coarse grid spacing is insufficient to resolve the boundary layer turbulent eddies. Hence, the boundary layer eddies must be parameterized. In order to develop the Planetary Boundary Layer parameterizations (PBL), we assume that the ensemble-averaged horizontal gradients of advected quantities are much less than their vertical gradients within the boundary layer such that the horizontal turbulent flux convergence can be neglected. Thus, the tendency of PBL turbulent mean variable $\bar{C}$, whereby $\bar{C}$ can represent $\bar{\theta}_l$ or $\bar{q}_t$, is expressed in terms of the convergence of its vertical turbulent flux($\overline{w'c'}$) as

$$\frac{\partial \bar{C}}{\partial t} = -\frac{\partial \overline{w'c'}}{\partial z}.$$

(**65**)

In order to solve Eq. 65 , we need to specify the vertical profile of $\overline{w'c'}$. One way is to employ the mixed-layer theory for STBL (Chapter 4) and assume a linear profile for $\overline{w'c'}$ and parameterize entrainment velocity, this method is also referred to as "zero-order closure". However, while MLM perform well in convective boundary layers, they perform poorly in stable boundary layers. Another method consists of formulating the turbulent flux in terms of mean variables, referred to as "first-order closure". A more complex scheme consists of equating the flux to second, third and higher order moments.

While such schemes account for more of the physics in the boundary layer, the higher moments must somehow be represented (Stull 1988). Hence, we must make some sort of "turbulence closure" assumption to specify the unknown moments in terms of know quantities.

GCM and NWP turbulence closure schemes are presently limited to first, 1.5, second and in some cases third order schemes (Holt and Raman, 1988). While second and third order schemes tend to represent more physics of the boundary layer, these schemes are more complex and computationally intensive as more equations and variables need to be computed. In this thesis we will focus on first-order and TKE (1.5-order) closure schemes which are commonly employed in NWP and GCM.

6.1 First-Order Closure

The turbulent transfer is modeled as molecular transport as

$$\overline{w'c'} = -K_C\left(\frac{\partial C}{\partial z}\right), \tag{66}$$

where K_C represent the eddy viscosity coefficient. Hence, the problem of first-order closure is effectively reduced to resolving K_c that is a property of the flow. The simplest method would be to specify a constant K_c, however such a model does not represent the boundary layer well. Rather by allowing K_c to depend height, and thermal stability, first order schemes are more capable of capturing more of the atmosphere's physics. Examples of K_c profile parameterizations include Brost and Wyngaard (1978) who parameterized K_c based on the surface layer and mixed layer scaling. Deardorff (1975) specified K_c to be proportional to the local turbulent energy while Yamamoto et al.

(1973) formulated K_c to be proportional to both vertical wind shear and vertical gradients of potential temperature.

In convective boundary layers the first-order turbulence closure scheme fails to models the buoyant thermals. For instance, the virtual potential temperature profiles are constant in the boundary layer of a well-mixed dry convective boundary layer. Consequently, first-order schemes that express flux as a function of the local gradient that is zero in a well-mixed boundary layer do not simulate any turbulence. Thus, in order to account for the rising parcels that originate at the surface and mix across the boundary layer, Holtslag and Boville (1993) proposed adding a correction term to account for convection as follows,

$$\overline{w'c'} = -K_C\left(\frac{\partial C}{\partial z} - \gamma_c\right),$$

(**67**)

where γ_c represents the nonlocal transport due to convection and is expressed as $\gamma_c = b\frac{\overline{(w'c')}_0}{w_{s0}z_{inv}}$, where $\overline{(w'c')}_0$ represents the flux generated at the surface and b represents the coefficient of proportionality. w_{s0} represents the mixed layer velocity scale evaluated at the surface and is expressed as $w_s = \left(u_*^3 + \phi_{h,m}kw_{*b}^3 z/z_{inv}\right)^{1/3}$ where u_* is the surface friction velocity, $\phi_{h,m}$ is the wind profile function evaluated at the top of the surface layer, and $w_{*b} = \left[g/\theta_{va}(\overline{(w'\theta_v')}_0 z_{inv})\right]^{1/3}$ is the convective velocity scale.

6.2 TKE Closure

TKE closure extends the first-order closure by solving the prognostic equations for TKE and energy dissipation or mixing length which are then utilized to determine K_c.

The scheme also commonly referred to as 1.5 order closure was proposed by -Mellor and Yamada in 1974. TKE ($q^2 = (\overline{u'^2} + \overline{v'^2} + \overline{w'^2})$) is expressed as

$$\frac{\partial q^2}{\partial t} = -\frac{\partial}{\partial z}\left(\overline{w'\left(u'^2 + v'^2 + w'^2 + \frac{2p'}{\rho}\right)}\right) - 2\left(\overline{u'w'}\frac{\partial u}{\partial z} + \overline{v'w'}\frac{\partial v}{\partial z}\right)$$
$$+ \frac{2g}{\theta_0}\overline{w'\theta'_v} - 2\varepsilon,$$

(68)

where $q^2 = (\overline{u'^2} + \overline{v'^2} + \overline{w'^2})$is twice the TKE and $\overline{w'\theta'_v}$ represents the virtual potential temperature veritcal flux and ε represents the dissipation rate of TKE (Nakanishi and Niino 2004). The first term on the right hand side of Eq. 68 represents turbulent and pressure transport, the second represent shear production, the third term represents buoyancy production the fourth dissipation of turbulent energy. The turbulent and pressure transport term can be modeled as

$$\left(\overline{w'(u'^2 + v'^2 + w'^2 + 2p'/\rho)}\right) = Lq\left(\frac{\partial q^2}{\partial z}\right),$$

(69)

where L is the mixing length scale(Nakanishi and Niino 2004). Buoyancy is expressed as

$\overline{w'\theta'_v} = Lq\frac{\partial\theta_v}{\partial z}$ and the dissipation rate is given by $\varepsilon = q^3/L$(Nakanishi and Niino 2004).

Chapter 7.   Evaluation of WRF SCM Simulations of STBL and Proposed Correction to Improve Turbulence and Entrainment Parameterizations

In this chapter, we evaluate SCM representation of the STBL in the Weather Research and Forecasting (WRF, Skamarock et *al*. 2008) model by comparing them against LES. Specifically, we evaluate the ability of the different PBL schemes to represent entrainment or mixing across the inversion, which plays an integral role in determining the cloud liquid water path (LWP), lifetime, and spatial extent and cloud microphysical properties. We analyze the Yonsei University (YSU) scheme that is a first-order scheme that models flux as a function of the eddy viscosity coefficient (Hong et al. 2006). The model includes a correction for counter gradient mixing and explicitly models the entrainment at the inversion. Second, we investigate the asymmetric convective model version 2 model (ACM2) that is also a first-order scheme, but uses a transilient matrix that defines mass flux to account for the convective eddies instead of using a counter-gradient correction term (Pleim 2007). Finally, we examine the Mellor–Yamada–Nakanishi–Niino model (MYNN) that is a (TKE) closure scheme (Nakanishi and Niino 2004). MYNN solves the TKE prognostic equation, which provides a better measure of the intensity and effectiveness of turbulence in the STBL, to determine the eddy diffusivity. Both the YSU and the ACM2 are less complex, more computationally economical models while the MYNN scheme takes into account more of the physics of the boundary layer at a higher computational cost. Furthermore, in order to account for the effects of the microphysics parameterizations, we run each scheme with four different microphysics schemes offered in WRF. We do not expect that the microphysics schemes

have a strong impact on the simulations, as the clouds are relatively thin and therefore do not drizzle significantly.

7.1 Model setup

For this analysis, we used WRF v3.7.1 in single column mode to evaluate three PBL and four microphysics schemes (refer to Tables 7.1 and 7.2 for an overview of the schemes). The vertical domain of the SCM consists of 75 levels up to an altitude of 10,000 m and the simulation time step is 20 s. The SCM employs New Goddard scheme for LW and SW radiation, and Monin-Obukhov similarity theory for the surface parameterization (Chou and Suarez 1999, 2001). We do not examine the radiative, surface, and land parameterizations and instead focus on the fluxes into or out of the boundary layer at the land surface and across the inversion. The DYCOMS rf01 initial profiles are utilized (Zhu et al. 2005). Following Zhu et al. (2005), we set the surface sensible heat flux (SHF) to be 15 $W\,m^{-2}$ and the latent heat flux (LHF) to be 115 $W\,m^{-2}$. Unlike in the DYCOMS SCM intercomparison study that evaluated a nocturnal six hour simulation, we run a 24-hour simulation in order to study how well the SCM are capable of simulating the STBL over the diurnal cycle. All simulations are initialized at midnight.

The UCLA-LES model is setup as in the DYCOMS LES intercomparison study (Stevens et al. 2005). The only difference is that we couple the LES to a one-dimensional radiative model with Monte Carlo sampling of the spectral integration rather than the parameterized radiative scheme employed in the DYCOMS LES intercomparison (Stevens et al. 2005; Pincus and Stevens, 2009). We find that the one-dimensional

radiative model produce fluxes that are closer to the New Goddard scheme employed in the WRF SCM.

Table 7.1. List of PBL schemes used in this study

PBL scheme	Parameterization type	Reference
Yonsei University (YSU)	First-order closure scheme. Turbulence is parameterized using the eddy-diffusivity approach and a gradient adjustment term is added to account for large-scale eddies. Entrainment is explicitly modelled.	Hong et al. (2006)
Asymmetric convective Model version 2 (ACM2)	First-order nonlocal closure scheme. Turbulence is parameterized as a combination of local eddy diffusion and a non-local transilient matrix that defines mass flux between any pair of model layers.	Pleim (2007)
Mellor–Yamada–Nakanishi–Niino (MYNN)	TKE closure scheme	Nakanishi and Nino (2004)

7.2 SCM Inversion Height determination

In WRF v3.7.1, the YSU and ACM2 schemes as well as the MYNN scheme, for convective boundary layers, determine the inversion height (planetary boundary layer height) based on,

$$z_{inv} = Rib_{cr} \frac{\theta_{va}|u(z_{inv})|^2}{g[\theta_v(z_{inv}) - \theta_s]},$$

(70)

where θ_v is the virtual potential temperature, Rib_{cr} is the critical bulk Richardson number, $u(z_{inv})$ and $\theta_v(z_{inv})$ are the horizontal wind speed and virtual potential temperature at the inversion height, respectively, θ_{va} is the virtual potential temperature at the lowest model level, and θ_s is the virtual potential temperature at the surface (Hong et al. 2006; Pleim 2007).

However, θ_v is not conserved within the cloud layer (θ_v increases with height above the cloud base height). Hence, Eq. 70 underestimates inversion height compared to SCM cloud-top height and inversion height in the LES (Fig. 7.1). Cloud top height is defined as the highest grid level with liquid water content in the SCM. LES inversion

height is defined at the maximum gradient of liquid potential temperature. We substitute θ_v in Eq. 70 with liquid virtual potential temperature $\theta_{vl} = \theta_l(1 + 0.608q_t)$ that is conserved within the STBL (Grenier and Bretherton 2001). We note that as the PBL schemes do not explicitly use inversion height in modelling the physics of the STBL, we do not observe a significant change in the results between the original and modified definition of inversion height.
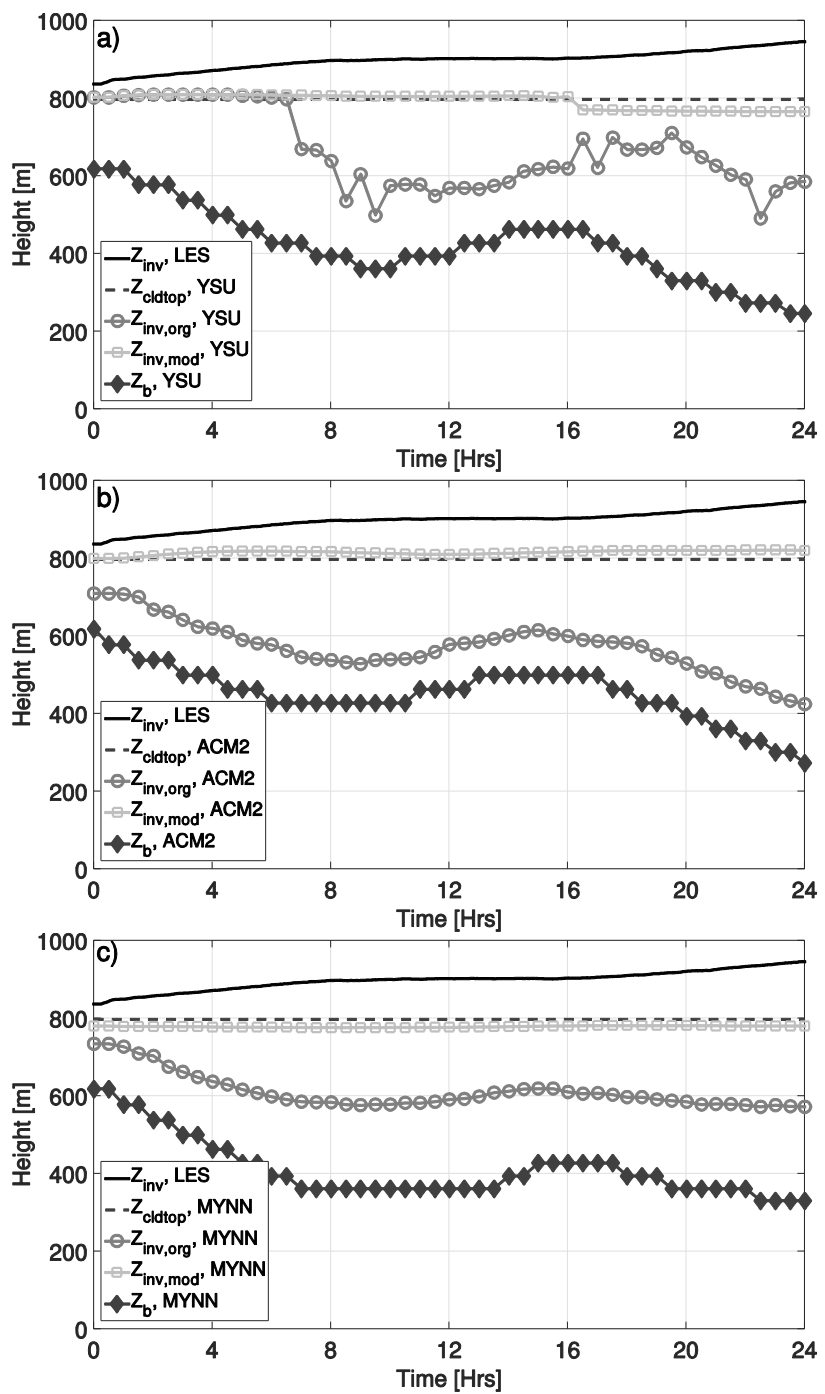
Figure 7.1. Original inversion heights based on Eq. 70 plotted with grey lines and circle markers, cloud-top heights plotted with grey dashed lines, and modified inversion heights plotted with grey lines and square markers for **(a)** YSU scheme, **(b)** ACM2 scheme, and **(c)** MYNN scheme. LES derived inversion height is plotted with the solid black line.

7.3 PBL formulation

7.3.1 YSU

Following Hong et al. (2006), the YSU scheme parameterizes the turbulent flux as

$$(\overline{w'c'})_{YSU} = -K_C \left(\frac{\partial C}{\partial z} - \gamma_c \right) - \overline{w'c'}_{z_{inv}} \left(\frac{z}{z_{inv}} \right)^3, \tag{71}$$

where K_c is the eddy diffusivity coefficient and is expressed as

$$K_C = k w_s z (1 - z/z_{inv})^2, \tag{72}$$

where k is the von Karman constant. The mixed layer velocity scale is expressed as

$w_s = \left(u_*^3 + \phi_{h,m} k w_{*b}^3 z/z_{inv} \right)^{1/3}$ where u_* is the surface friction velocity, $\phi_{h,m}$ is the wind

profile function evaluated at the top of the surface layer, and

$w_{*b} = \left[g/\theta_{va}((\overline{w'\theta_v'})_0 z_{inv}) \right]^{1/3}$ is the convective velocity scale. γ_c incorporates the

contributions of large-scale eddies to total flux and is computed as $\gamma_c = b \frac{(\overline{w'c'})_0}{w_{s0} z_{inv}}$, where

$(\overline{w'c'})_0$ represents the flux generated at the surface and b represents the coefficient of

proportionality. $(\overline{w'c'})_{z_{inv}} = w_e \Delta C_i$ represents the flux across the inversion. Finally,

entrainment w_e is parameterized as

$$w_e = A \frac{\theta_{v0}}{g \Delta \theta_{vi} z_{inv}} w_T^3, \tag{73}$$

where A is a constant taken to be -0.15, θ_{v0} is the reference virtual, $\Delta \theta_{vi}$ represent the

inversion jump. w_T^3 is a velocity scale based on the surface turbulence,

$$w_T^3 = w_*^3 + 5u_*^3, \tag{74}$$

where $w_* = [g/\theta_{va}((\overline{w'\theta'})_0 z_{inv})]^{1/3}$ is the mixed-layer velocity scale for dry air (when

$\theta = \theta_v$).

7.3.2 ACM2

The ACM2 uses a staggered grid where scalar quantities and horizontal momentum components are represented at the grid layer centers designated by i and the vertical fluxes, vertical velocities and eddy diffusivities are located at the layer interface $i + 1/2$. Hence, ACM2 computes flux at the interface as follows,

$$\left([\overline{w'c'}]_{i+1/2}\right)_{ACM2} = -(1 - f_{conv})K_{C,z_{i+1/2}} \frac{\partial C_i}{\partial z} + f_{conv} \frac{K_{C,z=3/2}}{\Delta z_{z=3/2}}(C_1 - C_i),$$ (75)

where f_{conv} is a weighting factor that splits mixing between local and non-local components and is expressed as

$$f_{conv} = \frac{K_c \gamma_h}{K_c \gamma_h - K_c \frac{\partial \theta}{\partial z}},$$ (76)

where γ_h is the gradient adjustment term for the nonlocal transport of sensible heat expressed as $\gamma_c = a w_* \left(\overline{w'\theta'}\right)_0 / w_m^2 z_{inv}$, w_* is the convective velocity scale and $w_m = u_*/\phi_m$ (Pleim 2007). K_C is as for the YSU scheme in Eq. 72, but the mixed layer velocity scale is expressed as $w_s = u_*/\phi_{h,m}$. ACM2 was designed such that the second term on the right hand side of Eq. 75 represents mass fluxes due to upward transport in convectively buoyant plumes. The first term on the right hand side of Eq. 75 represents the local eddy diffusion.

7.3.3 MYNN

The MYNN scheme determines the eddy diffusion coefficient as a function of turbulent kinetic energy (TKE, q), stability correction functions for momentum, heat, and water vapor (S_M, S_H, S_q, respectively), and the master length scale (L) as follows

$$(\overline{w'c'})_{MYNN} = qLS_{M,H}\frac{\partial C}{\partial z}.$$

(77)

The master length scale is a function of the Obukhov length, TKE, and buoyancy flux (Nakanishi and Niino, 2004). Refer to section 6.2 for an overview of TKE closure schemes.

7.4 PBL evaluation

The diurnal cycle of the WRF SCM simulated vertically integrated LWP is shown in Fig. 7.2(a), along with the LES result. All three PBL schemes yield a LWP that is more than twice that in LES. The LWP increases rapidly for all three PBL schemes at initialization at midnight reaching a maximum LWP shortly after sunrise after which they decrease during the day due to solar heating.
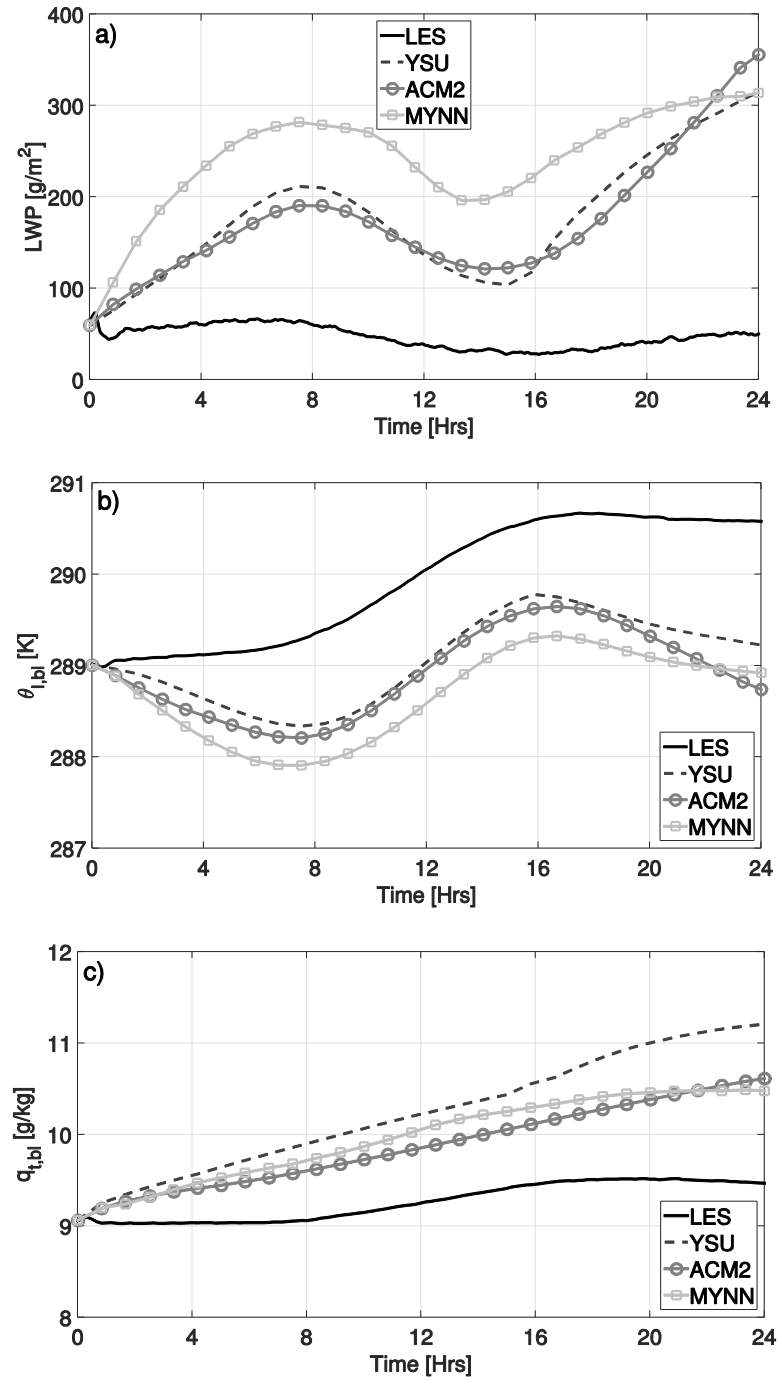
Figure 7.2. (a) Domain averaged vertically integrated LWP. **(b)** Boundary layer averaged liquid potential temperature and, **(c)** total water mixing ratio.

Figures 7.2(b, c) depict the boundary layer averaged liquid potential temperature

(θ_l) and the total water mixing ratio (q_t), respectively. Both θ_l and q_t are conserved in

adiabatic motions of moist air parcels in a well-mixed STBL (i.e. both variables are constant with height in the STBL); hence, we use the boundary layer averaged quantities as a proxy for the STBL heat and moisture content. All three schemes simulate lower θ_l and higher q_t values within the boundary layer. Hence, the SCM model a cooler, moisture STBL. STBL moisture content simulated by SCMs increases throughout the 24-hour simulation period. Since surface flux is kept constant for both the LES and the SCMs, the moisture and heat bias of the SCMs compared to LES is indicative of deficiencies in either the microphysics or the PBL parameterizations.

We use cloud thickness tendency as a proxy for the liquid water path tendency as they are analogues (Section 4.4). Since the inversion height diurnal cycle is much smaller than that of the cloud base height (Fig. 7.1), we will limit our analysis to the cloud base height tendency (Eqs. 57 61).

Figure 7.3. (a) Total cloud base height tendency, **(b)** θ_l vertical turbulent flux contribution to cloud base height tendency, **(c)** q_t vertical turbulent flux contribution to cloud base height tendency, and **(d)** radiative flux contribution to cloud base height tendency.

All three schemes produce a negative cloud base height tendency, ranging from -5 to -15mms^{-1}) nocturnally that is indicative of a thickening cloud layer (Fig. 7.3 (a)). The LES, on the other hand, simulate a cloud base height tendency that is close 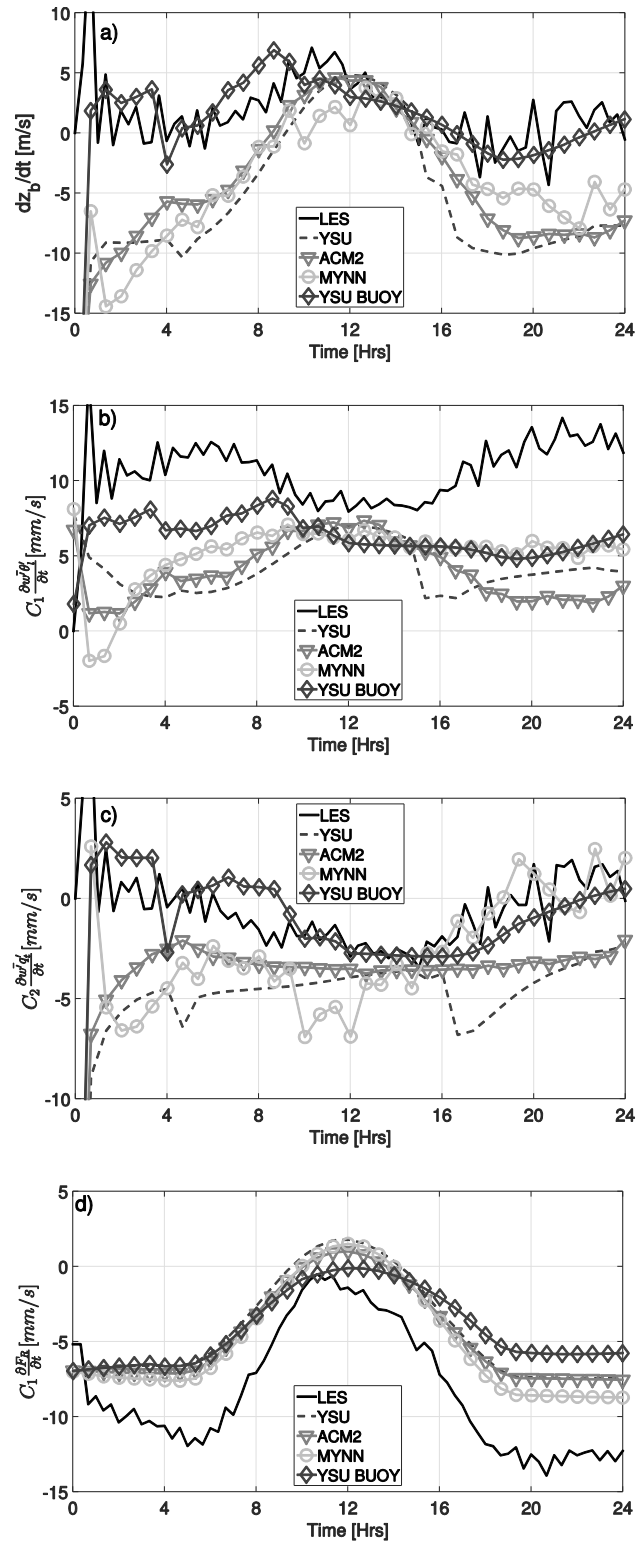to zero nocturnally and a positive tendency during the day due to solar loading. During the day, $\partial z_b/\partial t$ is positive as the cloud thins due to solar warming. Next, we split up the cloud base height tendency contributions due to liquid potential temperature vertical flux ($C_1\overline{w'\theta_l'}$) and total water mixing ratio vertical flux ($C_2\overline{w'q_t'}$). We note that within the STBL, surface sensible heat flux and cloud top entrainment flux both act to warm the STBL, while surface latent heat flux act to moisten the STBL and entrainment flux acts to dry the STBL. $C_1\overline{w'\theta_l'}$ is underestimated for all three schemes compared to the LES results, particularly for the MYNN scheme for the first two hours (Fig. 7.3). Noting that the surface flux is held constant for all schemes and assuming the STBL is well-mixed, we conclude that the entrainment flux warming is underestimated in the three PBL schemes resulting in a cooler STBL in which the cloud deck is thicker. Similarly, $C_2\overline{w'q_t'}$ is negative for the three PBL schemes, which indicates that there is little entrainment flux drying the STBL and acting to reduce the surface latent heat flux moistening of the STBL thereby decreasing the cloud base height (Fig. 7.3). Thus, for all three schemes we observe a systematic under-prediction of cloud-top entrainment flux. Due to the different radiation schemes employed by LES and the WRF SCMs, the LES radiative scheme simulates a strong radiative flux divergence thereby resulting in stronger longwave radiative cooling nocturnally compared to the SCM (Fig. 7.3(d)).

7.5 Microphysics scheme evaluation

In order to determine the effects of microphysics parameterization, we simulate compare four different microphysics parameterization for each of the PBL schemes (Table 2). For both the YSU and the ACM2 schemes, there is little dependence of LWP on the microphysics scheme for the first 18 hours. After sunset, the clouds begin to precipitate leading to a spread in LWP (Fig 7.4, 7.5). For the MYNN scheme, we observe a large spread in LWP for the different microphysics; whereby the WSM5 scheme produces the least LWP (Fig. 7.4 (c)). The spread is mainly due to precipitation, whereby the different autoconversion schemes within the microphysics schemes form raindrops due to collision of cloud droplets at different efficiencies. The MYNN in particular experiences a strong growth in LWP initially, resulting in thicker clouds that drizzle more (Fig. 7.4). Note that the thick drizzling clouds simulated by the different PBL and microphysics schemes are not consistent with DYCOMS LES results or the campaign measurements.

Table 7.2. List of microphysics schemes used for the microphysics senesitivty study

Microphysics scheme	Hydrometers	Reference
Kessler	water vapor, cloud water, rain	Kessler (1969)
Lin	water vapor, cloud water, ice, rain, snow and graupel	Lin et al. (1983)
Thompson	water vapor, cloud water, rain, ice, snow and graupel	Thompson et al. (2008)
WSM5	water vapor, cloud water, rain, ice, and snow	Hong et al. (2004)

All microphysics schemes simulated the sharp increase in LWP at the start of the simulation; hence, the cold, moist bias of the PBL schemes is not a result of deficiencies in the parameterization of the microphysics schemes. Thus, we hypothesize that the over-

estimation of cloud liquid water content is the result of incorrect PBL parameterization of entrainment flux.
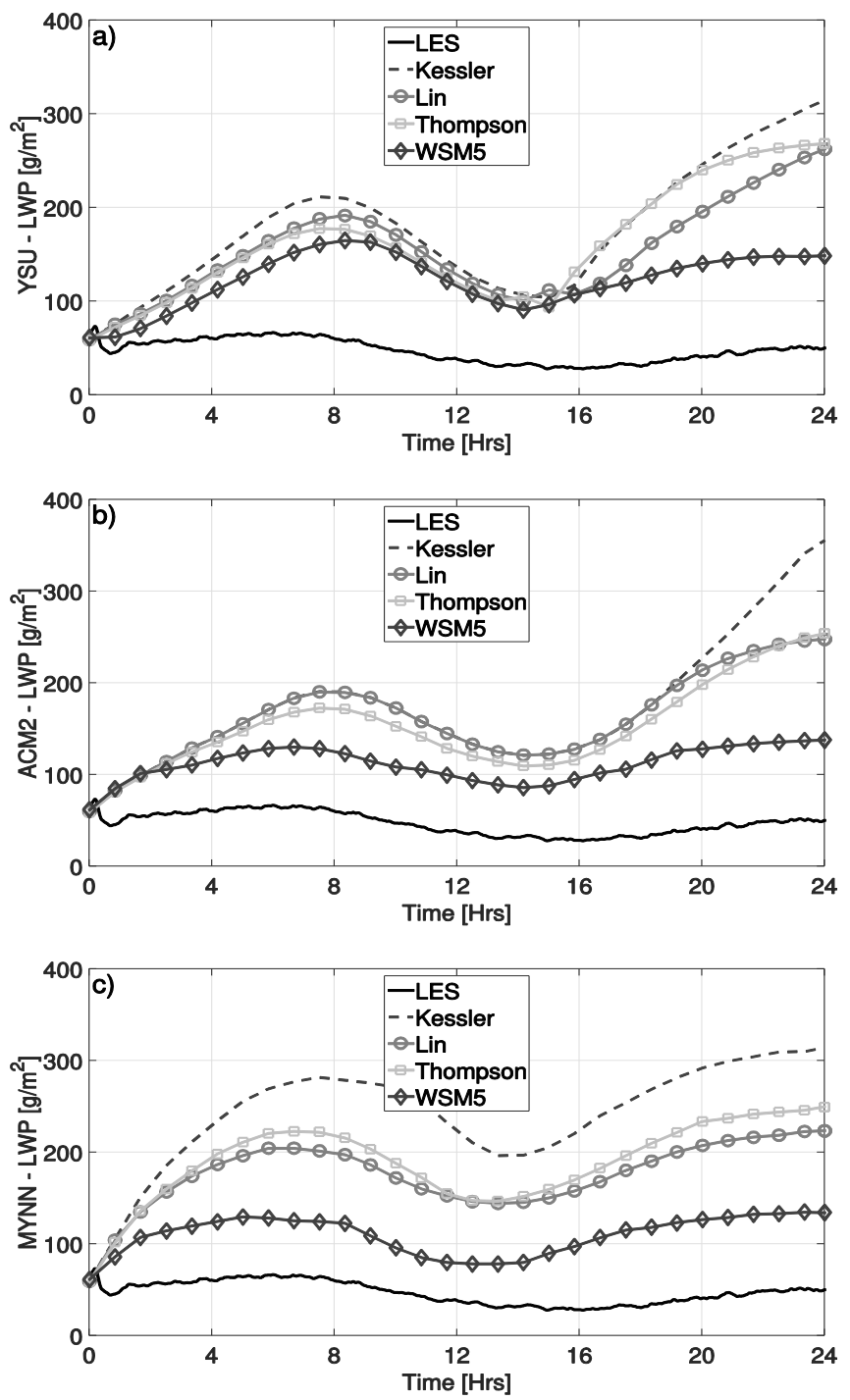

Figure 7.4. Domain averaged vertically integrated LWP for **(a)** YSU scheme, **(b)** ACM2 scheme, and **(c)** MYNN scheme and different microphysics schemes (Table 7.2).
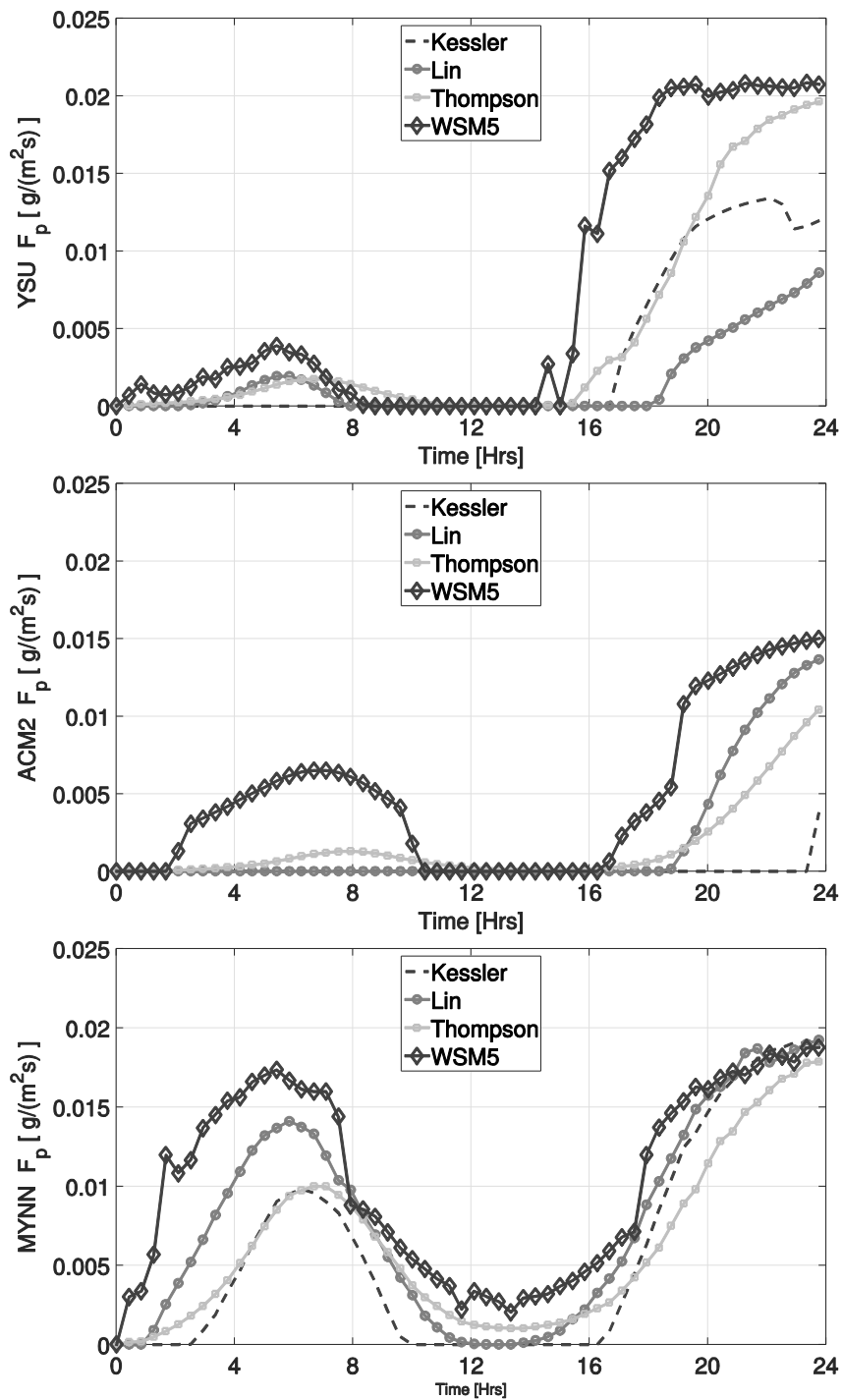
Figure 7.5. Precipitation flux at the surface for **(a)** YSU scheme, **(b)** ACM2 scheme, and **(c)** MYNN scheme and different microphysics schemes.

7.6 Proposed PBL correction and validation against LES

The eddy diffusivity coefficient proposed by Hong et al. (2006) in the YSU scheme does not take into account the contribution of cloud-top longwave radiative cooling to turbulence generated in the STBL. These thermals originate at the cloud –top and sink downwards through the STBL, as shown in plots of the third moment of vertical wind simulated by LES for the DYCOMS case (Fig. 7.6 (c)). Hence, we implement a correction to the YSU PBL scheme (YSU-BUOY). Following Lock et al. (2000) we define the eddy diffusivity coefficient as

$$K_c = kw_s z(1 - z/z_{inv})^2 + kw_{cld}\frac{z^2}{z_{inv}}(1 - z/z_{inv})^{0.5},$$

(78)

where w_{cld} is the cloud velocity scale and is formulated as:

$$w_{cld} = \frac{g}{\theta_{v0}}\int_{z_b}^{z_i}\overline{w'\theta_v'}\,dz,$$

(79)

where θ_{v0} is the reference virtual the virtual potential vertical flux is expressed as

$$\overline{w'\theta_v'}(z) = C_1\overline{w'\theta_l'}(z) + C_2\overline{w'q_T'}(z) \qquad z_b < z < z_{i,}$$

(80)

where $C_1 = \dfrac{1 + \frac{\overline{q_s}}{\epsilon} - \overline{q_T} + \frac{\overline{\theta}}{\epsilon}\left(\frac{dq_s}{dT}\right)}{1 + \frac{L_v}{c_p}\left(\frac{dq_s}{dT}\right)} \approx 0.5$ and $C_2 = \dfrac{L_v}{c_p}\left(\dfrac{1 + \frac{\overline{q_s}}{\epsilon} - \overline{q_T} + \frac{\overline{\theta}}{\epsilon}\left(\frac{dq_s}{dT}\right)}{1 + \frac{L_v}{c_p}\left(\frac{dq_s}{dT}\right)}\right) - \overline{\theta} \approx 970$ K within the

cloud layer (refer to Stevens 2002 for a more detailed derivation of the constants). Instead of formulating the cloud velocity scale as function of radiative divergence as in Lock et al. (2000), we have chosen the buoyancy flux within the cloud layer as the cloud-top longwave emission becomes insensitive to LWP changes for thick clouds (Kazil et al., 2015). Thus, by formulating w_{cld} as function of the buoyancy flux within the cloud layer,

YSU-BUOY accounts for additional turbulence generated by latent heat releases in updrafts within in the cloud layer.
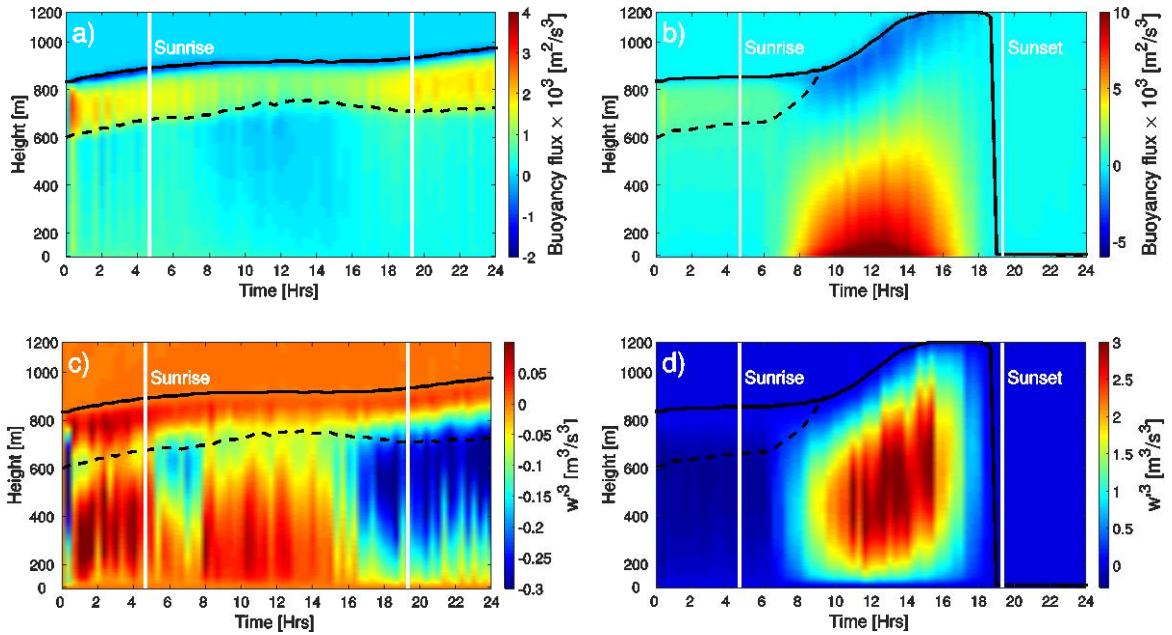
Figure 7.6. Horizontally averaged temporal evolutions from LES for the DYCOMS case of vertical profiles of **(a, b)** buoyancy flux and **(c, d)** third moment of vertical velocity ($\overline{w'^3}$). Results are shown for the ocean case **(a, c)** and land case with Bowen ratio equal 1.0 **(b-d)**. While the LES domain extends up to 1.6 km, only the lowest km is shown to focus on the boundary layer dynamics.

Similarly, the entrainment velocity parameterization does not account for the longwave cooling generated turbulence resulting in the underestimation of entrainment flux observed in Fig. 7.3. Hence similar to the entrainment parameterization outlined in Section 4.3, we define a new velocity scale for the entrainment parameterization as

$$w_T^{*3} = 1.25 \frac{g z_i}{\theta_{v0}} \overline{w'\theta'_v}_s + 2.5 \frac{g}{\theta_{v0}} \int_{z_b}^{z_i} \overline{w'\theta'_v} \, dz.$$

(81)

The convective velocity scale in Eq. 81 follows Lock et al. (1999 except instead of using the net radiative flux we use the integral of the in-cloud buoyancy flux. We do not modify the counter-gradient term (γ_c) as we find that the upward thermals generated by surface flux are much stronger than the downward thermals of cool air generated by

longwave cooling. The buoyancy flux generated due longwave radiative cooling rarely exceeds $4\,\mathrm{m^2 s^{-3}}$ for the DYCOMS case. However, if we run the same profile over the land surface we observe very strong thermals generated by the surface flux with buoyancy flux regularly exceeding $10\,\mathrm{m^2 s^{-3}}$ (Fig. 7.6 (a, b)). Thus, for the ocean cases, the thermals are not as strong as for the land case and we do not need to add a counter gradient term to account for them. For the remainder of the study we refer to the corrected YSU scheme as YSU-BUOY.

The corrected YSU scheme (YSU-BUOY) simulates a drier warmer STBL that better matches the LES compared to the original YSU parameterization (Fig. 7.7). This is a result of increased entrainment flux drying and warming the STBL (Fig. 7.3). As expected, YSU-BUOY then simulates LWP closer to the LES and DYCOMS measurements (Fig. 7.7). We do not observe any dependence on the microphysics schemes as the reduced LWP eliminates precipitation in the YSU-BUOY scheme (not shown). While YSU-BUOY, slightly underestimates LWP the diurnal cycle of LWP is accurately captured.
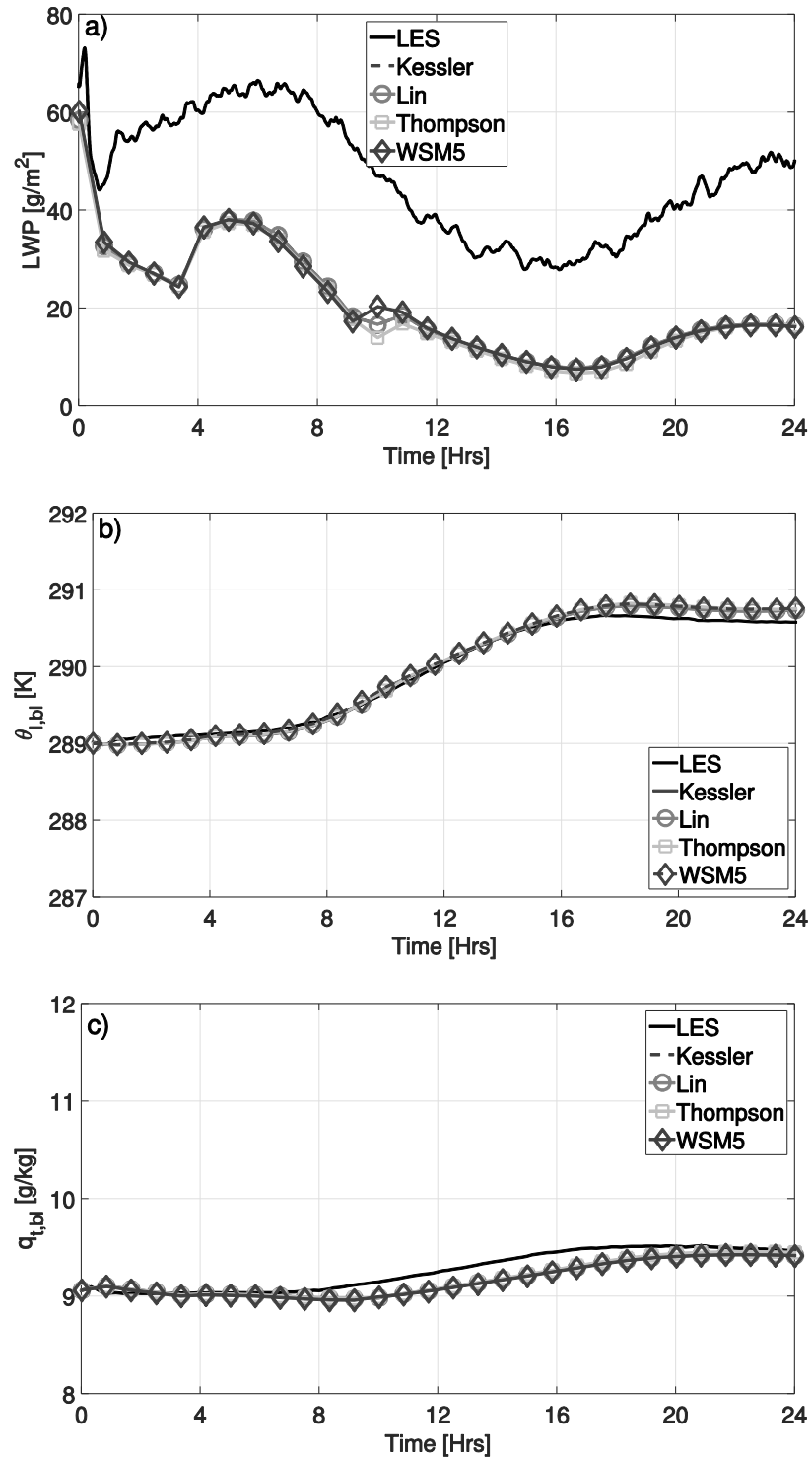
Figure 7.7. (a) Domain averaged vertically integrated LWP. **(b)** Boundary layer averaged liquid potential temperature and **(c)** total water ming ratio.

Next, we test the effect of resolution on the YSU-BUOY scheme to find that it plays an important role as expected (Fig. 7.8). We ran YSU-BUOY with 5 meter resolution in the boundary layer and find that the LWP matches that of the LES more accurately than the original resolution. The improvement in representation of STBL in the higher resolution could be due to numerics, for instance Lenderink and Holtslag (2004) found that convective schemes tend to produce liquid water through numeric detrainment process at the cloud top. Coarse resolution can lead to step jumps in LWP as grid cell becomes clear, this is particularly evident if the grid cell is near the cloud top with the highest liquid water content.
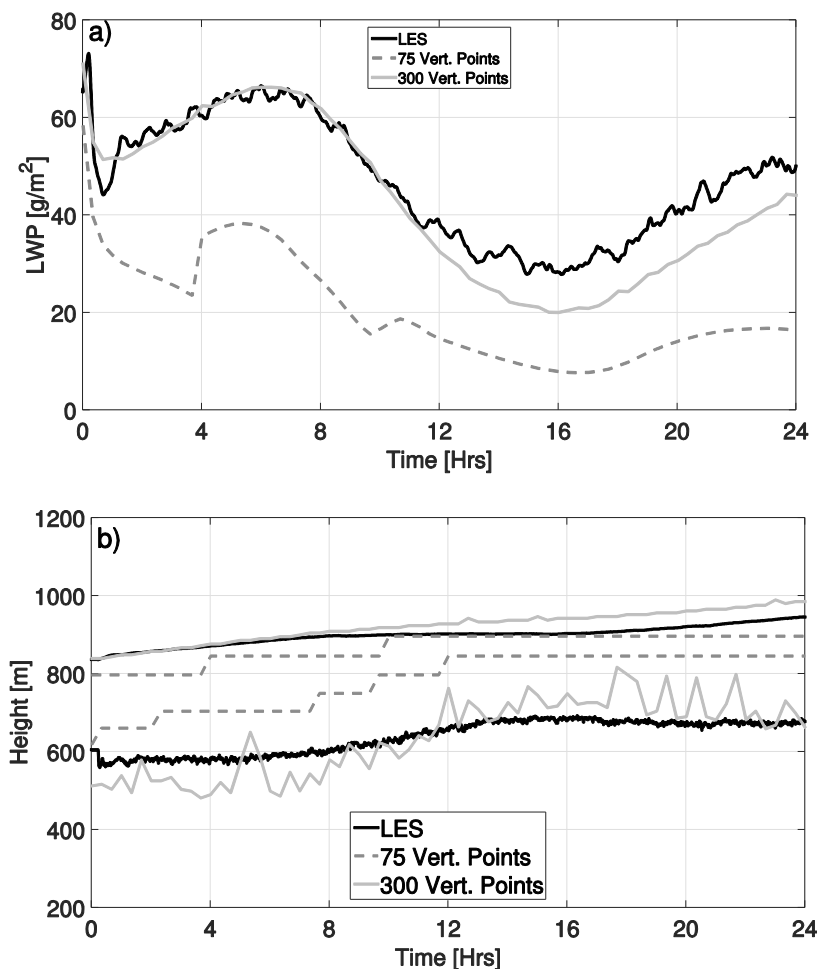
Figure 7.8 (a) Domain averaged vertically integrated LWP and **(b)** Inversion height and cloud base height for LES (solid black line), YSU-BUOY with 75 vertical points (grey dashed line), and YSU-BUOY with 300 vertical points (grey dashed line).

Furthermore, similar to the MLM validation in Chapter 5, we test YSU-BUOY for STBL occurring over coastal lands with DYCOMS initial profiles. We find that for relatively wet land surface ($\beta = 0.1$) YSU-BUOY is able to simulate LWP similar to LES for the first 16 hours of the simulation capturing the increase in inversion height driven by surface flux during the day (Fig. 7.9 (a-d)). However, YSU-BUOY underestimates entrainment flux after 16 hours as surface flux decreases and the clouds are not thick enough to produce sufficient longwave induced turbulence in the boundary

layer. Furthermore, we have a relatively thick boundary layer in which the buoyancy flux becomes negative indicating mild decoupling. Hence, due to the lower simulated turbulence, YSU-BUOY underestimates entrainment leading to cooler moisture STBL with higher LWP compared to the LES. Finally, we simulate the STBL over a relatively dry land surface ($\beta = 1.0$). YSU-BUOY is able to accurately simulate the cloud dissipation driven by surface sensible heat flux warming. Moreover, YSU-BUOY is able to capture the sharp increase in inversion height (about an increase of 250m) in the dry convective boundary layer regime during the day and the subsequent collapse at night (Fig. 7.9 (e-h)). In order to test how well YSU-BUOY performs under different initial condition we compare it to LES for the CGILS s12 case (Zhang et al., 2012; Blossey et al., 2013). YSU-BUOY matches the results of the LES relatively well simulating shortwave daytime radiative warming and the resulting drop in LWP (Fig. 7.9 (i-l)).
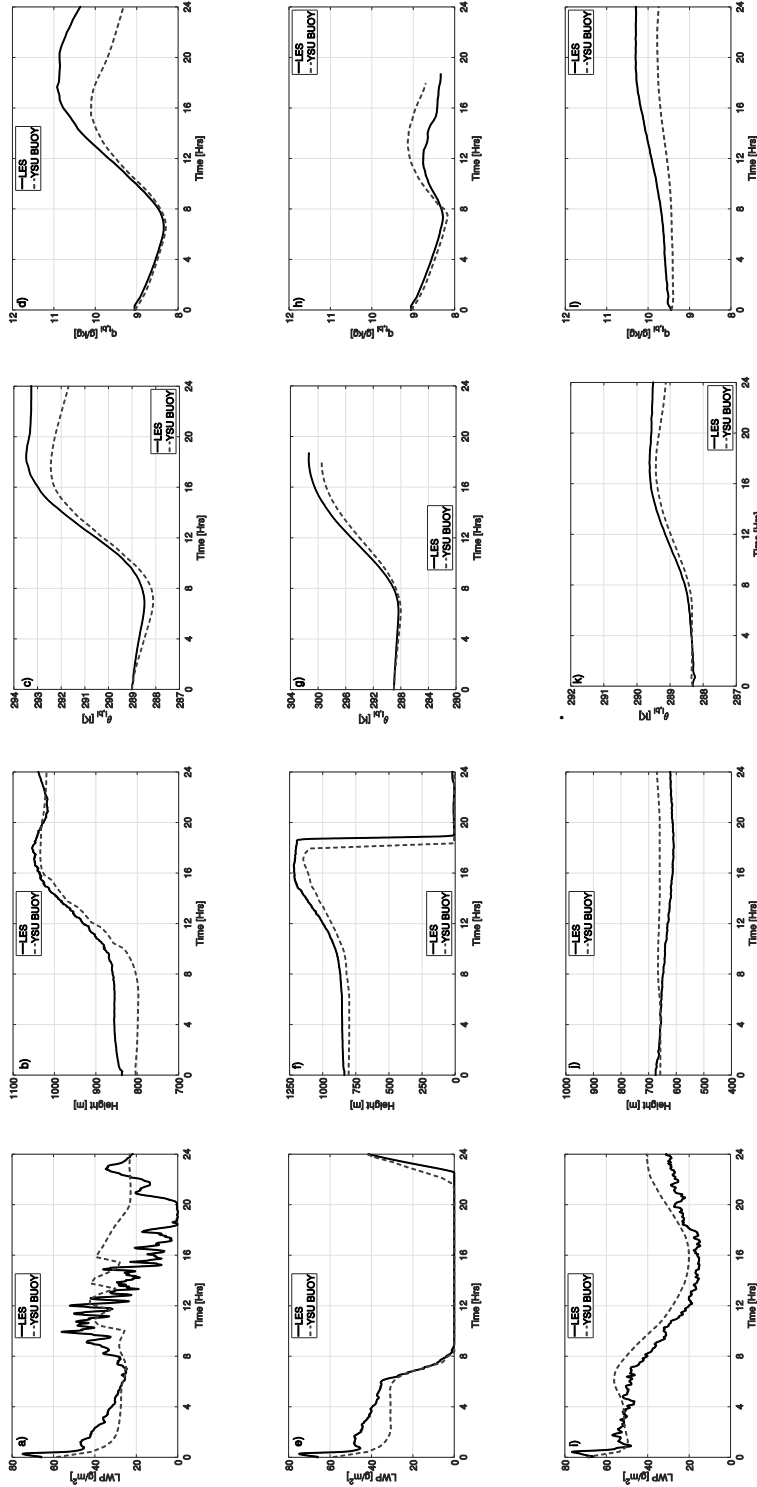
Figure 7.9. Comparison between LES (solid) and YSU-BUOY (dashed grey lines) for (**a, e, i**) LWP, (**b, f, j**), inversion height , (**c, e. k**) liquid potential temperature of the boundary layer ($\theta_{l,bl}$), and (**d, f, l**) total water mixing ratio ($q_{t,bl}$), for the DYCOMS land case with Bowen ratio equal 0.1 (**a-d**), DYCOMS land case with Bowen ratio equal 1.0 (**e-h**), CGILS ocean case (**i-l**).

7.7 Acknowledgement

.

Chapter 8.   Conclusions and Outlook

We employed LES to simulate the STBL over coastal lands (Chapter 3). We find that the main source of turbulence shifts from cloud-top longwave radiative cooling at night to the surface buoyancy flux during the day. In order to capture that transition, we formulate entrainment velocity as function of the surface buoyancy flux and the integrated cloud buoyancy flux (Chapter 4) and incorporate it into a MLM to study how the different physical factors affect the cloud lifetime. The simulated STBL and cloud dissipation time in the MLM was found to be in good agreement with LES results. In particular, the entrainment scheme produced entrainment velocities and inversion heights consistent with the LES results for a variety of cases, including over ocean (Chapter 5).

We found that cloud lifetime is sensitive to land surface conditions characterized by the Bowen ratio since the bulk of the net surface radiation over land is converted to convective fluxes into the boundary layer. For wet land surfaces, latent heat flux dominates over sensible heat flux, thus moistening the STBL and thereby thickening the cloud layer. In contrast, for moderately dry surfaces, the sensible heat flux dominates, and together with entrainment flux they rapidly dissipate the cloud after sunrise. The stronger surface buoyancy fluxes for both wet and dry land cases (compared to the ocean) indirectly thin the cloud by increasing turbulence in the STBL and increasing the cloud top entrainment flux. Furthermore, the surface net radiation induces stronger surface buoyancy fluxes and stronger entrainment at larger Bowen ratios.

The sea breeze is an important feature of coastal environments, and onshore winds advect cool air from over the ocean onto the coast, thereby thickening the cloud

layer. We represented advection effects by prescribing wind speed obtained from surface wind measurements and using temperature and humidity outputs from LES and MLM simulations over the ocean. The advection of ocean air onto the coast plays an important role in modulating the cloud lifetime. For both dry and wet land surface conditions, large-scale horizontal advection cools and dries the STBL. For the wet surface case, the large-scale horizontal advective cooling contributes to maintenance of the cloud layer throughout the day. For the dry surface case with advection, cloud dissipation time is delayed by several hours.

Next, we evaluate the capability of NWP parametrizations in modeling the STBL and offer an improved parameterization for the YSU scheme. We employ three WRF-SCM and bench mark the results against LES to investigate the capability of the different PBL schemes in modeling the STBL (Chapter 7). We find that all three PBL schemes underestimate entrainment flux resulting in cooler, moister boundary layer with much larger LWP. The YSU and ACM2 PBL schemes' turbulent flux parameterization do not take into account the longwave cooling induced turbulence in the boundary layer thereby leading to an underestimation of entrainment flux. Even the MYNN PBL scheme that employs a more sophisticated TKE closure scheme underestimate cloud-top entrainment, which indicates the inherent difficulty in modeling such regimes. The choice of microphysics schemes primarily regulates the upper bound of LWP through different amounts of drizzle precipitation, but the unphysically large LWP is common in all microphysics schemes. This further substantiates that entrainment flux is insufficient to counteract the longwave radiative cooling and surface latent heat flux moistening of the STBL.

In order to improve the parameterization of the STBL we propose a correction to the YSU scheme that takes into account longwave cooling induced turbulence in the boundary layer. We test the corrected scheme against LES for two different initial conditions and find that entrainment flux is better simulated resulting in LWP that closely match those simulated by the LES.

This thesis has highlighted the strong impact of clouds on local population and ecology. Additionally, the thesis has shown that the physics of stratocumulus over coastal land is markedly different to that over the ocean despite cloud originating over the ocean in both cases. The current cloud models that have been developed either for stratocumulus cloud occurring over the ocean, whereby cloud-top longwave radiation is the primary source of turbulence or clear convective boundary layers whereby the surface flux is the primary source of turbulence are not sufficient to describe the physics of a STBL over coastal lands. This thesis resolves some of the issues by describing the physics of STBL over coastal land and proposing corrections to existing parameterization to better model STBL occurring over coastal lands.

Outlook and Recommendation for Future Work

The majority of the literature on stratocumulus clouds surveyed focused on clouds occurring over the ocean, their effects on climate and response to various future climate scenarios. This thesis studies stratocumulus clouds from a weather forecasting perspective, and focuses on the STBL over coastal land and proposes improvements to parameterizations forecast models.

The MLM coupled with the entrainment, radiation parameterization and LSM proposed in this thesis have provided a computationally inexpensive and relatively

accurate method to conduct sensitivity studies on stratocumulus cloud lifetime. The MLM can be run to determine phase spaces in which stratocumulus persist and in which clouds dissipate. These phase spaces, in turn, provide important information on how the STBL would respond to different large-scale climate conditions and anthropogenic forcings. For instance, the MLM can provide important information on the response of the clouds to increased urbanization that leads to increased surface sensible heat flux or to weaker subsidence resulting from the weakening of the Hadley cell. Such studies will help shed some insight on how weather will change in the future. These studies will help answer questions such as: will the persistent marine layer be as prevalent over San Francisco and the bay area in the future? Will heat waves become more prevalent as the Hadley cell weakens?

Despite the significant improvements in our understanding and ability to model stratocumulus clouds, many additional important research questions still exist. Cloud-top entrainment remains very difficult to simulate with operational weather forecast models. While we had relative success in modeling entrainment for strong inversions, weaker thicker inversions are frequently observed in the atmosphere. There is no clear interface between the turbulent air in the STBL and the stratified layer above for the weak thick inversions making it more difficult to model and parametrize the entrainment mixing across the interface. In both types of inversions, modeling the entrainment mixing process occurring near the cloud top between the two-phase fluids at very high Reynolds numbers is difficult to model due to the large range of spatial resolutions that need to be resolved. Recent strides in high-resolution direct numerical simulations, however, are beginning to

shed some light into the cloud-top entrainment mixing and are helping to improve parameterizations.

In addition to cloud-top entrainment, this thesis has demonstrated the important role that large-scale horizontal advection plays in modulating coastal stratocumulus cloud lifetime. However, in order to better study and characterize the effects of large-scale horizontal advection on STBL, better measurements are required. This thesis utilized sparse surface measurements as a proxy for the boundary layer, yet vertical profiles of the STBL measured near the coast along transects aligned with the dominant velocity vector will provide a deeper insight into the physics of the STBL and constrain errors in such models in NWP.

References

Ackerman, A. S., and Coauthors, 2009: Large-Eddy Simulations of a Drizzling, Stratocumulus-Topped Marine Boundary Layer. *Mon. Weather Rev.*, **137**, 1083–1110, doi:10.1175/2008MWR2582.1.

Albrecht, B. A., C. Fairall, D. W. Thomson, and A. B. White, 1990: Surface-Based Remote Sensing of the Observed and the Adiabatic Liquid Water Content of Stratocumulus Clouds. *Geophys. Res. Lett.*, **17**, 89–92, doi:10.1029/GL017i001p00089.

——, C. Bretherton, D. Johnson, W. H. Scubert, and A. S. Frisch, 1995: The Atlantic Stratocumulus Transition Experiment - ASTEX. *Bull. Am. Meteorol. Soc.*, **76**, 889–904, doi:10.1175/1520-0477(1995)076<0889:TASTE>2.0.CO;2.

Bannon, P. R., 1996: On the Anelastic Approximation for a Compressible Atmosphere. *J. Atmos. Sci.*, **53**, 3618–3628, doi:10.1175/1520-0469(1996)053<3618:OTAAFA>2.0.CO;2.

Blossey, P. N., and Coauthors, 2013: Marine low cloud sensitivity to an idealized climate change: The CGILS LES intercomparison. *J. Adv. Model. Earth Syst.*, **5**, 234–258, doi:10.1002/jame.20025.

Bretherton, C., and M. C. Wyant, 1997: Moisture transport, lower-tropospheric stability, and decoupling of cloud-topped boundary layers. *J. Atmos. Sci.*, **54**, 148–167, doi:10.1175/1520-0469(1997)054<0148:MTLTSA>2.0.CO;2.

——, S. Krueger, M. Wyant, P. Bechtold, E. Van Meijgaard, B. Stevens, and J. Teixeira, 1999: A GCSS Boundary-Layer Cloud Model Intercomparison Study Of The First Astex Lagrangian Experiment. *Boundary-Layer Meteorol.*, **93**, 341–380, doi:10.1023/A:1002005429969.

——, P. N. Blossey, and C. R. Jones, 2013: Mechanisms of marine low cloud sensitivity to idealized climate perturbations: A single-LES exploration extending the CGILS cases. *J. Adv. Model. Earth Syst.*, 316–337, doi:10.1002/jame.20019.

Brost, R. A., and J. C. Wyngaard, 1978: A Model Study of the Stably Stratified Planetary Boundary Layer. *J. Atmos. Sci.*, **35**, 1427–1440, doi:10.1175/1520-0469(1978)035<1427:AMSOTS>2.0.CO;2.

Caldwell, P., C. S. Bretherton, and R. Wood, 2005: Mixed-layer budget analysis of the diurnal cycle of entrainment in Southeast Pacific stratocumulus. *J. Atmos. Sci.*, **62**, 3775–3791, doi:10.1175/JAS3561.1.

Chou M.-D., and M. J. Suarez, 1999: A solar radiation parameterization for atmospheric studies. NASA Tech. Rep. NASA/TM-1999-10460, vol. 15, 38 pp

——, and M. J. Suarez, 2001: A thermal infrared radiation parameterization for atmospheric studies. NASA/TM-2001-104606, vol. 19, 55pp

Deardorff, J. W., 1975: The development of boundary layer turbulence models for use in studying the severe storm environmen. *Proceeding SESAME Meet.*, 25–264.

——, 1980: Cloud Top Entrainment Instability. *J. Atmos. Sci.*, **37**, 131–147, doi:10.1175/1520-0469(1980)037<0131:CTEI>2.0.CO;2.

Duda, D. P., G. L. Stephens, and S. K. Cox, 1991: Microphysical and Radiative Properties of Marine Stratocumulus from Tethered Balloon Measurements. *J. Appl. Meteorol.*, **30**, 170–186, doi:10.1175/1520-0450(1991)030<0170:MARPOM>2.0.CO;2.

van der Dussen, J. J., S. R. de Roode, and A. P. Siebesma, 2014: Factors Controlling Rapid Stratocumulus Cloud Thinning. *J. Atmos. Sci.*, **71**, 655–664, doi:10.1175/JAS-D-13-0114.1.

Durran, D. R., 1989: Improving the Anelastic Approximation. *J. Atmos. Sci.*, **46**, 1453–1461, doi:10.1175/1520-0469(1989)046<1453:ITAA>2.0.CO;2.

Duynkerke, P. G., and Coauthors, 2004: Observations and numerical simulations of the diurnal cycle of the EUROCS stratocumulus case. *Q. J. R. Meteorol. Soc.*, **130**, 3269–3296, doi:10.1256/qj.03.139.

EPA, 2004: User's Guide for the AERMOD Meteorological Preprocessor (AERMET). EPA-454/B-03-002. U.S. Environmental Protection Agency, Research Triangle Park, NC.

Fang, M., B. Albrecht, V. Ghate, and P. Kollias, 2014a: Turbulence in Continental Stratocumulus, Part II: Eddy Dissipation Rates and Large-Eddy Coherent Structures. *Boundary-Layer Meteorol.*, **150**, 361–380, doi:10.1007/s10546-013-9872-4.

——, ——, ——, and ——, 2014b: Turbulence in Continental Stratocumulus, Part I: External Forcings and Turbulence Structures. *Boundary-Layer Meteorol.*, **150**, 341–360, doi:10.1007/s10546-013-9873-3.

Fedorovich, E., R. Conzemius, and D. Mironov, 2004: Convective entrainment into a shear-free, linearly stratified atmosphere: Bulk models reevaluated through large eddy simulations. *J. Atmos. Sci.*, **61**, 281–295, doi:10.1175/1520-0469(2004)061<0281:CEIASL>2.0.CO;2.

Fu, Q., and K. N. Liou, 1992: On the Correlated k-Distribution Method for Radiative Transfer in Nonhomogeneous Atmospheres. *J. Atmos. Sci.*, **49**, 2139–2156, doi:10.1175/1520-0469(1992)049<2139:OTCDMF>2.0.CO;2.

Gamon, J. A., and Coauthors, 2010: SpecNet revisited: bridging flux and remote sensing communities. *Can. J. Remote Sens.*, **36**, S376–S390.

Garcia, J. R., and J. P. Mellado, 2014: The Two-Layer Structure of the Entrainment Zone in the Convective Boundary Layer. *J. Atmos. Sci.*, **71**, 1935–1955, doi:10.1175/JAS-D-13-0148.1.

Gershunov, A., D. R. Cayan, and S. F. Iacobellis, 2009: The Great 2006 Heat Wave over California and Nevada: Signal of an Increasing Trend. *J. Clim.*, **22**, 6181–6203, doi:10.1175/2009JCLI2465.1.

Gesso, S. D., A. P. Siebesma, S. R. de Roode, and J. M. van Wessem, 2014: A mixed-layer model perspective on stratocumulus steady states in a perturbed climate. *Q. J. R. Meteorol. Soc.*, **140**, 2119–2131, doi:10.1002/qj.2282.

Ghate, V. P., B. A. Albrecht, and P. Kollias, 2010: Vertical velocity structure of nonprecipitating continental boundary layer stratocumulus clouds. *J. Geophys. Res. Atmos.*, **115**, D13204, doi:10.1029/2009JD013091.

Ghonima, M. S., J. R. Norris, T. Heus, and J. Kleissl, 2015: Reconciling and Validating the Cloud Thickness and Liquid Water Path Tendencies Proposed by R. Wood and J. J. van der Dussen et al. *J. Atmos. Sci.*, **72**, 2033–2040, doi:10.1175/JAS-D-14-0287.1.

——, T. Heus, J. R. Norris, and J. Kleissl, 2016: Factors controlling stratocumulus cloud lifetime over coastal land. *J. Atmos. Sci.*, doi:10.1175/JAS-D-15-0228.1.

Goody, R. M., 1995: *Principles of Atmospheric Physics and Chemistry*. 118 pp.

Grenier, H., and C. S. Bretherton, 2001: A Moist PBL Parameterization for Large-Scale Models and Its Application to Subtropical Cloud-Topped Marine Boundary Layers. *Mon. Weather Rev.*, **129**, 357–377, doi:10.1175/1520-0493(2001)129<0357:AMPPFL>2.0.CO;2.

Hahn, C. H., and S. G. Warren, 2007: A gridded climatology of clouds over land (1971–96) and ocean (1954–97) from surface observations worldwide.

Han, J., and H.-L. Pan, 2011: Revision of Convection and Vertical Diffusion Schemes in the NCEP Global Forecast System. *Weather Forecast.*, **26**, 520–533, doi:10.1175/WAF-D-10-05038.1.

Heus, T., and Coauthors, 2010: Formulation of the Dutch Atmospheric Large-Eddy Simulation (DALES) and overview of its applications. *Geosci. Model Dev.*, **3**, 415–444, doi:10.5194/gmd-3-415-2010.

Hilliker, J. L., and J. M. Fritsch, 1999: An Observations-Based Statistical System for Warm-Season Hourly Probabilistic Forecasts of Low Ceiling at the San Francisco International Airport. *J. Appl. Meteorol.*, **38**, 1692–1705, doi:10.1175/1520-0450(1999)038<1692:AOBSSF>2.0.CO;2.

Holt, T., and S. Raman, 1988: A review and comparative evaluation of multilevel boundary layer parameterizations for first-order and turbulent kinetic energy closure schemes. *Rev. Geophys.*, **26**, 761, doi:10.1029/RG026i004p00761.

Holtslag, A. A. M., and B. A. Boville, 1993: Local Versus Nonlocal Boundary-Layer Diffusion in a Global Climate Model. *J. Clim.*, **6**, 1825–1842, doi:10.1175/1520-0442(1993)006<1825:LVNBLD>2.0.CO;2.

Hong, S., V. Lakshmi, E. E. Small, F. Chen, M. Tewari, and K. W. Manning, 2009: Effects of vegetation and soil moisture on the simulated land surface processes from the coupled WRF/Noah model. *J. Geophys. Res. Atmos.*, **114**, D18118, doi:10.1029/2008JD011249.

Hong, S.-Y., J. Dudhia, and S.-H. Chen, 2004: A Revised Approach to Ice Microphysical Processes for the Bulk Parameterization of Clouds and Precipitation. *Mon. Weather Rev.*, **132**, 103–120, doi:10.1175/1520-0493(2004)132<0103:ARATIM>2.0.CO;2.

——, Y. Noh, and J. Dudhia, 2006: A New Vertical Diffusion Package with an Explicit Treatment of Entrainment Processes. *Mon. Weather Rev.*, **134**, 2318–2341, doi:10.1175/MWR3199.1.

Hu, X.-M., J. W. Nielsen-Gammon, and F. Zhang, 2010: Evaluation of Three Planetary Boundary Layer Schemes in the WRF Model. *J. Appl. Meteorol. Climatol.*, **49**, 1831–1844, doi:10.1175/2010JAMC2432.1.

Iacobellis, S. F., and D. R. Cayan, 2013: The variability of California summertime marine stratus: Impacts on surface air temperatures. *J. Geophys. Res. Atmos.*, **118**, 9105–9122, doi:10.1002/jgrd.50652.

Jamaly, M., J. L. Bosch, and J. Kleissl, 2013: Aggregate Ramp Rates of Distributed Photovoltaic Systems in San Diego County. *Sustain. Energy, IEEE Trans.*, **4**, 519–526, doi:10.1109/TSTE.2012.2201966.

Janjic, Z., and M. Pyle, 2010: *Scientific documentation for the NMM solver. NCAR Technical Note NCAR/TN 477+STR.*

Janjic, Z., and Coauthors, 2011: *3, User's guide for the NMM Core of the Weather Research and Forecast (WRF) Modeling System Version*. 195 pp.

——, and Coauthors, 2011: *3, User's guide for the NMM Core of the Weather Research and Forecast (WRF) Modeling System Version*. 195 pp.

Jones, C. R., C. S. Bretherton, and P. N. Blossey, 2014: Fast stratocumulus timescale in mixed layer model and large eddy simulation. *J. Adv. Model. Earth Syst.*, 206–222, doi:10.1002/2013MS000289.

Joseph, J. H., W. J. Wiscombe, and J. A. Weinman, 1976: The Delta-Eddington Approximation for Radiative Flux Transfer. *J. Atmos. Sci.*, **33**, 2452–2459, doi:10.1175/1520-0469(1976)033<2452:TDEAFR>2.0.CO;2.

Kazil, J., G. Feingold, and T. Yamaguchi, 2015: Wind speed response of marine non-precipitating stratocumulus clouds over a diurnal cycle in cloud-system resolving simulations. *Atmos. Chem. Phys. Discuss.*, **15**, 28395–28452, doi:10.5194/acpd-15-28395-2015.

Kessler, E., 1995: On the continuity and distribution of water substance in atmospheric circulations. *Atmos. Res.*, **38**, 109–145, doi:10.1016/0169-8095(94)00090-Z.

Klein, S. A., and D. L. Hartmann, 1993: The Seasonal Cycle of Low Stratiform Clouds. *J. Clim.*, **6**, 1587–1606, doi:10.1175/1520-0442(1993)006<1587:TSCOLS>2.0.CO;2.

Kollias, P., and B. Albrecht, 2000: The Turbulence Structure in a Continental Stratocumulus Cloud from Millimeter-Wavelength Radar Observations. *J. Atmos. Sci.*, **57**, 2417–2434, doi:10.1175/1520-0469(2000)057<2417:TTSIAC>2.0.CO;2.

Lacis, A. A., and V. Oinas, 1991: A description of the correlated k distribution method for modeling nongray gaseous absorption, thermal emission, and multiple scattering in vertically inhomogeneous atmospheres. *J. Geophys. Res. Atmos.*, **96**, 9027–9063, doi:10.1029/90JD01945.

Larson, V. E., K. E. Kotenberg, and N. B. Wood, 2007: An Analytic Longwave Radiation Formula for Liquid Layer Clouds. *Mon. Weather Rev.*, **135**, 689–699, doi:10.1175/MWR3315.1.

Lee, S. S., J. E. Penner, and S. M. Saleeby, 2009: Aerosol effects on liquid-water path of thin stratocumulus clouds. *J. Geophys. Res. Atmos.*, **114**, D07204, doi:10.1029/2008JD010513.

Lilly, D. K., 1968: Models of Cloud-Topped Mixed Layers Under a Strong Inversion. *Q. J. R. Meteorol. Soc.*, **94**, 292–309, doi:10.1002/qj.49709440106.

Lin, Y.-L., R. D. Farley, and H. D. Orville, 1983: Bulk Parameterization of the Snow Field in a Cloud Model. *J. Clim. Appl. Meteorol.*, **22**, 1065–1092, doi:10.1175/1520-0450(1983)022<1065:BPOTSF>2.0.CO;2.

Lock, A. P., and M. K. Macvean, 1999: The parametrization of entrainment driven by surface heating and cloud-top cooling. *Q. J. R. Meteorol. Soc.*, **125**, 271–299, doi:10.1002/qj.49712555315.

——, Brown, A. R., Bush, M. R., Martin, G. M., & Smith, R. N. B. (2000). A New Boundary Layer Mixing Scheme. Part I: Scheme Description and Single-Column Model Tests. *Monthly Weather Review*, *128*(9), 3187–3199.

Mathiesen, P., and J. Kleissl, 2011: Evaluation of numerical weather prediction for intra-day solar forecasting in the continental United States. *Sol. Energy*, **85**, 967–977, doi:10.1016/j.solener.2011.02.013.

——, C. Collier, and J. Kleissl, 2013: A high-resolution, cloud-assimilating numerical weather prediction model for solar irradiance forecasting. *Sol. Energy*, **92**, 47–61, doi:10.1016/j.solener.2013.02.018.

Mechem, D. B., Y. L. Kogan, and D. M. Schultz, 2010: Large-Eddy Simulation of Post-Cold-Frontal Continental Stratocumulus. *J. Atmos. Sci.*, **67**, 3835–3853, doi:10.1175/2010JAS3467.1.

Mellor, G. L., and T. Yamada, 1974: A Hierarchy of Turbulence Closure Models for Planetary Boundary Layers. *J. Atmos. Sci.*, **31**, 1791–1806, doi:10.1175/1520-0469(1974)031<1791:AHOTCM>2.0.CO;2.

Meneveau, C., and J. Katz, 2000: Scale-invariance and turbulence models for large-eddy simulation. *Annu. Rev. Fluid Mech.*, **32**, 1–32, doi:10.1146/annurev.fluid.32.1.1.

Morrison, H., J. A. Curry, and V. I. Khvorostyanov, 2005: A New Double-Moment Microphysics Parameterization for Application in Cloud and Climate Models. Part I: Description. *J. Atmos. Sci.*, **62**, 1665–1677, doi:10.1175/JAS3446.1.

Myers, T. A., and J. R. Norris, 2013: Observational Evidence That Enhanced Subsidence Reduces Subtropical Marine Boundary Layer Cloudiness. *J. Clim.*, **26**, 7507–7524, doi:10.1175/JCLI-D-12-00736.1.

Nakanishi, M., and H. Niino, 2004: An Improved Mellor–Yamada Level-3 Model with Condensation Physics: Its Design and Verification. *Boundary-Layer Meteorol.*, **112**, 1–31, doi:10.1023/B:BOUN.0000020164.04146.98.

Nicholls, S., 1984: The dynamics of stratocumulus: Aircraft observations and comparisons with a mixed layer model. *Q. J. R. Meteorol. Soc.*, **110**, 783–820, doi:10.1002/qj.49711046603.

——, and J. D. Turton, 1986: An observational study of the structure of stratiform cloud sheets : Part II Entrainment. *Q. J. R. Meteorol. Soc.*, **112**, 461–480.

Nielsen-Gammon, J. W., X.-M. Hu, F. Zhang, and J. E. Pleim, 2010: Evaluation of Planetary Boundary Layer Scheme Sensitivities for the Purpose of Parameter Estimation. *Mon. Weather Rev.*, **138**, 3400–3417, doi:10.1175/2010MWR3292.1.

Niu, G.-Y., 2011: *The community NOAH land-surface model (lsm) with multi-physics options*. 1-20 pp.

Ogura, Y., and N. A. Phillips, 1962: Scale Analysis of Deep and Shallow Convection in the Atmosphere. *J. Atmos. Sci.*, **19**, 173–179, doi:10.1175/1520-0469(1962)019<0173:SAODAS>2.0.CO;2.

Pal, S., and M. Haeffelin, 2015: Forcing mechanisms governing diurnal, seasonal, and interannual variability in the boundary layer depths: Five years of continuous lidar observations over a suburban site near Paris. *J. Geophys. Res. Atmos.*, **120**, 11,911–936,956, doi:10.1002/2015JD023268.

Perez, R., and Coauthors, 2013: Comparison of numerical weather prediction solar irradiance forecasts in the US, Canada and Europe. *Sol. Energy*, **94**, 305–326, doi:10.1016/j.solener.2013.05.005.

Pincus, R., and B. Stevens, 2009: Monte Carlo Spectral Integration: a Consistent Approximation for Radiative Transfer in Large Eddy Simulations. *J. Adv. Model. Earth Syst.*, **1**, 1, doi:10.3894/JAMES.2009.1.1.

Pleim, J. E., 2007: A Combined Local and Nonlocal Closure Model for the Atmospheric Boundary Layer. Part I: Model Description and Testing. *J. Appl. Meteorol. Climatol.*, **46**, 1383–1395, doi:10.1175/JAM2539.1.

——, and J. S. Chang, 1992: A non-local closure model for vertical mixing in the convective boundary layer. *Atmos. Environ. Part A. Gen. Top.*, **26**, 965–981, doi:10.1016/0960-1686(92)90028-J.

Price, J. D., 1999: Observations of stratocumulus cloud break-up over land. *Q. J. R. Meteorol. Soc.*, **125**, 441–468, doi:10.1002/qj.49712555404.

Randall, D. A., J. A. Coakley, D. H. Lenschow, C. W. Fairall, and R. A. Kropfli, 1984 Outlook for Research on Subtropical Marine Stratification Clouds. *Bull. Am.*

Meteorol. Soc., **65**, 1290–1301, doi:10.1175/1520-0477(1984)065<1290:OFROSM>2.0.CO;2.

Remund, J., R. Perez, and E. Lorenz, 2008: Comparison of solar radiation forecasts for the USA. *European PV Conference*.

Schwartz, R. E., A. Gershunov, S. F. Iacobellis, and D. R. Cayan, 2014: North American west coast summer low cloudiness: Broadscale variability associated with sea surface temperature. *Geophys. Res. Lett.*, **41**, 2014GL059825, doi:10.1002/2014GL059825.

Seifert, A., and K. D. Beheng, 2001: A double-moment parameterization for simulating autoconversion, accretion and selfcollection. *Atmos. Res.*, **59**, 265–281, doi:10.1016/S0169-8095(01)00126-0.

Shettle, E. P., and J. A. Weinman, 1970: The Transfer of Solar Irradiance Through Inhomogeneous Turbid Atmospheres Evaluated by Eddington's Approximation. *J. Atmos. Sci.*, **27**, 1048–1055, doi:10.1175/1520-0469(1970)027<1048:TTOSIT>2.0.CO;2.

Skamarock, W. C., and Coauthors, 2008: *A description of the advanced research WRF – version 3. NCAR Technical Note NCAR/TN 475+STR.*

Skupniewicz, C. E., J. W. Glendening, and R. F. Kamada, 1991: Boundary-Layer Transition across a Stratocumulus Cloud Edge in a Coastal Zone. *Mon. Weather Rev.*, **119**, 2337–2357, doi:10.1175/1520-0493(1991)119<2337:BLTAAS>2.0.CO;2.

Slingo, A., 1990: Sensitivity of the Earth's radiation budget to changes in low clouds. *Nature*, **343**, 49–51.

SolarAnywhere, 2014: SolarAnywhere Data. Clean Power Research 2014. http://www.solaranywhere.com.

Stevens, B., 2002: Entrainment in stratocumulus-topped mixed layers. *Q. J. R. Meteorol. Soc.*, **128**, 2663–2690, doi:10.1256/qj.01.202.

——,and Coauthors, 2003a: On entrainment rates in nocturnal marine stratocumulus. *Q. J. R. Meteorol. Soc.*, **129**, 3469–3493, doi:10.1256/qj.02.202.

——, and Coauthors, 2003b: Dynamics and Chemistry of Marine Stratocumulus—DYCOMS-II. *Bull. Am. Meteorol. Soc.*, **84**, 579–593, doi:10.1175/BAMS-84-5-579.

——, and Coauthors, 2005: Evaluation of large-Eddy simulations via observations of nocturnal marine stratocumulus. *Mon. Weather Rev.*, **133**, 1443–1462, doi:10.1175/MWR2930.1.

——, and A. Seifert, 2008: Understanding macrophysical outcomes of microphysical choices in simulations of shallow cumulus convection. *J. Meteorol. Soc. JAPAN*, **86A**, 143–162.

——,2010: Cloud-top entrainment instability? *J. Fluid Mech.*, **660**, 1, doi:10.1017/S0022112010003575.

Stull, R. B., 1988: *An Introduction to Boundary Layer Meteorology*. Kluwer Academic Publishers.

Sullivan, P. P., C. H. Moeng, B. Stevens, D. H. Lenschow, and S. D. Mayor, 1998: Structure of the entrainment zone capping the convective atmospheric boundary layer. J. Atmos. Sci., 55, 3042–3064, doi:10.1175/1520-0469(1998)055<3042:SOTEZC>2.0.CO;2.

Taylor, S. V, D. R. Cayan, N. E. Graham, and K. P. Georgakakos, 2008: Northerly surface winds over the eastern North Pacific Ocean in spring and summer. *J. Geophys. Res.*, **113**, doi:10.1029/2006JD008053.

Thompson, G., P. R. Field, R. M. Rasmussen, and W. D. Hall, 2008: Explicit Forecasts of Winter Precipitation Using an Improved Bulk Microphysics Scheme. Part II: Implementation of a New Snow Parameterization. *Mon. Weather Rev.*, **136**, 5095–5115, doi:10.1175/2008MWR2387.1.

Uchida, J., C. S. Bretherton, and P. N. Blossey, 2010: The sensitivity of stratocumulus-capped mixed layers to cloud droplet concentration: do LES and mixed-layer models agree? *Atmos. Chem. Phys.*, **10**, 4097–4109, doi:10.5194/acp-10-4097-2010.

Warren, S. G., C. H. Hahn, R. M. London, R. M. Chervin, and R. L. Jenne, 1986: Global Distribution of Total Cloud Cover and Cloud Type Amounts Over Land. *NCAR Tech. Note*, **NCAR/TN-27**.

——, ——, ——, ——, ——, 1988: Global Distribution of Total Cloud Cover and Cloud Type Amounts Over the Ocean. . *NCAR Tech. Note*, **NCAR/TN-31**.

Wood, R., 2007: Cancellation of aerosol indirect effects in marine stratocumulus through cloud thinning. *J. Atmos. Sci.*, **64**, 2657–2669, doi:10.1175/JAS3942.1.

——, 2012: Stratocumulus Clouds. *Mon. Weather Rev.*, **140**, 2373–2423, doi:10.1175/MWR-D-11-00121.1.

——, C. S. Bretherton, and D. L. Hartmann, 2002: Diurnal cycle of liquid water path over the subtropical and tropical oceans. *Geophys. Res. Lett.*, **29**, 2092, doi:10.1029/2002GL015371.

——, and Coauthors, 2011: The VAMOS Ocean-Cloud-Atmosphere-Land Study Regional Experiment (VOCALS-REx): goals, platforms, and field operations. *Atmos. Chem. Phys.*, **11**, 627–654, doi:10.5194/acp-11-627-2011.

Yamamoto, G., A. Shimanuki, M. Aida, and N. Yasuda, 1973: Diurnal Variation of Wind and Temperature Fields in the Ekman Layer. *J. Meteorol. Soc. Japan. Ser. II*, **51**, 377–387.

Zhang, M., C. S. Bretherton, P. N. Blossey, S. Bony, F. Brient, and J.-C. Golaz, 2012: The CGILS experimental design to investigate low cloud feedbacks in general circulation models by using single-column and large-eddy simulation models. *J. Adv. Model. Earth Syst.*, **4**, M12001, doi:10.1029/2012MS000182.

——, and Coauthors, 2013: CGILS: Results from the first phase of an international project to understand the physical mechanisms of low cloud feedbacks in single column models. *J. Adv. Model. Earth Syst.*, **5**, 826–842, doi:10.1002/2013MS000246.

Zhu, P., B. Albrecht, and J. Gottschalck, 2001: Formation and Development of Nocturnal Boundary Layer Clouds over the Southern Great Plains. *J. Atmos. Sci.*, **58**, 1409–1426, doi:10.1175/1520-0469(2001)058<1409:FADONB>2.0.CO;2.

——, and Coauthors, 2005: Intercomparison and Interpretation of Single-Column Model Simulations of a Nocturnal Stratocumulus-Topped Marine Boundary Layer. *Mon. Weather Rev.*, **133**, 2741–2758, doi:10.1175/MWR2997.1.